

ORDERED THREE-DIMENSIONAL CARBON-BASED
MULTIFUNCTIONAL NANOHYBRIDS FOR ENERGY STORAGE

A Dissertation

Presented to the Faculty of the Graduate School

of Cornell University

in Partial Fulfillment of the Requirements for the Degree of

Doctor of Philosophy

by

Jörg Gerd Werner

February 2016

© 2016 Jörg Gerd Werner

ALL RIGHTS RESERVED

ORDERED THREE-DIMENSIONAL CARBON-BASED MULTIFUNCTIONAL NANOHYBRIDS FOR ENERGY STORAGE

Jörg Gerd Werner, Ph. D.

Cornell University 2016

Nanostructures of countless materials have been studied extensively over the past decades for their interesting and highly tunable properties that go far beyond their characteristics in the bulk. While the variety of reported nanostructures, morphologies, and porosities is vast, little is still understood regarding the structure-property relationships for nanomaterials in energy storage. Furthermore, the potentials of multi-component nanohybrids, including complete nanodevices, are not fully explored. Block copolymer structure direction of inorganic nanomaterials provides a synthetic pathway for precise control over many relevant parameters.

In this thesis, the highly tunable synthesis of ordered mesoporous carbons from the self-assembly and structure direction of triblock terpolymers and phenolic resols is described. The tailorability of porosity, pore size, surface area, chemical composition, and morphology by design is demonstrated, including two different gyroidal carbons. These mesoporous carbon materials with a wide range of characteristics are employed in a structure-property relationship study as sulfur hosts in lithium-sulfur batteries. This methodological investigation demonstrates the beneficial impact of microporosity and low carbonization temperature, which influences the chemical composition of the carbon material, on cyclability and capacity retention of carbon-sulfur composite cathodes.

To extend the idea of three-dimensionally ordered multi-component nanomaterials that combine and potentially enhance the functionality of its individual components, atomic layer deposition is investigated towards its applicability on nanoporous materials. It is shown that a conformal, nanometer thin titanium dioxide coating on gyroidal mesopores can be achieved over microns in deposition depth on free-standing

carbonaceous substrates. The obtained ordered gyroidal mesoporous core-shell hybrid exhibit triple-functionality with a graphitized carbon core, crystallized anatase-titania shell, and a continuous mesoporous phase.

With the inclusion of a third solid phase in the gyroidal architecture the complexity of ordered multicomponent nanostructures is further increased. The “total synthesis” of a 3D-nanointegrated all-solid-state battery is described using almost entirely polymer based processing and materials. Free-standing gyroidal mesoporous carbon is used as the anode of a lithium ion battery and coated with an ultra-thin polymer electrolyte through self-limiting electropolymerization. The 3D-battery architecture is completed by backfilling the resulting mesoporosity of the anode-electrolyte assembly with sulfur and in-situ polymerized conducting polymer.

BIOGRAPHICAL SKETCH

Jörg was born in Berlin, Germany, as the second of four children. Growing up in Berlin, Jörg enjoyed spending as much time outside as possible and explored his surroundings, in nature and in the city. Jörg and his family moved to Frankfurt a. M. during elementary school, after which he attended the Dreieich Gymnasium Langen (middle and high school) from 1996 through 2005. During this time he was an active member of the track and field club, as an athlete as well as an official. He also took part in his first independent research project in his last two high school years as part of the “Jugend forscht” (youth researching) program in biochemistry, investigating the influence of heavy metal salts and surfactants on cell performance. This research led to a first place prize in the regional science fair and third place award in the state. In tenth grade, Jörg started tutoring math and physical sciences, which he continued for many years. Both these experiences fostered his interest in becoming a teacher and scientist. After high school, Jörg did his civil service with a local welfare organization for one year.

In the fall of 2006, Jörg started studying chemistry at the Johannes Gutenberg University in Mainz. Quickly, he discovered his interest in functional materials, in particular for sustainable energy solutions. A term paper on photovoltaics and a research class in the group of Prof. Tremel on inorganic materials for advanced solar cells strengthened his interest in energy materials. In 2009, Jörg was allowed to visit Cornell University for six months for a semester abroad. He worked in the group of Prof. Uli Wiesner on polymeric water filtration membranes and block copolymer-inorganic hybrid materials. This visit fostered his strong interest in functional polymeric, inorganic, and hybrid materials. He also discovered fascination with ordered structures and nanomaterials. Cornell University intrigued him very much with its collaborative and open atmosphere, as well as the world-class facilities that were at his disposal. The joy of the research in the group of Prof. Wiesner and his attraction to Cornell planted the idea in Jörg’s head to go to graduate school at Cornell. After returning to Mainz from the semester abroad, Jörg worked again in the group of Prof. Tremel on high aspect ratio inorganic nanomaterials for dye-sensitized and bulk

heterojunction solar cells, and subsequently finished his studies and graduated with a Diploma in chemistry in the summer of 2011.

Jörg started research in the Wiesner group in early 2011, before officially starting his PhD at Cornell in the fall of the same year. As part of the Energy Materials Center at Cornell (emc²), Jörg researched the synthesis and use of ordered nanostructured carbon materials from block copolymer self-assembly for energy storage applications under the supervision of Prof. Uli Wiesner. He was actively involved in the center, from organizing meetings and retreats for the lithium-sulfur battery initiative, to representing the center at scientific advisory board and Department of Energy review meetings. Through emc², Jörg got in contact and made friends with many students from different groups and various departments across the university. He enjoyed the countless productive discussions and idea exchanges with his peers. This and the approachable faculty of the center fostered numerous productive collaborations. In particular, the contact with his committee members Prof. DiSalvo and Prof. Abruña allowed him to intellectually and professionally gain as much as possible from his time at Cornell. The work described here in his thesis summarizes the major focus of his work in the Wiesner lab.

DEDICATED TO MY FAMILY AND FRIENDS.

ACKNOWLEDGEMENTS

This work has benefited from the guidance, discussion, help, and collaborations of many people at and outside of Cornell University. In particular I would like to acknowledge my thesis advisor, Prof. Uli Wiesner, for giving me the opportunity to work independently on projects as interesting, challenging, and fascinating as the ones presented in this thesis. I am very grateful for his guidance that started well before graduate school and, I am sure, will last for even longer. I would like to thank my other committee members Prof. Francis J. DiSalvo and Prof. Héctor D. Abruña for the very helpful and fruitful input I received from them, as well as allowing me the use of their equipment and labs.

A big thank you goes to all the members of the Wiesner group. I was lucky enough to get to know two generations of Wiesner group members, both of which I am very grateful for providing helpful insight, enthusiastic discussions, and fun experiences in and outside the lab. In particular I would like to thank the alumni Dr. Rachel Dorin, Dr. Hiroaki Sai, Dr. Kahyun Hur, Dr. Srikant Iyer, and Dr. Hitesh Arora for teaching me many techniques, instrumentations, characterization, and analysis methods during my semester abroad at Cornell that helped me tremendously as a graduate student. Additionally to the above mentioned, I would like to particularly acknowledge Dr. Tobias Hoheisel for his help with the work from chapter 2, Dr. Gabriel Rodríguez Calero, an alumnus of Prof. Abruña's group, for his collaboration on chapter 5, and Dr. Kwan Tan, Sarah Hesse, Dr. Yibei Gu, and Dr. Spencer Robbins for successful and fruitful collaborations on projects not described in this thesis. For their help, I would like to acknowledge the undergraduate students who worked with me, in particular Samuel Johnson and Vishal Vijay for their help with the work of chapter 3. I would like to also express my gratitude to Dolores Dewbury for all her administrative help.

I also would like to thank Prof. Ulrich Steiner and his former student and postdoc Dr. Maik Scherer for giving me the opportunity to visit them at Cambridge University, UK, and for their help on chapter 4. Special thanks goes to Prof. Sol Gruner and Mark Tate for advice and assistance with SAXS measurements. Furthermore, I acknowledge the members of the DiSalvo and Abruña groups and other

emc² members, in particular Dr. Michael Lowe, Dr. Jie Gao, Dr. Luis Estevez, Dr. Chinmayee Subban, Ryo Wakabayashi, Ritu Sahore, and Dr. Juchen Guo, for helpful discussions and aid with applied battery research.

For training and constant help and advice on many instruments across campus, I would like to thank John Grazul (CCMR, TEMs), Mick Thomas and Don Werder (CCMR, SEMs), Anthony Condo (GPC), Arthur Woll (CHESS), Dr. Christopher Umbach (CCMR, Raman), and Philip Carubia (CCMR, furnaces).

For their unlimited support throughout my whole life, especially morally and mentally, I want to thank my parents, Esther and Gerd, and my siblings, Janine, Juliane and Jan, and my entire family. A very special thanks goes to Katie Camera for her love and support throughout this journey.

TABLE OF CONTENTS

| | |
|--|-------|
| Biographical Sketch..... | iii |
| Dedication..... | v |
| Acknowledgements..... | vi |
| List of Figures..... | x |
| List of Tables..... | xviii |
| Chapter 1 | 1 |
| Introduction..... | 1 |
| Abstract..... | 1 |
| Macromolecules..... | 2 |
| Block Copolymers..... | 3 |
| Anionic Polymerization..... | 8 |
| Block Copolymer Hybrids..... | 11 |
| Thesis outline..... | 13 |
| References..... | 16 |
| Chapter 2 | 19 |
| Synthesis and Characterization of Gyroidal Mesoporous Carbons and Carbon Monoliths with Tunable Ultralarge Pore Size..... | 19 |
| Abstract..... | 19 |
| Introduction..... | 20 |
| Results and Discussion..... | 22 |
| Conclusion..... | 40 |
| Methods..... | 41 |
| Acknowledgements..... | 44 |
| Appendix A..... | 45 |
| Raman Spectroscopy:..... | 47 |
| Hexagonally oriented cylindrical carbon morphology..... | 48 |
| References..... | 50 |
| Chapter 3 | 54 |
| Carbon-Sulfur Composites from Cylindrical and Gyroidal Mesoporous Carbons with Tunable Properties in Lithium-Sulfur Batteries..... | 54 |
| Abstract..... | 54 |
| Introduction..... | 55 |
| Results and Discussion..... | 57 |
| Conclusions..... | 69 |
| Experimental..... | 69 |
| Acknowledgement..... | 72 |
| Appendix B..... | 73 |
| References..... | 78 |

| | |
|--|-----|
| Chapter 4 | 83 |
| Gyroidal Mesoporous Multifunctional Nanocomposites via Atomic Layer Deposition | 83 |
| Abstract..... | 83 |
| Introduction | 84 |
| Results and Discussion | 85 |
| Conclusions | 93 |
| Experimental Section..... | 94 |
| Acknowledgement..... | 95 |
| Appendix C..... | 96 |
| References..... | 97 |
| | |
| Chapter 5 | 99 |
| Gyroidal Nano-Integrated Solid-State 3D-Battery..... | 99 |
| Abstract..... | 99 |
| Introduction | 100 |
| Results and discussion | 104 |
| Conclusion..... | 114 |
| Experimental Section..... | 114 |
| Appendix D..... | 118 |
| References..... | 123 |
| | |
| Chapter 6 | 127 |
| Conclusions..... | 127 |
| References..... | 131 |

LIST OF FIGURES

- Figure 1.1.** (a) Theoretical phase diagram of a diblock copolymer and (b) experimental phase diagram of poly(styrene-*block*-isoprene) (PS-PI). (c) Equilibrium morphologies for an AB-diblock copolymer for different volume fractions of A (f: Volume fraction of B; Dis: Disordered; Scp: Closed-packed spheres; S/BCC: Body-centered cubic; C/HEX: Hexagonally packed cylinders; G: Gyroid; L/LAM: Lamellar).¹⁰ Apart from the lamellar morphology, the block with the higher volume fraction forms a matrix the other block is embedded in, forming a 1-D (spheres), 2-D (hexagonal, lamellar) or 3-D (gyroid) structure. The difference between theoretical and experimental phase diagrams is mostly caused by non-uniform aspect ratios of the different monomers, and thermal and concentration fluctuations, especially in the weak segregation limit. As described above, the Flory-Huggins interaction parameter is temperature dependent, which typically leads to an order-disorder transition at elevated temperatures (TODT), above which the blocks start mixing with each other..... 6
- Figure 1.2.** ABC triblock terpolymer phase diagrams. Left: Theoretical phase map of an idealized triblock terpolymer with equal statistical segment lengths for each block and with $\chi_{AC}N = 35$, $\chi_{AB}N = \chi_{BC}N = 13$. Right: Theoretical phase map for a model ISO triblock terpolymer, with statistical segment lengths $b_I = 6.0 \text{ \AA}$, $b_S = 5.5 \text{ \AA}$, and $b_O = 7.8 \text{ \AA}$ and interaction parameters $\chi_{IS}N = 11.0$, $\chi_{SO}N = 14.2$, and $\chi_{IO}N = 45.8$.¹² 7
- Figure 1.3.** Gyriodal network morphologies for non frustrated ABC triblock terpolymers: Core-shell double gyroid (Q^{230}), and alternating gyroid (Q^{214}). 8
- Figure 1.4.** Anionic synthesis scheme of poly(isoprene)-*block*-poly(styrene)-*block*-poly(ethylene oxide). 11
- Figure 1.5.** Schematic representation of structure direction with the triblock terpolymer ISO: Selective incorporation of inorganic or organic additives into the PEO phase through hydrogen bonding leads to increased hydrophilic volume fractions (swelling of the PEO phase), which results in the composition dependent formation of terpolymer morphologies with the additives confined in the hydrophilic PEO phase.²⁴ 13
- Scheme 2.1.** (a) Ternary volume fraction phase portrait that shows the reported ISO triblock terpolymer compositions and gyriodal hybrid compositions after incorporation of resols into the PEO block of the terpolymers. Inset shows the proposed mechanism of formation of resols-ISO organic-organic hybrids through self-assembly of the hydrogen bonded assembly. (b) Illustration of gyriodal structures and formation of gyriodal mesoporous carbon networks through decomposition of the triblock terpolymer and pyrolysis of the carbon precursor. The coating and backfilling steps are proposed routes to convert the carbon networks into two- and three-component functional nanocomposites. Top row: formation of core-shell double gyroid structure. Bottom row: formation of alternating gyroid structure. 24
- Figure 2.1.** Small-angle X-ray scattering (SAXS) patterns of double gyriodal organic-organic hybrids and double gyriodal mesoporous carbons: (a) GDMC#1-15, (b) GDMC#2-20, (c) GDMC#3-39 and (d) GDMC#4-12. Black traces after curing at 110-120 °C, red traces after pyrolysis at (a-c) 900 °C and

(d) 600 °C and blue traces after pyrolysis at (a-c) 1600 °C and (d) 1200 °C. The vertical ticks in the SAXS patterns indicate the expected peak positions of the double gyroid lattice (Q230)..... 26

Figure 2.2. (a) Thermogravimetric analysis curves of all 5 reported ISO-resols hybrids and pure phenol/formaldehyde resols. (b) Transmission electron micrograph of ISO#2-resols hybrid stained with osmium tetroxide (selectively stains poly(isoprene)), showing the double gyroidal (211) plane. Scanning electron microscopy (SEM) images of (c) GDMC#4-12-1600 (d) GDMC#1-15-900, (e) GDMC#2-20-900 and (f) GDMC#3-39-1600. Insets show images taken at higher magnification to demonstrate the difference in pore size and similarities in wall thickness between the 3 double gyroidal carbon materials derived from ISO#1-3..... 28

Figure 2.3. (a) Nitrogen sorption isotherms and (b) pore size distributions of GDMC#1-15-1600, GDMC#2-20-1600, GDMC#3-39-1600, and GDMC#4-12-1600. The pore size distributions were calculated using the BJH model for cylindrical pores..... 31

Figure 2.4. (a) Small angle X-ray scattering (SAXS) patterns, (b) scanning electron microscopy (SEM) image (inset: higher magnification of the (111) projection) after pyrolysis at 1600 °C and (c) nitrogen sorption isotherms with BJH pore size distributions (inset) of alternating gyroidal mesoporous carbons (G^AMC#5)..... 33

Figure 2.5. High-resolution transmission electron microscopy (HR-TEM) images of (a) G^DMC#2-20-1600, and (b) G^AMC#5-1600. Insets at a lower magnification of the same samples show the mesostructure. (c) Electron energy loss spectrum (EELS) of the carbon K-edge of G^DMC#2-20-1600. The spectrum is an average of six area spectra (10x10 nm²) taken at different spots of the sample. Raman spectra of powders of double gyroidal mesoporous carbons pyrolyzed at (d) 900 °C and (e) 1600 °C showing the evolution of the D- and G-bands. (f) High resolution – X-ray photoelectron spectroscopy (HR-XPS) data of the carbon K-edge of G^DMC#2-20-900, G^DMC#2-20-1600, and for comparison glassy carbon as well as carbon black, showing the decrease of the peak width at higher carbonization temperatures. 35

Figure 2.6. (a) Photographs of G^DMC#3-39-1200 monoliths from the top (bottom left) and conductively connected to silver wires (top left and right). Cross sectional SEM images of G^DMC#3-39-1200 monoliths of (b, left) 200 μm and (b, right) 50 μm thickness; higher magnification images at the edge of the surface (c) unexposed and (d) exposed to prior plasma treatment of the organic-organic hybrid. The insets in (c) and (d) show SEM images of the top surfaces only. 39

Figure S2.1. (a) Transmission electron microscopy image of ISO#2+resols following a synthetic procedure from the literature with only THF as the solvent and 1 hour stirring time only.¹⁵ (b) TEM image of the microtomed cross-section of a monolithic film mG^DMC#2-20-120 at the top surface. The lamellar sheets parallel to the surface are clearly distinguishable from the gyroidal bulk morphology. (c) Nitrogen sorption isotherms and (d) BJH pore size distributions of G^DMC#1-15-900, G^DMC#2-20-900, G^DMC#3-39-900..... 45

Figure S2.2. (a) Scanning electron microscopy image and (b) transmission electron microscopy image of G^DMC#1-15-1600 at low magnification showing a high degree of long range order and associated large gyroidal grain size of this carbon material. 46

Figure S2.3. (a) Scanning electron microscopy image of a 900 °C pyrolyzed hybrid material of ISO#5 and phenol/formaldehyde resols suggesting the formation of a disordered network. (b) Small angle X-ray scattering patterns of the hybrid before pyrolysis (lower trace) and after pyrolysis (upper trace) revealing poor structure formation in the hybrid and loss of periodicity after heat treatment. The material was prepared the same way as the G^DMCs. 47

Figure S2.4. (a) Powder X-ray diffraction patterns of G^DMC#2-20-900 (lower trace) and G^DMC#2-20-1600 (upper trace) showing the evolution of the graphitic (200) reflex at 22-26° and the (100) and (101) reflexes at 42-46°. The broad peaks indicate the existence of small graphitic clusters in the material. (b) Representative Raman spectra of powdered gyroidal mesoporous carbons heated at 900 °C (top, open squares, derived from ISO#2) and 1600 °C (bottom, open circles, derived from ISO#1) with peaks from peak fitting for the D and the G bands. 48

Figure S2.5. (a) Scanning electron microscopy image and small angle X-ray scattering (inset) pattern of ISO#1-Hex-1600 suggesting the formation of hexagonally oriented porous cylinders in a carbon matrix. The tick marks in the scattering pattern indicate the expected peak positions for hexagonal ordered cylinders. (b) Nitrogen sorption isotherms and BJH pore size distributions (inset) of ISO#1-Hex-1600 (solid line) and ISO#2-Hex-1600 (dashed line). (c) The Raman spectrum of ISO#1-Hex-1600 is similar to the spectra of the gyroidal mesoporous carbons pyrolyzed at 1600 °C. (d) High resolution – transmission electron microscopy image of ISO#2-Hex-1600 revealing the existence of small, bent graphitic clusters of a few stacked sheets with a length of 3–7 nm. Inset at a lower magnification of the same sample shows the mesostructure. 49

Figure 3.1. (a-d) Scanning electron microscopy (SEM) images of the four investigated ordered mesoporous carbon materials carbonized at 1600 °C: (a) Double gyroidal carbon with 15 nm pore size (G^DMC-15-1600°C), (b) single gyroidal carbon network (G^AMC-1600°C), (c) double gyroidal carbon with 39 nm pore size (G^DMC-39-1600°C), and (d) hexagonally packed cylindrical carbon (Hex-25-1600°C). The images have the same field of view for facile comparison. Insets in (a-d) show illustrations of the ordered carbon mesostructures and carbon-sulfur composites. (e) Nitrogen sorption isotherms and corresponding BJH pore size distribution (inset) of G^DMC-39-1600°C (red), G^AMC-1600°C (blue), and Hex-25-1600°C (black). (f) Discharge capacities of the first 100 cycles at 0.1C of 1:1 carbon-sulfur composites from G^AMC-1600°C (blue), Hex-25-1600°C (black), G^DMC-39-1600°C with (red) and without (purple) lithium nitrate as electrolyte additive. 60

Figure 3.2. (a) BJH pore size distributions of double gyroidal mesoporous carbons with 15 or 39 nm pore size and carbonized at 900 °C or 1600 °C. (b) Discharge capacities of the first 100 cycles at 0.1C of 1:1 carbon-sulfur composites from G^DMC-39-1600°C (red triangle), G^DMC-15-1600°C (green square), G^DMC-39-900°C (blue triangle), and G^DMC-15-900°C (black square), demonstrating the significant impact of carbonization temperature with little influence of mesopore size on cycling stability. (c) 1st and 50th charge and discharge curves at 0.1C of 1:1 carbon-sulfur composites from

G^DMC-15-1600°C (green) and G^DMC-15-900°C (black) demonstrating sharp discharge plateaus at the expected voltages without voltage decay over cycling for either of the host materials. 61

Figure 3.3. Structural and porosity characterization of CO₂-activated high temperature (1600 °C) derived gyroidal mesoporous carbons (aGDMC): (a) SEM image of 15 nm gyroidal mesoporous carbon after 10 hours of activation (aGDMC-15-10h) demonstrating good retention of gyroidal mesostructure during activation and roughening of the mesopore walls due to introduction of small nanopores. (b) Small-angle X-ray scattering (SAXS) patterns of GDMC-15-1600 °C before (black), and after CO₂-activation for 6 hours (aGDMC-15-6h, red), and for 10 hours (aGDMC-15-10h, blue). The patterns are shifted vertically for clarity. (c) Nitrogen sorption isotherms and (d) BJH pore size distributions (PSDs) of all activated double gyroidal mesoporous carbons. For comparison, the PSDs of the non-activated parent gyroidal mesoporous carbons are also plotted. The inset in (d) depicts an enlarged section at small pore width, showing the significant contribution of pores below 4 nm to the pore volume for aGDMC-15-10h. (e) Cumulative pore volume as a function of pore width analyzed using the NL-DFT model for slits on the nitrogen (black) and carbon dioxide (red) adsorption isotherms of aGDMC-15-10h, demonstrating the large pore volume contributed by the activation-induced small nanopores below 4nm..... 64

Figure 3.4. (a) Discharge capacities of the first 100 cycles at 0.1C of 1:1 carbon-sulfur composites from aG^DMC-15-6h (green triangle), aG^DMC-39-6h (blue square), aG^DMC-15-10h with TEGDME electrolyte (red triangle) and with DOL:DME electrolyte (black triangle). (b) 1st, 3rd, 30th and 100th charge and discharge curves at 0.1C of 1:1 carbon-sulfur composites of aG^DMC-15-10h with TEGDME electrolyte (discharge: red; charge: magenta) and DOL:DME electrolyte (discharge: black; charge: grey), indicating significant voltage decay of the discharge plateau and increase of the charge plateau over cycling in TEGDME. (c) Discharge capacities of first 100 cycles at 1C of 1:1 carbon-sulfur composites from aG^DMC-15-10h (black), G^DMC-15-1600°C (green), and G^DMC-15-900°C..... 66

Figure S3.1. Discharge capacities and coulombic efficiencies of first 100 cycles at 0.1C of 1:1 carbon-sulfur composites from G^AMC-1600°C (blue), Hex-25-1600°C (black), and G^DMC-39-1600°C with (red) and without (purple) lithium nitrate as electrolyte additive, and of a 2:1 carbon-sulfur composite from Hex-25-1600°C (green) with lithium nitrate as electrolyte additive. Solid symbols correspond to the discharge capacities, open symbols to the coulombic efficiencies. 73

Figure S3.2. Discharge capacities and coulombic efficiencies of the first 100 cycles at 0.1C of 1:1 carbon-sulfur composites from G^DMC-39-1600°C (red triangle), G^DMC-15-1600°C (green square), G^DMC-39-900°C (blue triangle), and G^DMC-15-900°C (black square). Solid symbols correspond to the discharge capacities, open symbols to the coulombic efficiencies..... 74

Figure S3.3. Carbon dioxide adsorption isotherm of the gyroidal mesoporous carbon with 15 nm pore size after CO₂-activation for 10 hours at 950 °C (aG^DMC-15-10h). 75

Figure S3.4. Discharge capacities and coulombic efficiencies of first 100 cycles at 0.1C of two separately prepared 1:1 carbon-sulfur composites from aG^DMC-15-10h. Solid symbols correspond to the discharge capacities, open symbols to the coulombic efficiencies..... 75

Figure S3.5. Nitrogen sorption isotherms and BJH pore size distributions of gyroidal carbon hosts with (red) and without (black) infiltrated sulfur (1:1 by weight) of G^DMC-15-900°C (a, d), G^DMC-15-1600°C (b, e), and aG^DMC-15-CO₂-10h (c, f). The BET surface areas of G^DMC-15-900°C, G^DMC-15-1600°C, and aG^DMC-15-CO₂-10h infiltrated with an equal amount of sulfur are 27, 26, and 291 m² g⁻¹, respectively, with mesopore volumes of 0.17, 0.15, and 0.83 cm³ g⁻¹ (calculated at a relative pressure of 0.99), respectively. The data confirms that the sulfur fills up most of the mesoporosity in the non-activated carbon hosts (900 °C and 1600 °C), while the small nanopores below 4 nm are filled in the highly activated gyroidal mesoporous carbon host (aG^DMC-15-CO₂-10h) and the larger 15 nm mesopores are still porous after sulfur infiltration. 76

Figure S3.6. Powder X-ray diffraction (PXRD) patterns of gyroidal mesoporous carbon filled with sulfur at 155 °C (1:1 by weight): G^DMC-15-1600°C (red), G^DMC-15-900°C (black), and aG^DMC-15-CO₂-10h (blue). A broad signal between 22 and 29 degrees was obtained for the non-activated carbon hosts (carbonized at 900 °C and 1600 °C). The main peaks of orthorhombic sulfur are in this range. However, from the data, it was determined that the sulfur is amorphous in all carbon hosts. 77

Figure S3.7. Scanning electron microscopy images at different magnifications of an electrode casted from aG^DMC-15-CO₂-10h infiltrated with Sulfur (1:1 by weight) with 10 wt% PVDF binder. Powder particles of the carbon hosts are between 100s of nanometers and 10s of microns in size... 77

Scheme 4.1. Illustration of the process employed for the formation of periodically ordered gyroidal mesoporous multifunctional titania nanocomposites, together with photographs of the resulting materials and gyroidal models illustrating the respective structures. From left to right: Monolithic 3D continuous gyroidal mesoporous resin; monolithic 3D continuous gyroidal mesoporous core-shell polymer-titania composite after atomic layer deposition (ALD) of amorphous titania exhibiting decreased deposition thickness away from the top surface; monolithic 3D continuous gyroidal mesoporous crystalline anatase titania (top) and monolithic 3D continuous gyroidal mesoporous core-shell carbon-titania composite (bottom) after heat-treatment at 600 °C in air or inert atmosphere, respectively. The insets show double gyroidal unit cells of the respective structures with indication of the 3D pore (yellow; left) and titania (white; middle and right) connectivity. 87

Figure 4.1. (a) Titania EDX line scans from the surface of the as-made polymer-titania composites with 250 deposition cycles. Cross-section SEM images of TiO₂/C-0.4s (b), TiO₂/C-1s-direct (c), and TiO₂/C-1s-soak (d) after removal of the polymeric template by heat treatment. These images directly visualize the increase of ALD depth with increasing pulse and soaking time. Insets depict SEM images of the titania shell structure at higher magnification. Note that in (b) the titania films resulting from both surfaces after removal of the polymer template are collapsed onto each other, whereas in (c) and (d) only one of these films is shown. 88

Figure 4.2. SEM images of the double gyroidal mesoporous polymer template (a), TiO₂/C-1s-soak after pyrolysis at 600 °C under nitrogen at distances of 1 μm (b) and 6.5 μm (c) from the surface, and after calcination at 600 °C in air at the surface (d), as well as at 5 μm (e) and 10 μm (f) from the surface, showing a homogeneous titania layer thickness over the first ~7 μm from the template surface. Insets in (a) and (b) show SEM simulations of the double gyroid matrix (211) plane (a) and the double gyroid shell along the [110] zone axis (b). Overlays in (b) and (c) are guides for the eye

for a clear identification of the carbon (black) and titania (grey) phases. Insets in (d-f) show parts of the respective SEM images at higher magnification facilitating direct titania layer thickness comparison. 90

Figure 4.3. (a) XRD patterns of TiO₂/C-1s-direct heat treated under different conditions. (b) Raman spectra of TiO₂/C-1s-direct before (blue) and after pyrolysis in nitrogen at 600 °C (red) or 900 °C (black) showing the evolution of D- and G-bands, typical for disordered carbon materials. (c) SEM image of TiO₂/C-1s-direct after pyrolysis in nitrogen at 900 °C revealing the random growth of titania crystallites in the ordered carbon framework. 91

Figure 4.4. (a) XRD patterns of TiO₂/C-1s-direct-125 heat-treated under different conditions. SEM images of TiO₂/C-1s-direct-125 (b) and TiO₂/C-1s-direct (c) close to the top surface after pyrolysis at 600 °C in nitrogen showing the titania layer thickness dependence on the ALD cycle number. ... 92

Figure S4.1. Photographs of a large, flexible gyroidal mesoporous resin template (a+b) and of the Beneq TFS200 ALD system used for part of the samples described in this report, indicating the sample position for the normal "flow over" and the "directed flow" procedure..... 96

Figure 5.1. Nano-integrated 3D-battery assembly from gyroidal mesoporous carbon monoliths. (a) Carbon monoliths (blue, second from left) are obtained from BCP self-assembly directed gyroidal hybrid formation (left, showing minority BCP domains) with resols precursors and subsequent carbonization. Nanoscopic gyroidal majority domains of the carbon anode (blue) are conformally coated with a nanoscopic polymer electrolyte layer (green), which in turn is back-filled with a nanoscopic cathode composite (red). (b) Photographs of gyroidal mesoporous carbon monoliths as-made (top) and attached to a wire in edge-on geometry (bottom). (c,d) SEM images of a gyroidal mesoporous carbon monolith exhibiting uniform thickness of approximately 60 μm (c), surfaces with open and accessible gyroidal mesoporosity (c, inset), and uniformly structured cross-section (d). 106

Figure 5.2. Electropolymerization of ultrathin solid polymer electrolyte on mG^DMC anode. (a) Cyclic voltammogram (CV) of mG^DMC anode in the phenol electropolymerization solution. The broad oxidation peak of the first cycle disappears completely after 10 cycles. (b) Current-time traces of selected potentiostatic deposition pulses at 0.6 V vs. Ag/Ag⁺ showing the decrease in double layer and oxidation current. (c) CVs after pulsed potentiostatic PPO deposition in the same solution showing only double layer current without a phenol oxidation peak. (d-f) SEM images of mG^DMC anode before (d) and after (e,f) pulsed potentiostatic electropolymerization of PPO. Freshly cleaved cross-sections are shown in (d,e) and the surface in (f). Insets show cross-sections at higher magnification..... 108

Figure 5.3. Performance test of ultra-thin PPO polymer electrolyte layer. (a) Resistance measurements using a two-electrode configuration of the wire-connected mG^DMC anode before (black) and after (red) PPO electropolymerization showing an increase in resistance by more than 5 orders of magnitude. Note, the current of the PPO coated monoliths was multiplied by a factor of 10⁵ for easier comparison. (b) Discharge and charge curves of a PPO-coated mG^DMC anode demonstrating reversible lithiation-delithiation through the PPO-layer. 109

Figure 5.4. Cathode composite infiltration. (a) Resistance measurements of insulating double gyroidal mesoporous polymer monoliths (mG^DMP, black) back-filled with PEDOT (red), and sulfur and PEDOT (blue) using a two-probe configuration with contacts on either monolith surface. (b) Cross-sectional SEM image of a sulfur-PEDOT backfilled mG^DMP indicating good infiltration efficiency. (c) Cross-sectional SEM image of a sulfur-PEDOT backfilled PPO-coated mG^DMC (3D-battery) and EDX line scan of the sulfur signal across the film (line scan position indicated by black arrow in SEM and shown in Figure S5.4a)..... 111

Figure 5.5. Performance test of an all-nano-integrated 3D-battery. (a) Photograph and schematic of a fully assembled 3D-battery after contacting the cathode phase on the top surface and before lithiation (alligator clip for the lithium metal can be seen on the right). (b) Discharge curve of the sulfur-PEDOT phase vs. lithium metal in liquid electrolyte at 0.125 mA cm⁻². (c) Discharge capacities of the tested cycles. The cycle conditions (voltage window and current rate) are indicated in the graph. (d) Discharge curves of the first two cycles that were run in the potential window of 1-3.5 V at a current of 0.125 mA cm⁻² (11th and 12th cycle total). (e) Discharge curves of selected cycles that were run in the potential window of 1.5-3.5 V at a current of 0.125 mA cm⁻² (13th-20th cycle total). (f) Discharge curves of selected cycles that were run in the potential window of 1.5-3.6 V at a current of 0.25 mA cm⁻² (22nd-30th cycle total)..... 112

Figure S5.1. (a) Small-angle X-ray scattering pattern of mG^DMC material after pyrolysis at 1100 °C. The markings indicate expected positions for the *Ia-3d* space group of the double gyroid morphology with (100) spacing of 131 nm. (b) BJH pore size distribution derived from the nitrogen adsorption isotherm of gyroidal mesoporous carbon material after pyrolysis at 1600 °C..... 118

Figure S5.2. (a) Current-time traces of selected potentiostatic pulses at 0.6 V vs. Ag/Ag⁺ of gyroidal mesoporous carbon in the supporting electrolyte demonstrating no change over 200 pulses. (b) CVs after the potentiostatic pulses in the same solution for the supporting electrolyte (red) and after PPO deposition (black). (c) Current-time traces of selected potentiostatic deposition pulses of PPO on a flat carbon substrate (highly oriented pyrolytic graphite, HOPG) at 0.6 V vs. Ag/Ag⁺ showing the very fast decrease in double layer and oxidation current over pulses. (d) CVs after pulsed potentiostatic PPO deposition in the same solution of mG^DMC and HOPG showing only double layer current without a phenol oxidation peak (current of the HOPG is increased by a factor of 10 for clarity)..... 119

Figure S5.3. Charge and discharge curves of the first two cycles (a) and capacities of the first 22 cycles (b) of powdered gyroidal mesoporous carbon in a standard coin cell versus lithium metal. (c) Resistance measurements using a two-probe configuration of the wire-connected gyroidal mesoporous carbon anode without PPO coating (black) and HOPG after PPO electropolymerization (red) showing the increase in resistance by more than 5 orders of magnitude. Note, the current of the PPO coated HOPG was multiplied by a factor of 10⁵ to facilitate comparison. (d) Discharge and charge curves of PPO-coated HOPG demonstrating reversible lithiation-delithiation through the PPO-layer. 120

Figure S5.4. (a) Cross-sectional SEM image of the 3D-battery described in the main text with the arrow showing the position of the line scan plotted in Figure 5.4. (b) Cross-sectional SEM image of the

3D-battery described in the main text with the points showing the position of the quantified spectra described in the text. (c) First charge curve described in the text of the 3D-battery to 3 V at 0.125 mA cm^{-2} . (d) Current/potential-time traces of the first 10 cycles run between 1 and 3 V at 0.125 mA cm^{-2} with 15 mins rest between each applied charge or discharge current. (e) Current/potential-time traces of the 10th-20th cycle run between 1 V (11th+12th) or 1.5 V (13th-20th) and 3.5 V at 0.125 mA cm^{-2} with 15 mins rest between each applied charge or discharge current. 121

Figure S5.5. (a) Charge-discharge curves of the first two cycles that were run in the potential window of 1-3.5 V at a current of 0.125 mA cm^{-2} (11th and 12th cycle total). (b) Charge and discharge curves of selected cycles that were run in the potential window of 1.5-3.5 V at a current of 0.125 mA cm^{-2} (13th-20th cycle total). (c) Discharge curves of selected cycles that were run at a current of 0.125 mA cm^{-2} (11th-20th cycle total). (d) Charge and discharge curves of selected cycles that were run in the potential window of 1.5-3.6 V at a current of 0.25 mA cm^{-2} (21st-30th cycle total). (e) Charge and discharge capacities of the tested cycles. The cycle conditions (voltage window and current rate) are indicated in the graph. (f) Cycle efficiencies (coulombic efficiencies) of the tested cycles. The cycle conditions (voltage window and current rate) are indicated in the graph. 122

LIST OF TABLES

| | |
|---|----|
| Table 2.1. Triblock terpolymer compositions and resols loadings for gyroidal organic-organic hybrids.. | 23 |
| Table 2.2. Structural characteristics of gyroidal mesoporous carbons. | 30 |
| Table 3.1. Triblock terpolymer compositions, resols loadings for ordered mesoporous carbons, and carbon sample notations used in this study. | 58 |
| Table 3.2. Structural characteristics of ordered mesoporous carbons. | 59 |
| Table 3.3. Structural characteristics of activated gyroidal mesoporous carbons..... | 64 |
| Table S3.1. Capacity values of the first, third and 100th cycle, initial capacity decay and per cycle decay rate of selected 1:1 (by weight) carbon-sulfur composites at a rate of 0.1C, and tapped density of the gyroidal carbon-sulfur composites with 15 nm mesopores. Tapped density was measured after tapping of the composites 200 times. | 74 |
| Table 4.1. Summary of the ALD conditions employed for the formation of ordered mesoporous multifunctional multicomponent titania nanocomposites. | 86 |

CHAPTER 1

INTRODUCTION

Abstract

The focus of the work described in this thesis is the synthesis, characterization, and functionalization of bicontinuous mesoporous carbon materials with large tunability over structural and porosity characteristics. Organic-polymeric self-assembly of block copolymers and carbon precursors is employed as a synthesis tool. Backfilling, surface coating and combinations thereof are investigated to obtain carbon based multifunctional nanohybrids with controlled morphology for applications in energy storage. This chapter introduces the fundamental concepts of polymers and block copolymer self-assembly, structure direction, and synthetic procedures. Each following chapter contains a concise introduction that provides a summary of the relevant literature and background.

Macromolecules

Polymers or macromolecules, two terms that are used interchangeably, consist of a number of smaller molecules as repeating units, called monomers. If the addition or removal of one or a few of these repeating units does not lead to a significant change in properties of the molecule, it can generally be referred to as a polymer. As a general guideline, polymers are often considered to be molecules with a molecular weight of at least 1000 g mol^{-1} but the molecular weight threshold is not sharply defined and is rather arbitrary. Polymers are generally divided in two types of macromolecules: synthetic and biological polymers. While most polymers can be synthesized in a chemical laboratory, biological polymers can also be found in nature, synthetic ones cannot. Synthetic polymers usually consist of a much smaller variety of repeating units per macromolecule than their biological counterparts.¹

Early and important examples of synthetic polymers are Bakelite, a phenol/formaldehyde resin, synthesized by the chemist Leo Bakeland and commercialized in the early 20th century; neoprene rubbers and polyamide, widely known under its commercial name *nylon*, synthesized in the early 1930s by Carothers; and polyethylene, synthesized with organometallic catalysts by Ziegler in the 1950s that led to the mass production of polymers. In the beginning of the 20th century, scientists thought of polymers as agglomerations of smaller molecules that were held together by an unknown force. It was Staudinger in 1920 who proposed that polymers like rubber are big molecules that consist of a large number of covalently bonded repeating units. Staudinger's theory was not accepted at first, but was later proven right.

In 1929, the synthesis of macromolecules was divided into two classes by Carothers: step-growth polymerization and chain-growth polymerization.² The stepwise reaction occurs between polyfunctional molecules, often including the elimination of a small molecule. Chain-growth happens in polymerizations of monomers with double bonds or rings, where an initiation step is needed to add one monomer after the other to the chain. Direct reactions between monomers do not happen during this kind of polymerization.

Two structural categories can be assigned to non-cross-linked macromolecules, branched and linear.^{3,4} Branched polymers consist of one or more merging points, where more than two chains come

together. The highest degree of branching is achieved in so-called dendrimers, where every monomer has at least three direct bonds to other monomers. Star-shaped and comb-like polymers are other examples of branched polymers, the earlier has three or more polymer chains connected at one center point, and the latter consists of smaller chains grown off a larger polymeric backbone. Polymers with only one type of repeating unit are called homopolymers. If more than one monomer type is used as a building unit of a macromolecule, copolymers are achieved. These copolymers can be alternating, with perfect monomer alteration, random or statistic, where the monomers are not in any particular order, as well as ordered as block copolymers, in which chains of one single monomer are covalently linked into blocks. In addition to the chemical properties typically coming from the monomers, a polymer is also characterized by the total number of repeating units per chain, the so-called degree of polymerization. Since within a given polymer sample this number varies for different chains, the degree of polymerization is expressed as an average. The molecular weight is usually expressed as the number average, M_n , and the weight average, M_w , as defined in equations (1.1.1) and (1.1.2).

$$M_n = \frac{\sum M_i N_i}{\sum N_i} \quad (1.1.1)$$

$$M_w = \frac{\sum M_i^2 N_i}{\sum M_i N_i} \quad (1.1.2)$$

$$PDI = M_w / M_n \quad (1.1.3)$$

A value that describes the polydispersity of the weight distribution is the so-called polydispersity index (PDI), given in (1.1.3). The closer this value is to 1, the narrower the weight distribution of the polymer is. The molecular weight distribution can usually be influenced by the choice of polymerization technique and its synthesis parameters.^{1,4}

Block Copolymers

Thermodynamics of polymer mixtures: Most chemically different polymers form two distinct phases when mixed together. This behavior of polymer mixtures is called macrophase separation and is

well understood and described thermodynamically: A system of two components in thermodynamic equilibrium is described by the Gibbs free energy of mixing, ΔG_m , given by equation (1.2.1):

$$\Delta G_m = \Delta H_m - T\Delta S_m \quad (1.2.1)$$

In polymeric systems, the heat of mixing, ΔH_m , and the entropy of mixing, $T\Delta S_m$, is usually described by the Flory-Huggins expressions (1.2.2) and (1.2.3):

$$\Delta H_m = nRT\chi_{AB}f_Af_B \quad (1.2.2)$$

$$\Delta S_m = -nR \left(\frac{\phi_A}{N_A} \ln(\phi_A) + \frac{\phi_B}{N_B} \ln(\phi_B) \right) \quad (1.2.3)$$

where f_A and f_B describe the volume fractions of polymer A and B in the mixture and χ_{AB} is the so-called Flory-Huggins interaction parameter that describes the local interaction between the monomers of polymer A and B.³ This results in the Flory-Huggins expression for the Gibbs free energy of mixing of polymer blends (1.2.4):

$$\Delta G_m = nRT \left(\frac{f_A}{N_A} \ln(f_A) + \frac{f_B}{N_B} \ln(f_B) + \chi_{AB}f_Af_B \right) \quad (1.2.4)$$

The entropic contribution to the free energy of mixing is always negative (volume fractions f_A and f_B are less than 1), but since in polymers the number of monomers (N_A and N_B) is high, the entropy of mixing is extremely small and decreases with a higher degree of polymerization (N). Therefore, the mixing behavior of polymers majorly depends on the Flory-Huggins interaction parameter and occurs almost exclusively for negative values of χ_{AB} at high degrees of polymerization. Negative χ_{AB} parameters only occur for specific A-B monomer interactions such as hydrogen bonding, ionic or π -electron interactions. A well-known and industrially used example for a polymer mixture with negative interaction parameter is the blend of poly(styrene) and poly(2,6-dimethyl-1,4-phenylenether) (PPE). In general, the mixing behavior of polymers is temperature-dependent and in a simple Flory-Huggins approach for purely enthalpic local interactions, χ_{AB} is inversely proportional to T . In many cases, this

leads to miscibility or immiscibility of polymers at higher temperatures with positive or negative Flory-Huggins interaction parameters, respectively.³ Polymer mixtures that are not miscible phase separate into two phases, each of which is rich in one of the components with a small amount of the other component dissolved in it. The morphology of these macrophase separated mixtures depends on the fabrication method. A slow quench of the mixture from a miscible to an immiscible state typically results in nucleation and growth of one of the phases as spheres in a matrix of the other phase. A fast quench can lead to spinodal decomposition with a metastable bicontinuous morphology. The length scale of the phase separation is 100s of nanometers to micrometers and typically increases with time.

Diblock copolymers: The simplest case of a block copolymer (BCPs) is a diblock copolymer, in which two chemically different polymer chains are covalently bonded to each other. Macro phase separation cannot occur in this case due to the covalent linkage. The generally unfavorable interaction between A-blocks and B-blocks is avoided by so-called microphase separation, where equal blocks from separate polymers form one phase. This kind of separation is limited by the entropic penalty from the stretching of the polymer chains away from the interface between the two blocks. Since the entropic term in (1.2.4) is proportional to N^{-1} and the general enthalpic term to χ_{AB} , the product χN dictates the microphase separation. Theoretical descriptions of block copolymer microphase separation have been provided for the so-called weak ($\chi N \sim 10$) and strong ($\chi N \gg 10$) segregation limit by Leibler and Semenov, respectively.^{5,6}

In the microphase separated state, block copolymers form different morphologies with length scales in the nanometer regime depending on the volume fraction, f , of the blocks and χN . Structure formation is caused by balancing between minimization of interfacial area, block incompressibility, and chain stretching dependent entropic penalty. Theoretical and experimental phase diagrams are described by various groups, e.g. Matsen and Bates.⁷⁻⁹ The generally observed morphologies for diblock copolymers are closed-packed spheres (S_{CP}), bcc-spheres (Q_{Im-3m} , Q^{229}), hexagonally packed cylinders (H, HEX), bicontinuous gyroid (Q_{Ia-3d} , Q^{230}) and lamellar (L). Schematic representations of these

morphologies are given in Figure 1.1. With the exception of the gyroid, all morphologies are characterized by a constant mean curvature of the interface between the different micro-domains.

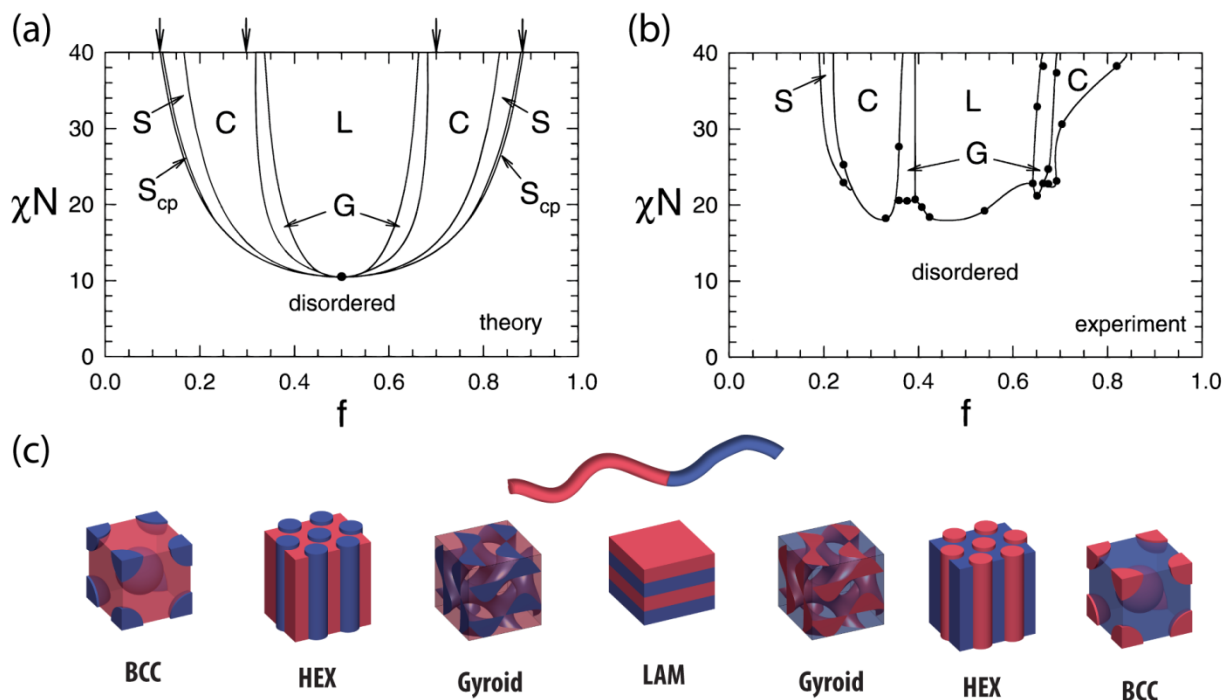


Figure 1.1. (a) Theoretical phase diagram of a diblock copolymer and (b) experimental phase diagram of poly(styrene-*block*-isoprene) (PS-PI). (c) Equilibrium morphologies for an AB-diblock copolymer for different volume fractions of A (f : Volume fraction of B; Dis: Disordered; Scp: Closed-packed spheres; S/BCC: Body-centered cubic; C/HEX: Hexagonally packed cylinders; G: Gyroid; L/LAM: Lamellar).¹⁰ Apart from the lamellar morphology, the block with the higher volume fraction forms a matrix the other block is embedded in, forming a 1-D (spheres), 2-D (hexagonal, lamellar) or 3D (gyroid) structure. The difference between theoretical and experimental phase diagrams is mostly caused by non-uniform aspect ratios of the different monomers, and thermal and concentration fluctuations, especially in the weak segregation limit. As described above, the Flory-Huggins interaction parameter is temperature dependent, which typically leads to an order-disorder transition at elevated temperatures (T_{ODT}), above which the blocks start mixing with each other.

Linear Triblock copolymers: In more complex block copolymers like ABC-triblock, multiblock or starblock copolymers, the variety of morphologies increases. This work focuses on linear ABC-triblock terpolymers, which are introduced in more detail here. In linear ABC-triblock terpolymers, three chemically different polymer chains are covalently bonded to form one linear chain. This leads to the formation of two block junctions, A-B and B-C, and three different interaction parameters: χ_{AB} , χ_{BC} , and χ_{AC} , as well as three volume fractions: f_A , f_B , and f_C . Two types of triblock terpolymers are

distinguished: non-frustrated and frustrated ones. In polymers without frustration, the interaction parameter between A and C is higher than between A and B or B and C, respectively ($\chi_{AB} \sim \chi_{BC} \ll \chi_{AC}$). This leads to structure formation without an interface between A and C micro domains. In frustrated polymers, χ_{AC} is smaller than at least one of the two others. Frustrated polymers show the same basic morphologies as non-frustrated systems, but because of a more favorable A-C interface, also numerous other morphologies like hexagonal perforated lamellae and decorated phases of the usual morphologies with A-C interfaces are found.¹¹

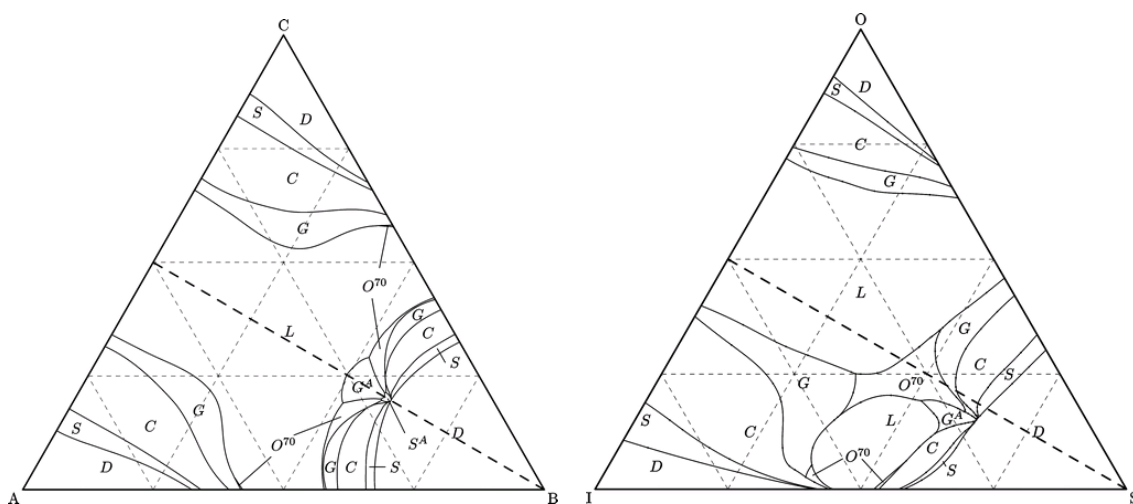


Figure 1.2. ABC triblock terpolymer phase diagrams. Left: Theoretical phase map of an idealized triblock terpolymer with equal statistical segment lengths for each block and with $\chi_{AC}N = 35$, $\chi_{AB}N = \chi_{BC}N = 13$. Right: Theoretical phase map for a model ISO triblock terpolymer, with statistical segment lengths $b_I = 6.0 \text{ \AA}$, $b_S = 5.5 \text{ \AA}$, and $b_O = 7.8 \text{ \AA}$ and interaction parameters $\chi_{IS}N = 11.0$, $\chi_{SO}N = 14.2$, and $\chi_{IO}N = 45.8$.¹²

In this work, the focus lies on non-frustrated triblock terpolymers, in particular poly(isoprene)-*block*-poly(styrene)-*block*-poly(ethylene oxide) (ISO). This ABC triblock terpolymer has been extensively studied both theoretically and experimentally by the Bates group.¹²⁻¹⁴

In comparison to the diblock copolymer morphologies, core-shell analogous morphologies are formed in the triblock system, with the B-block separating the A- and C-phases, such as core-shell double gyroid (Q^{230}) or core-shell hexagonally packed cylinders. In addition to these morphologies, alternating morphologies like alternating Gyroid (Q^{214}) and the orthorhombic O^{70} were achieved in simulations and

experiments, with symmetries that are only possible with triblock terpolymer systems.¹⁴ The two observed gyroid phases for ABC triblock terpolymers are schematically shown in Figure 1.3.

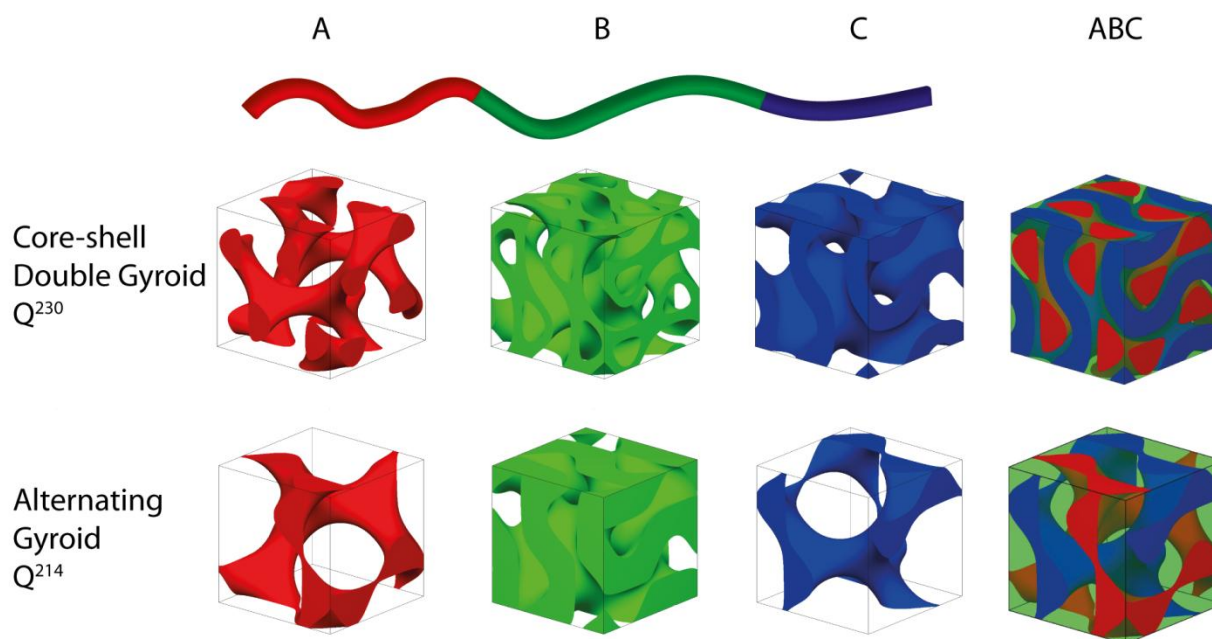


Figure 1.3. Gyroidal network morphologies for non frustrated ABC triblock terpolymers: Core-shell double gyroid (Q^{230}), and alternating gyroid (Q^{214}).

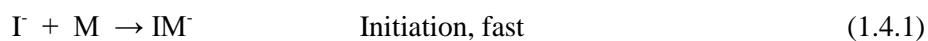
The advantage of linear ABC triblock terpolymers over diblock copolymers is the better accessibility of the bicontinuous morphologies and a greater variety in applications as templates. Since the three blocks are chemically different, they can be removed and backfilled or blended selectively. Many materials can be arranged and combined in this way into well ordered structures with unit cell sizes of 10 nm to 100 nm.

Anionic Polymerization

Living chain growth polymerizations offer precise control over molecular weight with low polydispersity and allow for the polymerization of multiple distinct polymer blocks in sequence. One of these polymerization methods is anionic polymerization, which is suitable for the polymerization of e.g. vinyl monomers and cyclic ethers. The polymerization is initiated by an anion that propagates on the chain end as a carbanion or oxyanion, respectively. Initiation and chain propagation reactions are nucleophilic addition of the anion to the monomer. The counter cation and the degree of anion-cation

dissociation significantly influence the reactivity and kinetics of the polymerization. Depending on solvent, cation, and temperature, the ion pair can be present in different types: a polarized, covalent bond, a contact ion pair or a solvated, free ion pair. Initiators are often alkali metals or their organic compounds. Initiation is classified into two different basic types: nucleophilic addition of organometallic compounds of alkali metals, and electron transfer from free alkali metals. The latter usually follows a mechanism that includes the formation of radical anions that dimerize to dianions and the chains propagate in two directions. The reaction mechanism can follow a free addition mechanism of the monomer to the free anion, a coordination mechanism or an insertion mechanism with pi-complex formation. The latter is the case when a polarized covalent bond is present like with lithium organic compounds in nonpolar solvents. When no impurities are present, anionic polymerization does not show termination or transfer reactions, which in combination with high initiation rate compared to the chain propagation, leads to equally growing chains that stay living after consumption of all monomers. The living chains act as macroinitiators for additionally added monomers and block copolymers can easily be grown.¹

Kinetics and Molecular Weight Distributions: The mechanism of anionic polymerizations can be divided into a fast initiation reaction, followed by a propagation reaction and finalized with an externally induced termination:



A complete and fast initiation leads to living active species with one monomer anion attached to the initiator. Since there is no internal termination reaction, the concentration of living chains equals the concentration of initiator $[I]_0$ and the reaction rate is proportional to the monomer concentration $[M]$, which leads to an exponential decrease of monomer concentration with time t .

$$v_p = -d[M]/dt = k_p [I]_0 [M] \quad (1.4.4)$$

$$[M] = [M]_0 \exp(-k_p [I]_0 t) \quad (1.4.5)$$

The degree of polymerization at time $t = \tau$ is given by

$$P_n = ([M]_0 - [M]_\tau) / [I]_0. \quad (1.4.6)$$

When all monomers are used up and without any termination or transfer reactions the final degree of polymerization is given by the ratio of monomer to initiator. The distribution of the degree of polymerization and molecular weight corresponds to a Poisson distribution. This leads to a decreasing polydispersity for increasing molecular weight ($PDI = 1 + 1/P_n$).^{1,25}

Polymerization of poly(isoprene)-*block*-poly(styrene)-*block*-poly(ethylene oxide): Poly(isoprene)-*block*-poly(styrene)-*block*-poly(ethylene oxide) (ISO) is synthesized in a stepwise anionic polymerization that requires a solvent and counter cation exchange. All steps involving organic anions are conducted under strict exclusion of oxygen, water and any proton sources to avoid side reactions and termination. Figure 1.5 shows the reaction pathway of the anionic polymerization of the triblock terpolymer. Isoprene is initiated by *sec*-butyl lithium in benzene. Due to the polarized covalent bond of organolithium compounds, unlike organometallic compounds of higher alkali metals, they are soluble in hydrocarbons. This results in an insertion mechanism and leads to the preferential formation of poly(1,4-isoprene) in non-polar solvents. The ratio of 1,4- and 3,4-isomers can be determined with H^1 -NMR. In the next step, styrene is polymerized using the poly(isoprenyl) anion as the macroinitiator. The living polymer chain is end-functionalized via addition of an excess of ethylene oxide and terminated with methanolic hydrochloric acid as a proton source. The ethylene oxide anion cannot polymerize with lithium as counter ion, because of the strong bonding between lithium and oxygen, which leads to the addition of only one ethylene oxide monomer at the end of each living chain. In order to polymerize ethylene oxide, a cation exchange must be accomplished and the solvent is exchanged to the more polar tetrahydrofuran (THF). The cation exchange is accomplished through repeated washing of the polymer solution with water and extraction of lithium chloride formed during termination, followed by the addition of excess potassium chloride. The diblock copolymer end-capped with a hydroxyl group is reinitiated through deprotonation with potassium naphthalenide to form the living potassium alkoxide chain end, which is used as the

macroinitiator for the anionic ring opening polymerization of ethylene oxide. The polymerization of ethylene oxide is terminated again with methanolic hydrochloric acid, which yields the hydroxyl end-functionalized triblock terpolymer.

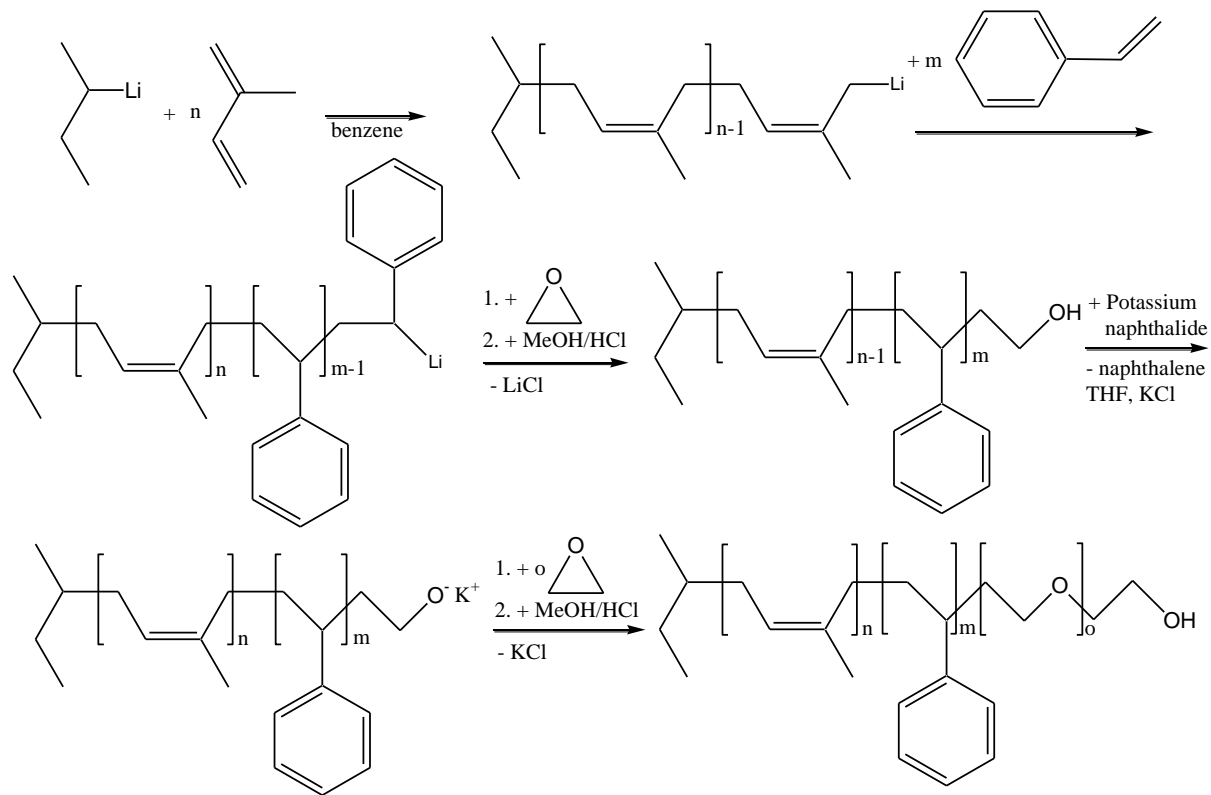


Figure 1.4. Anionic synthesis scheme of poly(isoprene)-*block*-poly(styrene)-*block*-poly(ethylene oxide).

Block Copolymer Hybrids

Hybrids of block copolymers and inorganic materials are of particular interest to create composites with a well-defined structure on the scale of 10 – 100 nm. The self-assembly of block copolymers as structure-directing moieties for inorganics has been employed extensively over the last two decades using metal oxide sol-gel additives, metal or semiconducting nanoparticles, and ceramic precursors.^{15–22} After removal of the organic material the hybrids lead to nanoporous and mesostructured functional materials, e.g. aluminosilicates, orthosilicates, transition metal oxides, non-oxide ceramics and metals. These kinds of nanomaterials can find a great variety of applications, such as catalysis, energy storage, energy conversion, plasmonics, and membranes.

In order to structure-direct additives in block copolymer hybrids, selective and attractive interactions between one block and the additive are required. These interactions include hydrogen bonding as well as polar, coordination, and ionic interactions. In the case of nanoparticles, these interactions can be between a block and the particle surface or ligands associated with the nanoparticle surface. A further requirement for successful structure direction with block copolymers results in a size limitation for the additive. It has been shown in nanoparticle systems that nanoparticles have to be smaller than the radius of gyration of the attracting block to prevent entropy-driven nanoparticle segregation.²¹

The structure of microphase separated block copolymers depends on the volume fraction of the blocks and the interaction parameters. By selectively blending materials like inorganic nanoparticles with block copolymers, the volume fractions as well as the interaction parameters of the phases change. An extensive study has been reported by Garcia *et al.* on the system of aluminosilicates and poly(isoprene)-*block*-poly(ethylene oxide) (PI-PEO) with varying BCP composition and BCP-inorganic ratios leading to a variety of ordered hybrid mesostructures.²³ The selective swelling of one block with inorganic additives in BCP-inorganic hybrid systems allows for the formation of different morphologies using the same polymer by addition of different amounts of inorganic precursor as schematically shown in Figure 1.5. Morphologies with either inorganic minority or majority volume fractions are accessible using block copolymers with the inorganic-attracting block holding a minority volume fraction. The use of ABC triblock terpolymers offers the advantage of attaining bicontinuous morphologies like double gyroid more frequently. These structures are of special interest because the achievable porosity and the inorganic networks are continuous in three dimensions. For example in device applications these bicontinuous structures make macroscopic structure alignment unnecessary, and pore blockage can be mitigated.

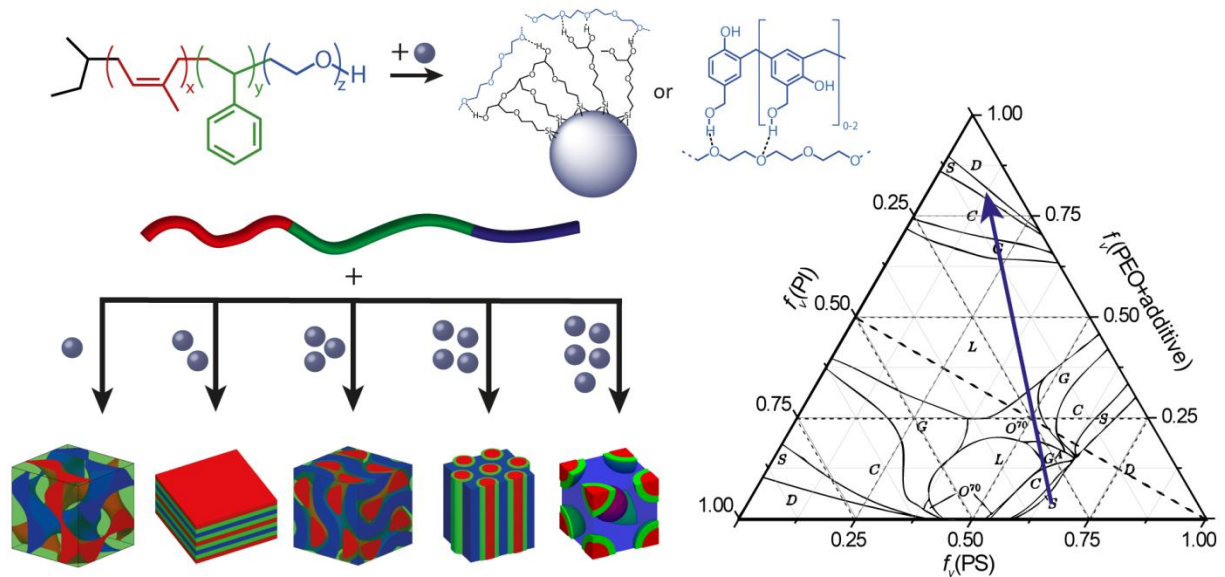


Figure 1.5. Schematic representation of structure direction with the triblock terpolymer ISO: Selective incorporation of inorganic or organic additives into the PEO phase through hydrogen bonding leads to increased hydrophilic volume fractions (swelling of the PEO phase), which results in the composition dependent formation of terpolymer morphologies with the additives confined in the hydrophilic PEO phase.²⁴

Thesis outline

In energy storage and conversion nanostructured materials hold tremendous academic and technological promise. This is due primarily to the very high surface or interface to volume ratios of nanosized materials or composites, respectively. While the diversity of reported nanostructured and nanoporous materials is vast, establishing precise structure-property relationships for nanomaterials in energy storage and conversion devices still remains a major challenge in the field. In order to understand the influence of nanostructure on performance, controlled and ordered morphologies are essential, as single crystals are essential for the understanding of bulk properties of materials. Block copolymer self-assembly directed inorganic nanomaterials formation provides a synthetic pathway for precise control over all relevant material's parameters, including composition/chemistry, dimensionality, and porosity. Furthermore, the potential of nanostructured functional materials and hybrids for energy storage applications is not fully explored yet. This thesis describes my work on triblock terpolymer directed three-

dimensionally ordered mesoporous carbon materials and carbon-based nano-hybrids as rationally derived energy storage materials and architectures.

In chapter 1, I describe my work on the synthesis of ordered mesoporous carbons (OMCs) from triblock terpolymer structure direction with independently tunable morphology and porosity characteristics. To that end I developed a materials system consisting of poly(isoprene)-*block*-poly(styrene)-*block*-poly(ethylene oxide) (PI-*b*-PS-*b*-PEO, ISO) that is synthesized via anionic polymerization for precise control over composition and nanostructure, combined with phenol- or resorcinol-formaldehyde resols as carbon precursors. I demonstrate that morphology, porosity, as well as pore and unit cell size are independently controllable by rationally designing BCP composition, molar mass, and polymer-to-precursor ratio.

In chapter 2, the use of my OMCs for a comprehensive structure-property relationship study on the influence of carbon characteristics of carbon-sulfur composite cathodes in lithium-sulfur batteries is described. In this methodological investigation, I describe the influence of morphology, mesopore size, carbonization temperature, and microporosity from physical activation on the sulfur-capacity retention over cycling.

Chapter 3 expands the ordered nanocomposite concept to a rationally designed ordered mesoporous multifunctional two-component core-shell nanohybrid. The proximity of multiple functional materials on the nanoscale results in large interfaces with potential synergistic effects important for various electrochemical devices. I describe the use of atomic layer deposition (ALD), a well-established thin film technique, to deposit titania on my free-standing monolithic gyroidal OMCs. I demonstrate the applicability and limitations of titania ALD on nanoporous bulk substrates.

Chapter 4 describes the integration of all battery components on the nanoscale into a macroscopic solid-state device. Combining anode, electrolyte, and cathode materials on the nanoscale, significant battery performance improvements have been proposed in the past. Realization of such integrated three-dimensional (3D) devices has proven to be most difficult, however. Indeed a working battery with nanoscale dimensions of all components has not been demonstrated to date. The chapter describes details

of the successful “total synthesis” of such nanohybrids with all three battery components integrated into a nanostructure and subsequently reports on first 3D-battery performance evaluations.

The thesis concludes with an outlook of potential future directions for research on porous carbon materials and their use in advanced fabrication techniques, as well as three-dimensionally integrated energy storage devices.

REFERENCES

- (1) Lechner, M. D.; Gehrke, K.; Nordmeier, W. H. *Makromolekulare Chemie*; 3rd ed.; Springer-Verlag: Basel, 2003.
- (2) Carothers, W. H. Studies on Polymerization and Ring Formation. I. An Introduction to the General Theory of Condensation Polymers. *J. Am. Chem. Soc.* **1929**, *51*, 2548–2559.
- (3) Strobl, G. *The Physics of Polymers*; 3rd ed.; Springer-Verlag: Berlin Heidelberg, 2007.
- (4) Sun, S. F. *Physical Chemistry of Macromolecules*; 2nd ed.; John Wiley & Sons: Hoboken, NJ, 2004.
- (5) Leibler, L. Theory of Microphase Separation in Block Copolymers. *Macromolecules* **1980**, *13*, 1602–1617.
- (6) Semenov, A. N. Theory of Block Copolymer Interfaces in the Strong Segregation Limit. *Macromolecules* **1993**, *26*, 6617–6621.
- (7) Matsen, M. W.; Bates, F. S. Unifying Weak- and Strong-Segregation Block Copolymer Theories. *Macromolecules* **1996**, *29*, 1091–1098.
- (8) Matsen, M.; Schick, M. Microphase Separation in Starblock Copolymer Melts. *Macromolecules* **1994**, *27*, 6761–6767.
- (9) Khandpur, A. K.; Foerster, S.; Bates, F. S.; Hamley, I. W.; Ryan, A. J.; Bras, W.; Almdal, K.; Mortensen, K. Polyisoprene-Polystyrene Diblock Copolymer Phase Diagram near the Order-Disorder Transition. *Macromolecules* **1995**, *28*, 8796–8806.
- (10) Matsen, M. W. The Standard Gaussian Model for Block Copolymer Melts. *Journal of Physics: Condensed Matter*, 2001, *14*, R21–R47.
- (11) Bates, F. S.; Fredrickson, G. H. Block {Copolymers—Designer} Soft Materials. *Phys. Today* **1999**, *52*, 32.
- (12) Tyler, C. A.; Qin, J.; Bates, F. S.; Morse, D. C. {SCFT} Study of Nonfrustrated {ABC} Triblock Copolymer Melts. *Macromolecules* **2007**, *40*, 4654–4668.

- (13) Chatterjee, J.; Jain, S.; Bates, F. S. Comprehensive Phase Behavior of Poly(isoprene-B-Styrene-B-Ethylene Oxide) Triblock Copolymers. *Macromolecules* **2007**, *40*, 2882–2896.
- (14) Epps, T. H.; Cochran, E. W.; Bailey, T. S.; Waletzko, R. S.; Hardy, C. M.; Bates, F. S. Ordered Network Phases in Linear Poly(isoprene-B-Styrene-B-Ethylene Oxide) Triblock Copolymers. *Macromolecules* **2004**, *37*, 8325–8341.
- (15) Hoheisel, T. N.; Hur, K.; Wiesner, U. B. Block Copolymer-Nanoparticle Hybrid Self-Assembly. *Prog. Polym. Sci.* **2015**, *40*, 3–32.
- (16) Chen, H.; Schmidt, D. F.; Pitsikalis, M.; Hadjichristidis, N.; Zhang, Y.; Wiesner, U.; Giannelis, E. P. Poly(styrene-Block-Isoprene) Nanocomposites: Kinetics of Intercalation and Effects of Copolymer on Intercalation Behaviors. *J. Polym. Sci. Part B Polym. Phys.* **2003**, *41*, 3264–3271.
- (17) Yang, P. D.; Zhao, D. Y.; Margolese, D. I.; Chmelka, B. F.; Stucky, G. D. Generalized Syntheses of Large-Pore Mesoporous Metal Oxides with Semicrystalline Frameworks. *Nature* **1998**, *396*, 152–155.
- (18) Chiu, J. J.; Kim, B. J.; Kramer, E. J.; Pine, D. J. Control of Nanoparticle Location in Block Copolymers. *J. Am. Chem. Soc.* **2005**, *127*, 5036–5037.
- (19) Li, Z.; Sai, H.; Warren, S. C.; Kamperman, M.; Arora, H.; Gruner, S. M.; Wiesner, U. Metal Nanoparticle/Block Copolymer Composite Assembly and Disassembly. *Chem. Mater.* **2009**, *21*, 5578–5584.
- (20) He, J.; Sill, K.; Xiang, H. Self-Directed Self-Assembly of Nanoparticle / Copolymer Mixtures. *Nature* **2005**, *404*, 55–59.
- (21) Warren, S. C.; Messina, L. C.; Slaughter, L. S.; Kamperman, M.; Zhou, Q.; Gruner, S. M.; DiSalvo, F. J.; Wiesner, U. Ordered Mesoporous Materials from Metal Nanoparticle-Block Copolymer Self-Assembly. *Science (80-.)*. **2008**, *320*, 1748–1752.
- (22) Bockstaller, M. R.; Lapetnikov, Y.; Margel, S.; Thomas, E. L. Size-Selective Organization of Enthalpic Compatibilized Nanocrystals in Ternary Block Copolymer/particle Mixtures. *J. Am. Chem. Soc.* **2003**, *125*, 5276–5277.
- (23) Garcia, B. C.; Kamperman, M.; Ulrich, R.; Jain, A.; Gruner, S. M.; Wiesner, U. Morphology Diagram of a Diblock {Copolymer–Aluminosilicate} Nanoparticle System. *Chem. Mater.* **2009**, *21*, 5397–5405.

- (24) Stefik, M.; Mahajan, S.; Sai, H.; Epps, T. H.; Bates, F. S.; Gruner, S. M.; DiSalvo, F. J.; Wiesner, U. Ordered Three- and Five-Ply Nanocomposites from {ABC} Block Terpolymer Microphase Separation with Niobia and Aluminosilicate Sols. *Chem. Mater.* **2009**, *21*, 5466–5473.
- (25) Stevens, M. P. *Polymer Chemistry: An Introduction*; 3rd ed.; Oxford University Press, New York: New York, 1999.
- (26) Hunt, B. J.; Holding, S. R. *Size Exclusion Chromatography*; Chapman and Hall: New York, 1989.

CHAPTER 2

SYNTHESIS AND CHARACTERIZATION OF GYROIDAL MESOPOROUS CARBONS AND CARBON MONOLITHS WITH TUNABLE ULTRALARGE PORE SIZE

Abstract

Ordered mesoporous carbons (OMC) with high pore accessibility are of great interest as electrodes in energy conversion and storage applications due to their high electric and thermal conductivity, chemical inertness and low density. The metal- and halogen-free synthesis of gyroidal bicontinuous mesoporous carbon materials with uniform and tunable pore sizes through bottom-up self-assembly of block copolymers thus poses an interesting challenge. Four double gyroidal mesoporous carbons (G^D MC) with pore sizes of 12 nm, 15 nm, 20 nm, and 39 nm were synthesized using poly(isoprene)-*block*-poly(styrene)-*block*-poly(ethylene oxide) (ISO) as structure directing triblock terpolymer and phenol-formaldehyde resols as carbon precursors. The highly ordered materials were thermally stable to at least 1600 °C with pore volumes of up to 1.56 cm³ g⁻¹. Treatment at this temperature induced a high degree of sp²-hybridization and low microporosity. Increasing the resols:ISO ratio led to hexagonally packed cylinders with lower porosity. A single gyroid carbon network with high porosity of 80 vol% was obtained using a similar synthesis strategy. Furthermore, we present a method to fabricate monolithic materials of the gyroidal carbons with macroscopic shape and thickness control that exhibit an open and structured surface with gyroidal features. The gyroidal materials are ideally suited as electrode materials in fuel cells, batteries and supercapacitors as their high, three-dimensionally connected porosity is expected to allow for good fuel or electrolyte accessibility and to prevent total pore blockage.

Adapted with permission from Werner, J. G., Hoheisel, T. N., Wiesner, U.: Synthesis and Characterization of Gyroidal Mesoporous Carbons and Carbon Monoliths with Tunable Ultralarge Pore Size, *ACS Nano* **8** (1), 731-743 (2014). Copyright 2013 American Chemical Society.

Introduction

Chemical and physical properties like good electrical and thermal conductivity, chemical resistance and inertness as well as low density combined with high surface area and porosity make porous carbon materials a preferred material in a broad field of applications, such as electrodes in batteries and fuel cells, and gas adsorbents.¹⁻³ Ordered mesoporous carbons (OMC) have retained a lot of attention since their first synthesis in 1999, where silica templates were used as a mold.^{4,5} This hard-templating method is very versatile and dimensions are only limited by the availability of the silica template, but it is tedious due to multiple step synthesis and the removal of the silica template with hazardous chemicals.⁶⁻¹² In 2004, Liang *et al.* reported the first soft-templated OMC.¹³ They used structure direction from the block copolymer poly(styrene)-*block*-poly(4-vinylpyridine) (PS-*b*-P4VP) with resorcinol through solvent evaporation induced self-assembly (EISA) and subsequent gas-solid reaction with gaseous formaldehyde. The resulting carbon thin films of up to 1 μm thickness showed hexagonally ordered cylindrical pores with a pore size of 33.7 nm after pyrolysis. Since this first report, extensive studies on soft-templated OMCs have been performed using the surfactant-like block copolymers Pluronic. Due to the small molar mass of these structure directing molecules, however, the accessible pore size range was limited to less than 4 nm, which was increased to 15–16 nm by molecular swelling agents, as well as by using carbon onions or carbon black additives.¹⁴⁻¹⁷ Only a few reports on the use of block copolymers with molar masses up to 45.6 kDa for the synthesis of OMCs with larger pore sizes were published.¹⁸⁻²¹ Pore sizes up to 37 nm have been achieved using poly(styrene)-*block*-poly(ethylene oxide) (PS-PEO) with poly(styrene) homopolymer addition as pore expander and phenolic resols as the carbon precursors.²² The mesostructures achieved with these polymers were inverse micellar and hexagonally packed cylinders. Ordered, bicontinuous networks, such as gyroidal mesoporous carbons, have only been reported using Pluronic, and recently using the structure directing block copolymer poly(ethylene oxide)-*block*-poly(ϵ -caprolactone) (PEO-*b*-PCL).^{15,23} However, the reported material showed only a small pore size of 11 nm and low porosity.

Here we report the tunable synthesis of two gyroidal mesoporous carbon morphologies through the EISA process of the structure directing triblock terpolymer poly(isoprene)-*block*-poly(styrene)-*block*-poly(ethylene oxide) (ISO) with phenol- or resorcinol-formaldehyde resols as carbon precursors. We demonstrate the tunability of the materials characteristics such as porosity, pore size and mesostructure by rational design of the soft template. Organic-organic hybrids with the core-shell double gyroid and hybrids with the alternating gyroid morphology result in a double gyroidal carbon matrix and a single gyroidal carbon network after pyrolysis, respectively. Pore tunability was achieved through variation of the triblock terpolymer composition and the respective polymer to resols ratios. The pore size tunability is demonstrated by using three ISOs with similar composition but different molar mass. The bicontinuous, ordered carbon materials show surprisingly good structure retention after heat treatment at temperatures as high as 1600 °C. This high temperature stability allows for thermal tunability of the microstructure of the carbon as well as the microporosity. A report by Wang *et al.* showed the retention of only local order of a hexagonally packed cylindrical carbon mesostructure at 1800 °C with structural collapse at higher temperatures by scanning electron microscopy.²⁴ However, the long range order of the material treated at these high temperatures was not retained according to small-angle X-ray scattering (SAXS). For the ordered gyroidal mesoporous carbons reported here, up to six clearly identifiable SAXS peaks remained, demonstrating, for the first time, long range order retention at 1600 °C.

Much research in electrochemical energy storage focuses on the enhancement of rate capability during charge and discharge of supercapacitors and batteries. Due to better electrolyte accessibility and shorter solid state diffusion length, nanoporous materials have been proven to enhance the rate of charge and discharge while keeping the capacity loss small. However, the standard device design of these electrochemical devices employs powders of the active materials and conductive additives, held together in a film by a polymeric binder. The contact resistance between the micron sized particles causes large ohmic losses, especially at high frequency operations. Therefore, monolithic electrodes without particle-to-particle resistance are highly desirable for future energy storage devices. There are several reports in the literature for ordered mesoporous monolithic carbon materials, usually by hard-templating.¹² Two

soft-templating approaches have also been described, *i.e.* hierarchical macro-mesoporous carbon monoliths from hydrothermal synthesis and EISA.^{25–29} The macropores and only micron sized mesoporous walls in the hierarchical carbons assure sufficient release pathways for the decomposition gases and good strain relaxation upon carbonization. In the EISA derived monoliths, carbon-silica composites have been employed. The mechanically robust silica prevents collapse of the monolith during carbonization, but it makes the undesirable extra step of silica removal necessary.³⁰ These monoliths are typically irregular with ill-defined macroscopic structure and they exhibit unstructured surfaces with broad pore size distributions. In contrast, here we present a silica-free soft-templating method to produce well-defined, ordered, purely mesoporous carbon monoliths with tunable macroscopic dimensions. Furthermore, we report a process to achieve surfaces with narrow pore size distributions that exhibit the same ordered gyroidal features as the bulk of the material.

Results and Discussion

Characterization of mesostructure: The formation of mesoporous carbon materials by block copolymer structure direction of phenol- or resorcinol- formaldehyde carbon precursors is illustrated in Scheme 2.1. Five poly(isoprene)-*block*-poly(styrene)-*block*-poly(ethylene oxide) (ISO) terpolymers with polydispersity indices of 1.04–1.07 (Table 2.1) were synthesized using anionic polymerization to serve as the soft template for the preparation of gyroidal mesoporous carbon structures by evaporation induced self-assembly (EISA). Briefly, in this process a solution of the carbon precursor and the terpolymer template is slowly evaporated to dryness, leading to microphase separation of the block terpolymer. The hydrophilic carbon precursor forms hydrogen bonds with the hydrophilic poly(ethylene oxide) (PEO) block of the terpolymer, which ensures that the carbon precursor is embedded in the PEO block, selectively swelling this phase.³¹ The organic-organic hybrid film is subsequently annealed to cure the phenolic resols. Further heat treatment under inert atmosphere condenses the resols to a highly cross-linked resin while the block copolymer decomposes (Scheme 2.1 and Figure 2.2a) yielding an ordered

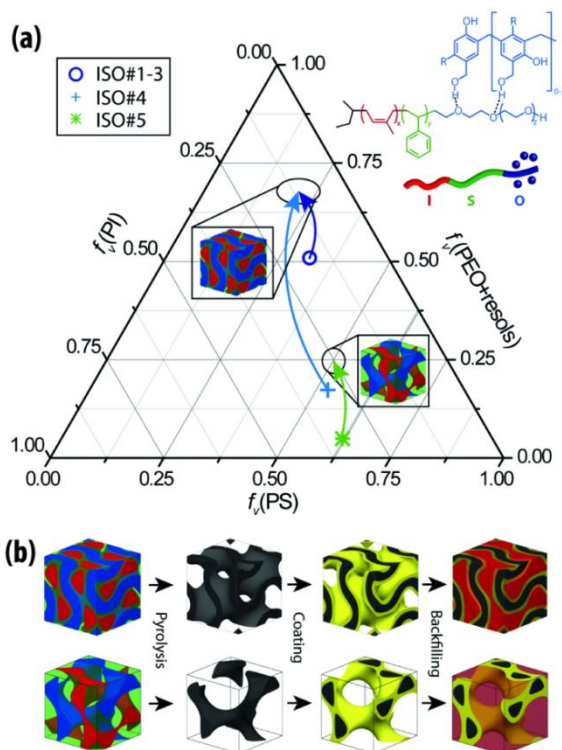
Table 2.1. Triblock terpolymer compositions and resols loadings for gyroidal organic-organic hybrids.

| Polymer | GMC | M_N^a / g/mol | PDI | $f_v(\text{PI})^b$ | $f_v(\text{PS})^b$ | $f_v(\text{PEO})^b$ | Resols: ISO ^c |
|---------|------------------------|-----------------|------|--------------------|--------------------|---------------------|-----------------------------|
| ISO#1 | G ^D MC#1-15 | 38,891 | 1.06 | 17.7 vol% | 32.5 vol% | 49.8 vol% | 0.58 : 1 |
| ISO#2 | G ^D MC#2-20 | 55,993 | 1.06 | 16.7 vol% | 31.2 vol% | 52.1 vol% | 0.73 : 1 |
| ISO#3 | G ^D MC#3-39 | 108,311 | 1.07 | 17.7 vol% | 31.6 vol% | 50.7 vol% | 0.50 : 1 |
| ISO#4 | G ^D MC#4-12 | 27,019 | 1.05 | 30.1 vol% | 52.6 vol% | 17.3 vol% | 1.80 : 1 |
| ISO#5 | G ^A MC#5 | 68,959 | 1.04 | 33.1 vol% | 62.0 vol% | 4.9 vol% | 0.32 : 1 |

^a determined by combination of ¹H-NMR and GPC; ^b determined by ¹H-NMR; ^c weight ratio.

gyroidal mesoporous polymeric resin. Pyrolysis at temperatures above 600 °C leads to carbonization of the resin to form the desired gyroidal mesoporous carbons with tailored porosity and pore sizes. During the EISA process, microphase separation occurs when a critical concentration of the polymer/additive is reached in the solution. This process is very sensitive to both the processing parameters and the precursor molecules employed. First, well-defined mesostructures only form in systems in which the different blocks have sufficiently high Flory-Huggins interaction parameters.^{38,32} Second, it is critical to ensure strong and selective hydrogen bonding between the resols and the PEO for selective swelling of this block. The morphology that is formed depends on the volume fractions of the separated microphases and their interaction parameters. With decreasing amount of solvent, the mobility of the polymer decreases until it reaches a kinetically trapped state. If the additive, in this case the resols, is not bonded strongly enough to one of the polymer blocks, the interface between the hydrophilic and hydrophobic phases is unsharp. This leads to unstructured microphase separation or poor structure formation and no long range order. In order to form well defined gyroidal organic-organic hybrids, the solvent system and precursors as well as the mixing time and casting temperature had to be optimized. While protocols reported in the literature for block copolymer-resols structure direction¹⁹⁻²¹ resulted in limited structure formation and order (Figure S2.1a), optimization of the above mentioned parameters yielded well-defined organic-organic ISO-resols hybrids (Figure 2.2b), highlighting the importance of the conditions for film-casting.

In our case, the desired gyroidal morphology was only achievable using a casting solution stirred for 24 hours in a solvent system of tetrahydrofuran (THF) and chloroform and elevated casting temperatures for solvent evaporation (Figure 2.2b-f). Third, to assure structural stability of the ordered nanomaterial during decomposition of the triblock terpolymer template, high enough loading of the cross-linkable precursor is crucial in soft-templating methods, as opposed to hard-templating methods. On the other hand, high porosity and large specific surface areas are desirable for most applications, favoring lower loadings. We specifically designed our triblock terpolymers with different compositions to assure thermal stability and structural integrity through sufficient connectivity of the carbon precursor while yielding tunable porosities between 32 vol% and 80 vol%.



Scheme 2.1. (a) Ternary volume fraction phase portrait that shows the reported ISO triblock terpolymer compositions and gyroidal hybrid compositions after incorporation of resols into the PEO block of the terpolymers. Inset shows the proposed mechanism of formation of resols-ISO organic-organic hybrids through self-assembly of the hydrogen bonded assembly. (b) Illustration of gyroidal structures and formation of gyroidal mesoporous carbon networks through decomposition of the triblock terpolymer and pyrolysis of the carbon precursor. The coating and backfilling steps are proposed routes to convert the carbon networks into two- and three-component functional nanocomposites. Top row: formation of core-shell double gyroid structure. Bottom row: formation of alternating gyroid structure.

Double gyroidal mesoporous carbon (G^D MC): Three triblock terpolymers, ISO#1–ISO#3, with a PEO volume fraction of approximately 50 vol% and molar mass of 39 kDa (ISO#1), 56 kDa (ISO#2), and 108 kDa (ISO#3), and a fourth triblock terpolymer ISO#4, with a PEO volume fraction of 17 vol% and a molar mass of 27 kDa, were used for the preparation of ordered mesoporous carbons (OMCs) with double gyroid morphology (Q^{230} , $Ia\bar{3}d$) (Table 2.1 and Scheme 2.1a). These materials were designated G^D MC#X-Y-Z, where X represents the terpolymer number, Y the approximate final pore size and Z the highest temperature at which the material was heat treated. In the organic-organic hybrid, the hydrophilic phase, consisting of PEO and resols, formed the matrix that separates the two interpenetrating gyroidal poly(isoprene)-*block*-poly(styrene) core-shell networks (top row in Scheme 2.1b). In Figure 2.1, the well resolved small angle X-ray patterns of the hybrids are shown (lowest trace in each graph). For hybrids from polymers ISO#1, ISO#2 and ISO#4, multiple higher order peaks consistent with the space group Q^{230} were observed, indicating a high degree of long range order. The SAXS pattern for the hybrid obtained from the largest terpolymer ISO#3 showed a broad first order peak with a shoulder on the higher q -side together with broad higher order peaks, making structural assignments based on SAXS data only challenging. The lower resolution of the SAXS pattern for this hybrid as compared to the SAXS patterns of the hybrids from ISO#1, ISO#2 and ISO#4 is due to squeezing of all reflexes into a smaller q range as well as a decreased degree of long range order, as expected for a higher molar mass polymer. In the EISA process, as the solvent evaporates, the hybrids self-assemble into their structures, once a certain concentration is reached. During this self-assembly, the solvent swells the polymer and therefore provides mobility to the polymer chains. When the solvent concentration drops, the system starts to freeze, since the casting temperature is below the glass-transition temperature of the poly(styrene) block. Casting or thermal annealing at temperatures higher than the glass-transition temperature of poly(styrene) is not possible, since it would induce cross-linking of the phenolic resols. Higher molar mass polymers have lower mobility and therefore yield smaller grain sizes and lower long range order than smaller molar mass structure directing polymers. Therefore, the best resolved SAXS patterns are obtained with the smallest triblock terpolymers ISO#1 and ISO#4. Moreover, the different molar masses of the three ISO polymers

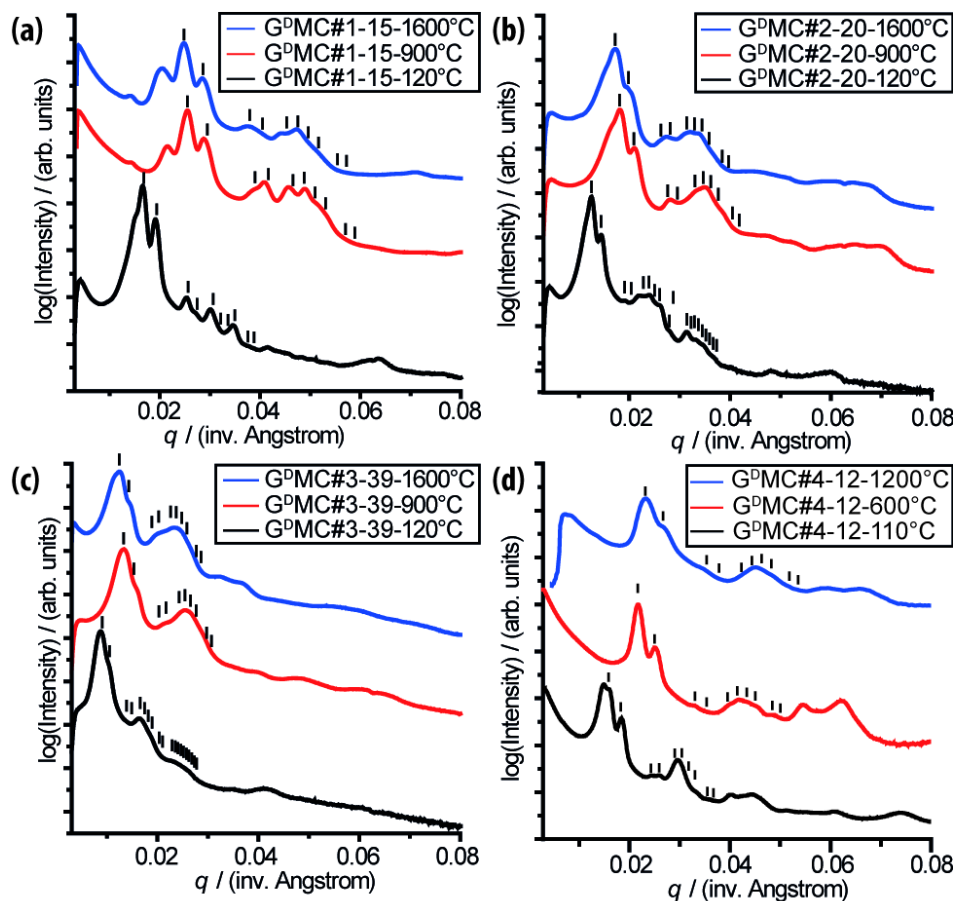


Figure 2.1. Small-angle X-ray scattering (SAXS) patterns of double gyroidal organic-organic hybrids and double gyroidal mesoporous carbons: (a) G^DMC#1-15, (b) G^DMC#2-20, (c) G^DMC#3-39 and (d) G^DMC#4-12. Black traces after curing at 110-120 °C, red traces after pyrolysis at (a-c) 900 °C and (d) 600 °C and blue traces after pyrolysis at (a-c) 1600 °C and (d) 1200 °C. The vertical ticks in the SAXS patterns indicate the expected peak positions of the double gyroid lattice (Q₂₃₀).

with similar composition, ISO#1-3, resulted in different characteristic structural length scales of the prepared hybrids. A clear trend of the first order peak that corresponds to the (211) plane of the Q²³⁰ space group to lower q -values was observed when comparing the patterns for G^DMC#1-15-120, G^DMC#2-20-120 and G^DMC#3-39-120. This decrease corresponds to an increase in the unit cell size of the cubic morphology from 92 nm to 123 nm to 169 nm for hybrids of ISO#1, ISO#2 and ISO#3, respectively, as expected from the increasing molar mass of the three structure directing triblock terpolymers. The organic-organic hybrid of ISO#4 and resols gave a gyroidal unit cell size of 96 nm, only 4% larger than G^DMC#1-15-120. Even though ISO#4 has a 31% smaller molar mass with a more than two times lower PEO fraction than ISO#1, the three times higher resols loading of G^DMC#4-12 made the two hybrids very

comparable in composition of the three phases, PI, PS and PEO-resols. This lead to two double gyroidal materials with similar characteristic length scales, but significantly different compositions of the hydrophilic PEO-resols phase, that is G^DMC#4-12 has a much higher resols:PEO ratio than G^DMC#1-15 (Scheme 2.1a).

The hybrids were subsequently heated under inert atmosphere to decompose the terpolymer and carbonize the resols. First, the hybrids were heated to 600 °C at a rate of 1 °C min⁻¹ and held at that temperature for 3 hours to ensure sufficient structure stabilization. For further carbonization, two temperatures were investigated: 900 °C for 3 hours, often employed in literature reports of mesoporous carbons, and 1600 °C for 1 hour, both temperatures reached with a heating rate of 5 °C min⁻¹.¹⁹ Upon heat treatment and carbonization, the structure shrinks significantly but is well retained. This is apparent from the well resolved SAXS patterns that, compared to the parent hybrids, were shifted to higher *q*-values corresponding to smaller unit cell sizes, but retained higher order reflections consistent with a cubic gyroid lattice (middle and upper traces in Figure 2.1a-d and Table 2.2). According to the decrease of the unit cell, the structures shrank approximately 30% during decomposition of the polymer and carbonization of the resols. Considering this large change in size, the thermal stability of the mesostructure of these materials is remarkable. To the best of our knowledge, this is the first report of soft-templated materials with long-range ordered and periodic mesostructure after treatment at temperatures as high as 1600 °C. The lack of an appropriate furnace inhibited further exploration of the thermal stability at even higher temperatures of these materials. It is noteworthy, that the shrinkage of the structure during heat treatment at 900 °C (for 3 hours) was larger than during the heating at 1600 °C (for 1 hour). We assume that after the stabilization at 600 °C, the phenolic resin condensed very slowly. A temperature plateau at 900 °C could allow the mesostructure to relax or condense for a longer time compared to material that is directly heated to 1600 °C and hardened quickly. Additionally, for ISO#1-derived G^DMC#1-15, the SAXS patterns after heat treatment showed an extra peak at lower *q*-values. The peak matched the (200) peak that is forbidden in the cubic double gyroid morphology. This suggests anisotropic shrinkage of the structure during heat treatment as has been observed for oxide materials in

the past.³³ The SAXS pattern of G^DMC#4-12-600 shows multiple higher order peaks consisting with the double gyroid morphology. After heat treatment at 1200 °C, the peaks broadened. The gyroidal unit cell of the ISO#4-resols hybrid shrank from 96 nm to 71 nm and 66 nm after pyrolysis at 600 °C and 1200 °C, respectively. The characteristic length scale of G^DMC#4-12-1200 and G^DMC#1-15-1600 only differed by 8%.

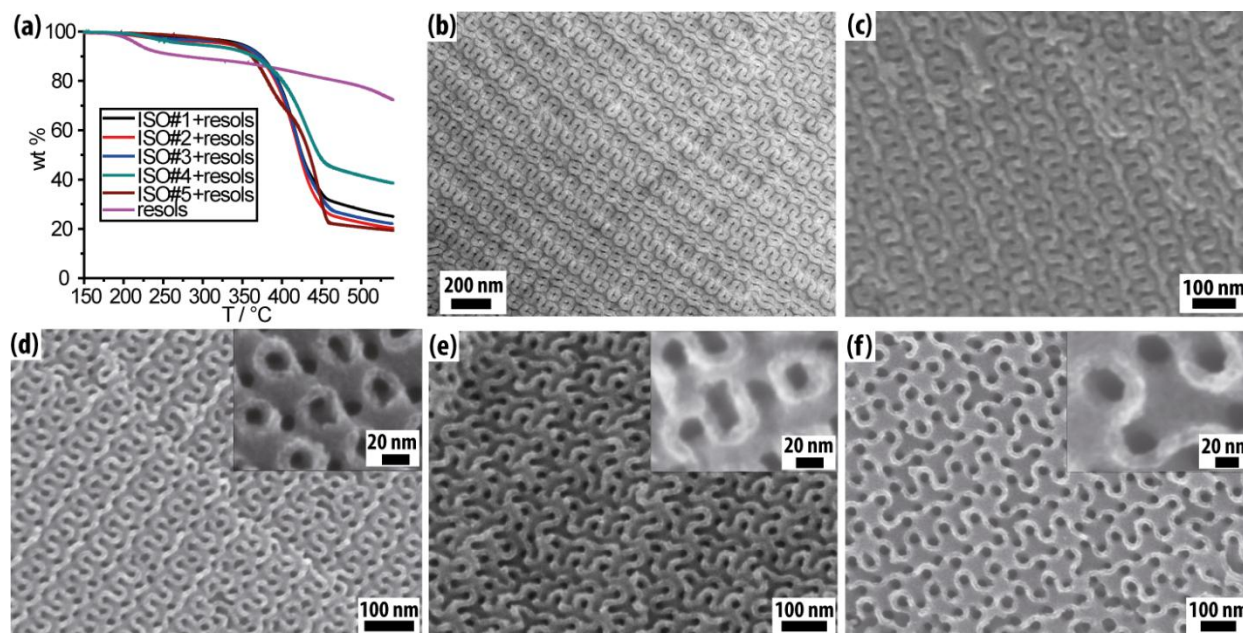


Figure 2.2. (a) Thermogravimetric analysis curves of all 5 reported ISO-resols hybrids and pure phenol/formaldehyde resols. (b) Transmission electron micrograph of ISO#2-resols hybrid stained with osmium tetroxide (selectively stains poly(isoprene)), showing the double gyroidal (211) plane. Scanning electron microscopy (SEM) images of (c) GDMC#4-12-1600 (d) GDMC#1-15-900, (e) GDMC#2-20-900 and (f) GDMC#3-39-1600. Insets show images taken at higher magnification to demonstrate the difference in pore size and similarities in wall thickness between the 3 double gyroidal carbon materials derived from ISO#1-3.

The remarkable structure control as evidenced by SAXS and the assignments to gyroidal structures in all four materials was corroborated by scanning electron microscopy (SEM), see Figure 2.2c-f. The SEM images show the well defined (211) projection (double wavy pattern) of the double gyroid morphology for all four materials. The extensive long range order of GDMC#1-15-1600, apparent from the well resolved SAXS pattern was also evident from electron microscopy analyses. Grains with diameters of multiple microns were seen in SEM that were connected by thin lamellae grain boundary regions. During crushing of the samples, the grain boundaries are mechanically the weakest points of the structure and

mesostructurally “single crystalline” particles with sizes of more than 5 microns were observed in TEM (Figure S2.2). While electron microscopy analysis indicated a low porosity for the G^DMC#4-12-1200 materials derived from ISO#4 with low PEO fraction and high resols loading, a high porosity was suggested for the materials derived from ISO#1-3 with high PEO fractions and low resols loadings. Thus, the thickness of the pore walls of the latter three investigated double gyroidal mesoporous carbons were measured to be between 10 nm and 15 nm with wall-to-wall distances of approximately 15 nm, 19 nm and 36 nm for G^DMC#1-15-1600, G^DMC#2-20-1600 and G^DMC#3-39-1600, respectively(see insets in Figure 2.2d, e and f). In contrast to these high pore-to-wall thickness ratios, the wall thickness and wall-to-wall distance of G^DMC#4-12-1600 was measured to be 20 nm and 12 nm, respectively.

Nitrogen sorption analysis of the carbonized samples confirmed the presence of mesoporous structures with narrow pore size distributions and tunable porosity. Figure 2.3a shows nitrogen sorption isotherms of all four G^DMCs pyrolyzed at 1600 °C. The isotherms show typical type-IV curves with H₁-type hysteresis and sharp capillary condensation above relative pressures of 0.9. The sharp capillary condensation shifted to higher relative pressures with increased molar mass of the terpolymer template. The amount of nitrogen adsorbed at low relative pressure was twice as high for the carbon materials treated at 900 °C (Figure S2.1b) compared to the ones treated at 1600 °C, indicating a much higher specific surface area. Analysis according to the Brunau-Emmet-Teller (BET) theory resulted in specific surface areas of 529 m² g⁻¹, 606 m² g⁻¹, 551 m² g⁻¹ and 692 m² g⁻¹ for G^DMC#4-12-900, G^DMC#1-15-900, G^DMC#2-20-900 and G^DMC#3-39-900, respectively (Table 2.2). More than two thirds of these specific surface areas were constituted by microporosity. However, pyrolysis of the mesoporous carbons at 1600 °C resulted in a large decrease of the contribution of the micropores to the specific surface area, while the mesopore surface area (obtained through subtraction of the micropore surface area from the total surface area) remained almost unchanged (Table 2.2). At this temperature, the micropore surface

Table 2.2. Structural characteristics of gyroidal mesoporous carbons.

| GMC | Pore size ^a / nm | Pore volume ^b (micropore volume ^c) / cm ³ /g | BET surface area (micropore area ^c) / m ² /g | d- spacing ^d / nm | Carbon : oxygen ratio ^e | Graphitic cluster size ^f / Å |
|-----------------------------|--------------------------------|--|---|------------------------------------|--|---|
| G ^D MC#1-15-900 | 15 ± 2 | 0.89 (0.2) | 606 (427) | 60 | 88:12 | 26.8 ± 3.0 |
| G ^D MC#1-15-1600 | 16 ± 2 | 0.80 (0.06) | 318 (136) | 62 | 91:9 | 37.4 ± 3.0 |
| G ^D MC#2-20-900 | 19 ± 2 | 0.78 (0.19) | 551 (403) | 86 | 88:12 | 27.0 ± 4.1 |
| G ^D MC#2-20-1600 | 21 ± 2 | 0.80 (0.03) | 196 (72) | 89 | 92:8 | 37.6 ± 2.1 |
| G ^D MC#3-39-900 | 39 ± 4 | 1.56 (0.23) | 692 (506) | 116 | 85:15 | 27.2 ± 2.4 |
| G ^D MC#3-39-1600 | 39 ± 5 | 1.15 (0.03) | 202 (74) | 124 | 90:10 | 36.9 ± 4.0 |
| G ^D MC#4-12-900 | 11 ± 2 | 0.37 (0.2) | 529 (437) | 71* | 80:20 | 27.1 ± 1.0 |
| G ^D MC#4-12-1600 | 12 ± 3 | 0.24 (0.06) | 172 (93) | 66** | 86:14 | 34.2 ± 2.2 |
| G ^A MC#5-900 | 35 ± 5 | 2.01 (0.15) | 588 (332) | 48 | 90:10 | 29.6 ± 3.1 |
| G ^A MC#5-1600 | 31 ± 9 | 1.41 (0.05) | 348 (120) | 49 | 93:7 | 36.7 ± 5.7 |

^a determined by BJH-model applied to nitrogen sorption isotherms; ^b based on amount adsorbed at relative pressure of 0.99; ^c determined using the t-plot method; ^d determined by SAXS; ^e determined by XPS; ^f determined by fitting of Raman spectra; * from G^DMC-12-600; ** from G^DMC-12-1200.

area only contributed 27–30% to the total surface area of G^DMC#1-15-1600, G^DMC#2-20-1600 and G^DMC#3-39-1600, while micropores still contributed 54% to the total surface area for G^DMC#4-12-1600, indicating a relation between the carbon wall thickness and microporosity. Nitrogen sorption also confirmed the high porosity for the ISO#1-3 derived materials, supporting the results from SEM analysis. Assuming a carbon density of 2 g cm⁻³, a porosity of 62% was calculated from the pore volumes of around 0.8 cm³ g⁻¹ for G^DMC#1-15-1600 and G^DMC#2-20-1600. With a pore volume of 1.2 cm³ g⁻¹, G^DMC#3-39-1600 exhibited a high porosity of 71%, even after heat-treatment at 1600 °C. By comparison, G^DMC#4-12-1600 displayed a significantly lower porosity of 32 vol% as a result of the high content of carbon precursor in the hybrid, which was necessary to achieve the double gyroid morphology from the low PEO content in ISO#4. This demonstrates the tunability of the porosity of the carbon materials by changing the PEO content of the starting polymer. The tunability of the pores was further evidenced by comparing the contributions of micro- and mesopores to the pore volume of the G^DMC

materials pyrolyzed at 1600 °C. For materials derived from ISO#1–3, the microporosity decreased drastically due to extensive condensation, and its contribution to the pore volume was minimal (Table 2.2). In most porous carbon materials with high porosity, pores of less than 5 nm diameter make up the majority of the pore volume.¹⁵ In contrast, the large mesopores contributed over 96% of the pore volume in the G^DMC#1-15-1600, G^DMC#2-20-1600, and G^DMC#3-39-1600 materials. The tremendously high temperature stability of the ordered structure of the carbon materials made this high mesoporosity with low microporosity possible. For G^DMC#4-12-1600, the micropores still contributed 25 % to the total pore volume, showing again that the ratio of micro- and mesoporosity seems to be dependent on the pore wall thickness at these high pyrolysis temperatures.

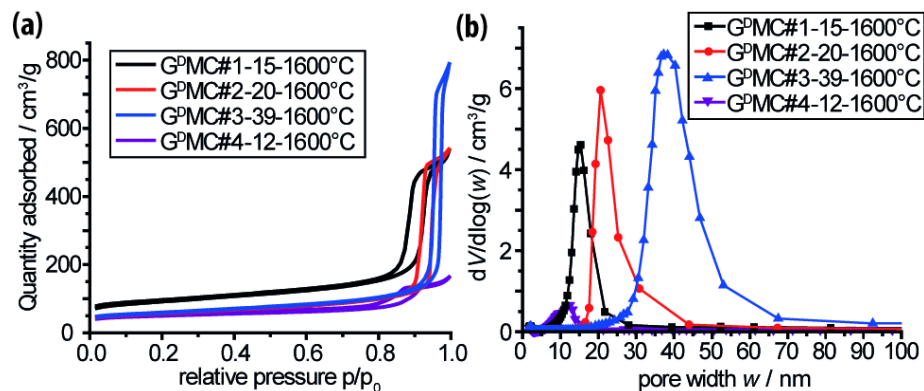


Figure 2.3. (a) Nitrogen sorption isotherms and (b) pore size distributions of GDMC#1-15-1600, GDMC#2-20-1600, GDMC#3-39-1600, and GDMC#4-12-1600. The pore size distributions were calculated using the BJH model for cylindrical pores.

Analysis of the nitrogen adsorption isotherm using the Barrett-Joyner-Halenda (BJH) method resulted in narrow pore size distributions centered at 12 nm, 16 nm, 21 nm and 39 nm for G^DMC#4-12-1600, G^DMC#1-15-1600, G^DMC#2-20-1600 and G^DMC#3-39-1600, respectively (Figure 2.3b), consistent with the SEM analysis. To the best of our knowledge, the ultra-large pore size of 39 nm is the largest reported to date for ordered soft-templated carbon materials. It exceeds the largest pore size previously reported, *fcc* packed spherical pores, by 5% and the largest reported gyroidal mesoporous carbon by more than 300%. This demonstrates the versatile tunability over a wide range of structural and porosity characteristics by rational design of the structure directing block copolymer.

Alternating gyroidal mesoporous carbon (G^AMC): Another cubic bicontinuous morphology that is thermodynamically stable for triblock terpolymers is the so-called alternating gyroid (Q²¹⁴, I4₁32).³⁴ In this morphology, the PI and the PEO end blocks each form a single gyroid network in a PS matrix. The two chemically distinct networks are enantiomeric and interpenetrating (Scheme 2.1). For the fabrication of G^AMC#5, we synthesized the terpolymer ISO#5, with a very low PEO volume fraction of 4.9 vol% and a low polydispersity of 1.04 (Table 2.1). Following the protocol described above for the successful and well controlled synthesis of double gyroidal organic-organic hybrids, however, we were not able to obtain ordered hybrids using ISO#5 and phenol-formaldehyde resols (Figure S2.3). In order to increase the interaction parameter between the hydrophilic and hydrophobic phases in our mixed polymer/resols system, we introduced more phenolic hydroxy groups by using resorcinol-formaldehyde resols as the carbon precursor. This change in precursor functionality lead to the formation of organic-organic hybrids with well ordered network morphology following our protocol, which was subsequently converted into an OMC network by pyrolysis.

The SAXS pattern of the organic-organic hybrid from ISO#5 and resorcinol-formaldehyde resols showed multiple peaks, some of which were overlapping (black trace in Figure 2.4a). The first sharp peak at a q -value of 0.13 \AA^{-1} was followed by a peak at 0.2 \AA^{-1} with a shoulder on the higher q -side and a third peak at 0.35 \AA^{-1} with a shoulder on either side. The peaks and their shoulders matched the q/q^* -ratios of $\sqrt{3}$, $\sqrt{4}$, $\sqrt{6}$, $\sqrt{7}$ and $\sqrt{8}$, with q^* being the first order peak, consistent with the allowed peaks of the Q²¹⁴ space group. Note that an expected peak at a ratio of $\sqrt{5}$ to the first order peak did not appear. However, the existence of the peak with a q/q^* -ratio of $\sqrt{6}$, corresponding to the (222) plane, and the absence of a peak with a $\sqrt{2}$ ratio suggested the formation of the alternating gyroid structure in the organic-organic hybrid. The first peak at 0.13 \AA^{-1} corresponds to the (110) plane of the alternating gyroid morphology with a lattice constant of 69 nm.

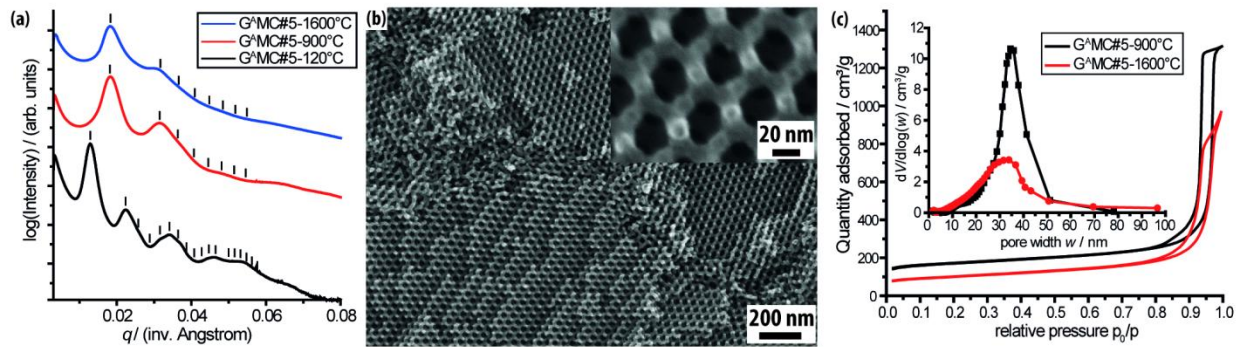


Figure 2.4. (a) Small angle X-ray scattering (SAXS) patterns, (b) scanning electron microscopy (SEM) image (inset: higher magnification of the (111) projection) after pyrolysis at 1600 °C and (c) nitrogen sorption isotherms with BJH pore size distributions (inset) of alternating gyroidal mesoporous carbons ($G^A MC\#5$).

Upon heat treatment under inert atmosphere, the resorcinol-formaldehyde resols – ISO hybrid was converted into a periodically ordered mesoporous carbon network. The SAXS patterns after pyrolysis shifted to higher q -values and exhibited a lower resolution, in contrast to the double gyroidal mesoporous carbons. This was probably due to the fragility of the single gyroid network that caused non-uniform shrinkage and loss of symmetry. However, a first order peak and a higher order peak with a shoulder on the high q -side were clearly distinguishable. The q/q^* -ratio of the peaks and the shoulder were 1, $\sqrt{3}$ and $\sqrt{4}$, consistent with the (110), (211) and (220) plane reflections of the Q^{214} space group with $I4_132$ symmetry. However, the gyroidal morphology might not be completely retained after pyrolysis and formation of a structure only closely related to the single gyroidal morphology is also possible.³⁵ The resolution of the pattern was independent of the pyrolysis temperature. The decrease in unit-cell size of the material before and after heat treatment corresponded to a 30% shrinkage of the periodic single network, very similar to the shrinkage seen in the case of the double gyroidal morphology. To the best of our knowledge, this is the first report of a single gyroidal mesoporous carbon network.

Scanning electron microscopy of the pyrolyzed $G^A MC\#5$ supported the formation of a well ordered and periodic, porous single gyroidal network. The highly ordered network that was observed exhibited thin struts that were connected by triple nodes (Figure 2.4b). At higher magnification, a honeycomb like structure with two struts per hexagon coming out of the image plane that matches the (111) projection of a

single gyroid network was seen (inset in Figure 2.4b). From analysis of the SEM images, the diameter of the struts was determined to approximately 15 nm and the pore diameter along the (111) projection was determined to approximately 26 nm. Similar to the SAXS patterns, the order that was seen in the SEM images did not change when the pyrolysis temperature was raised from 900 °C to 1600 °C as evidenced by a similar grain size of the mesostructure on the order of a few microns for materials heated to these temperatures. Considering the low carbon precursor content in the organic-organic hybrid, it is astonishing that the ordered morphology does not collapse upon decomposition of the structure directing triblock terpolymer and excessive condensation of the resin during carbonization at temperatures as high as 1600 °C. The SEM images suggest a very high porosity of the single gyroidal carbon network, which is expected from the low resorcinol-formaldehyde resols to ISO ratio, with good structure retention.

Nitrogen sorption confirmed the high porosity of the single gyroidal carbon network (Figure 2.4c). For both heat treatment temperatures, the isotherms showed typical type-IV curves with H₁-type hysteresis and sharp capillary condensation above relative pressures of 0.95. The amount of nitrogen adsorbed at low relative pressure was almost twice as high for the sample treated at 900 °C compared to the one heated to 1600 °C, indicating a much higher specific surface area for the lower temperature treated carbon network. BET analysis resulted in specific surface areas of 588 m² g⁻¹ and 348 m² g⁻¹ for G^AMC#5-900 and G^AMC#5-1600, respectively. The micropore surface area contributed more than 50% to the total surface area for samples heated at 900 °C, and, very similar to the double gyroidal carbons, it decreased to less than 35% after pyrolysis at 1600 °C (Table 2.2). Pore volumes of 2.01 cm³ g⁻¹ and 1.41 cm³ g⁻¹ for samples treated at 900 °C and 1600 °C, respectively, were observed by nitrogen sorption. These values exceeded the highest obtained pore volume for the double gyroidal morphology and corresponded to porosities of 80% and 74%, respectively. As seen for the double gyroidal morphology, this high pore volume was almost exclusively constituted by the mesopores after carbonization at 1600 °C. The micropore volume decreased by a factor of three upon pyrolysis at 1600 °C. The pore size distribution, calculated using the BJH model for cylindrical pores, showed a broad peak centered at 35 nm, with higher peak area for the sample heat treated at 900 °C, in agreement with the higher pore

volume (Figure 2.4c, inset). The pores of the single gyroidal carbon network do not exhibit cylindrical shape, as assumed in the BJH model, which can explain the large discrepancy between the pore size obtained from SEM image analysis and the BJH result.

Characterization of the carbon microstructure: In order to investigate their composition, atomic structure, and degree of graphitization, the ordered mesoporous carbon materials reported here were characterized by X-ray photoelectron spectroscopy (XPS), high resolution XPS (HR-XPS), Raman spectroscopy, high resolution TEM (HR-TEM), wide angle X-ray diffraction (WAXD) and electron energy loss spectroscopy (EELS).

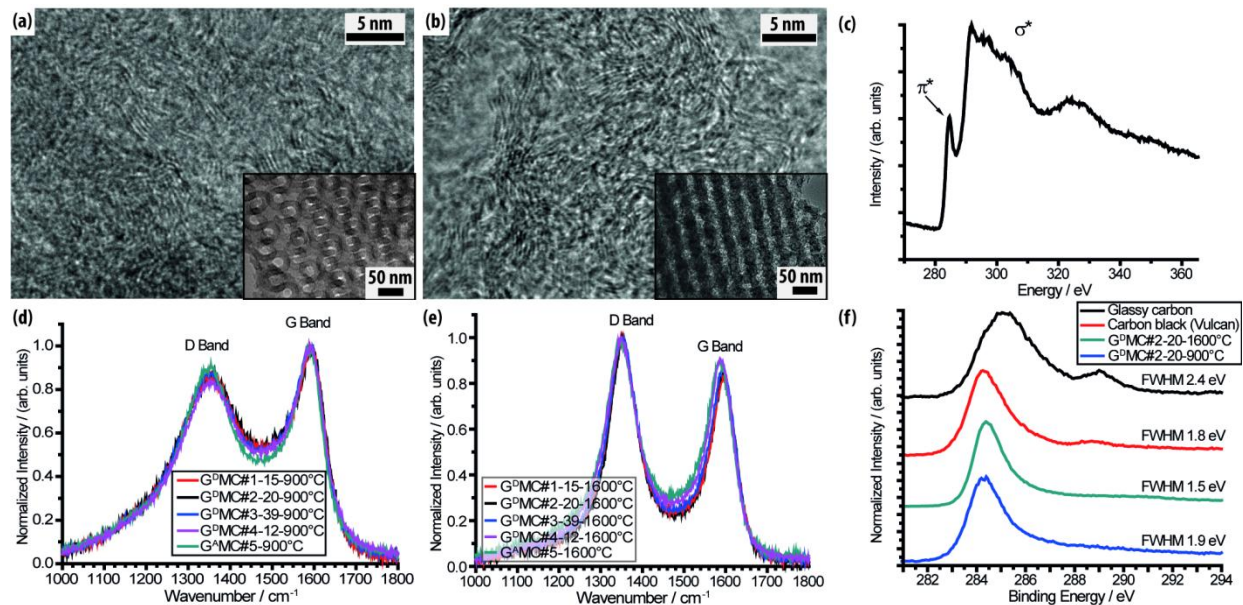


Figure 2.5. High-resolution transmission electron microscopy (HR-TEM) images of (a) G^DMC#2-20-1600, and (b) G^AMC#5-1600. Insets at a lower magnification of the same samples show the mesostructure. (c) Electron energy loss spectrum (EELS) of the carbon K-edge of G^DMC#2-20-1600. The spectrum is an average of six area spectra (10x10 nm²) taken at different spots of the sample. Raman spectra of powders of double gyroidal mesoporous carbons pyrolyzed at (d) 900 °C and (e) 1600 °C showing the evolution of the D- and G-bands. (f) High resolution – X-ray photoelectron spectroscopy (HR-XPS) data of the carbon K-edge of G^DMC#2-20-900, G^DMC#2-20-1600, and for comparison glassy carbon as well as carbon black, showing the decrease of the peak width at higher carbonization temperatures.

XPS can be used to investigate the elemental composition of the top 1–10 nm of a material. Since our materials showed wall thicknesses of less than 20 nm, we assume that the resulting elemental composition

is representative for our bulk material. The carbon materials heated to 900 °C showed oxygen contents of 10–20% which decreased to 7–16% for materials pyrolyzed at 1600 °C (Table 2.2). The oxygen content was most-likely due to hydroxyl groups on the carbon surface. In comparison, from XPS spectra of glassy carbon and carbon black (Vulcan X72) we calculated oxygen contents of 19% and 5%, respectively. The HR-XPS spectra of the carbon K-edge of G^DMC#2-20 carbonized at 900 °C and 1600 °C are shown in Figure 2.5f together with other carbon materials for comparison. HR-XPS showed one narrow peak centered at 284.4 eV, indicating that only one type of carbon was predominantly present. The full width at half maximum (FWHM) of this G^DMC peak decreased with increasing carbonization temperature and was narrower than carbon black when pyrolyzed at 1600 °C. Furthermore, the carbon K-edge in EELS showed the appearance of a pre-peak, that is due to the π^* -band, only present in sp²-hybridized carbon materials (Figure 2.5c). We concluded from the HR-XPS and EELS spectra that after carbonization at 1600 °C, the carbon atoms in the structured mesoporous materials were almost entirely sp²-hybridized.

In order to determine the degree of graphitization, Raman spectroscopy as well as WAXD were applied to elucidate the in-plane size of the graphitic clusters and the number of stacked sheets, respectively. In Raman spectroscopy of disordered carbon materials, two bands, called the D- and the G-band, are typically observed at approximately 1350 cm⁻¹ and 1590 cm⁻¹, respectively. The G-band arises from the in-plane vibration of C=C double bonds, while the D-band is caused by a breathing mode of isolated benzene rings.³⁶ The Raman spectra of the G^DMC materials heated to 900°C and 1600°C are displayed in Figure 2.5d and 2.5e, respectively. For the two temperatures, the D- and the G-band were clearly visible at 1352 cm⁻¹ and 1592 cm⁻¹ (900°C) and 1352 cm⁻¹ and 1595 cm⁻¹ (1600°C), indicating the presence of disordered carbon. For a given pyrolysis temperature, the different G^DMC materials displayed identical Raman spectra irrespective of their pore size. Higher pyrolysis temperatures lead to narrower bands and increased the ratio of the integrated intensities of the G-band to the D-band suggesting a higher degree of graphitization for higher pyrolysis temperatures. Tuinstra and Koenig reported an empirical formula for the determination of the in-plane size of graphitic clusters based on the ratio of the G-band to the D-band (see SI).^{36,37} Applying this formula, the in-plane size of the graphitic clusters was estimated to

approximately 2.7 nm for the G^DMC-900 materials, and to approximately 3.7 nm for the G^DMC-1600 materials (Table 2.2), consistent with values reported in the literature on the pyrolysis of phenolic resins.³⁸ In WAXD measurements of graphitic materials, the peak at $2\theta = 23\text{-}27^\circ$ corresponds to the (200) plane of graphite. The position of the peak depends on the spacing between the graphene sheets ($2\theta = 26.6^\circ$ for graphite corresponding to 0.335 nm sheet spacing) and its FWHM gives information about the number of stacked graphene sheets. Measurements of the G^DMC materials yielded diffractograms with poorly defined peaks at $2\theta = 25^\circ$ (Figure S2.4). This indicated a small number of stacked graphene sheets, but made an analysis of the FWHM of the peak unreliable.

HR-TEM images of G^DMC#2-20-1600 and G^AMC-1600 were consistent with the calculations from the Raman spectra (Figure 2.5a and 2.5b). Areas with four to eight parallel graphitic sheets of 3–5 nm length were observed. The orientation of the graphitic sheets in the different clusters was random and in no relationship to the features of the mesostructure, *e.g.* parallel or vertical to the pore wall. Additionally, curvature is evident in most of the graphitic sheets. The small cluster size, random orientation and varying curvature give rise to poor crystallographic long range order. The lack of long range order of more than a few nanometers is consistent with the poorly defined peaks observed in WAXD. Our analysis suggests that the microstructure of the gyroidal mesoporous carbons bears a strong resemblance to the microstructure of glassy carbon. The electrical conductivity of powdered gyroidal carbon materials was measured using a home-built four-point probe apparatus with uni-axial applied pressure of 250 psi as described in detail before.³⁹ The conductivities of G^DMC#2-20-900 and G^DMC#2-20-1600 were 0.1 S cm⁻¹ and 2.1 S cm⁻¹, respectively, which makes our high temperature treated gyroidal mesoporous carbon comparable to Carbon Black (Vulcan XC72) with a measured conductivity of 4.2 S cm⁻¹ under the same conditions.

In order to elucidate the influence of the morphology on the graphitic cluster size, we investigated carbon materials from hybrids with hexagonally packed cylindrical morphology (see Appendix A). Hybrids using ISO#1 and ISO#2 formed an inverse hexagonally packed cylindrical morphology at resols:ISO loadings up to 1.2:1 (Figure S2.5a). The materials showed similar Raman spectra as the

gyroidal mesoporous carbons (Figure S2.5c). HR-TEM images also suggested randomly oriented graphitic clusters with the same apparent size and curvature as in the gyroidal materials (Figure S2.5d). This result suggests that for the present terpolymer derived carbons, there is no relationship between the carbon micro- and mesostructure. Formation of a well defined hexagonally oriented cylindrical morphology at higher resols loadings demonstrated further structural tunability of mesoporous carbons *via* our synthesis procedure.

Monolithic gyroidal mesoporous carbon: Following our synthesis strategy, we were able to synthesize monolithic gyroidal mesoporous carbons (mG^DMC) with tailored macroscopic dimensions. As-cast, annealed organic-organic hybrid films were flexible and therefore could be cut or punched into the desired shape (Figure 2.6a). After carbonization at temperatures up to 1600 °C, the monoliths retained their macroscopic appearance (Figure 2.6a). The large mesostructural shrinkage of 30% during heat treatment was translated into a macroscopic shrinkage of the monoliths (*e.g.* a hybrid disc of 10 mm diameter yielded a gyroidal carbon monolith of 7 mm diameter, Figure 2.6a). Considering this large shrinkage, it was surprising that the monoliths kept their structural integrity without cracking or pulverizing. Furthermore, by altering the amount of material per casting area, we were able to tailor the monolith thickness from over 200 μm to less than 50 μm, a thickness ideally suited for electrode applications (Figure 2.6b). The remarkable macrostructure preservation for different monolith sizes demonstrated the high versatility of our process. We attribute the macroscopic stability of the materials at high temperatures to the wall thickness of more than 10 nm as well as the bicontinuous mesostructure that allowed isotropic strain release during the shrinkage and assured sufficient release of the decomposition gases without building up of pressure inside the material that would cause cracking of the monolith. To the best of our knowledge this is the first report of silica-free, soft-templated ordered mesoporous carbon monoliths without macropores. Moreover, we developed a procedure to fabricate monoliths with structured surfaces that show narrow pore size distributions (Figure 2.6c and d).

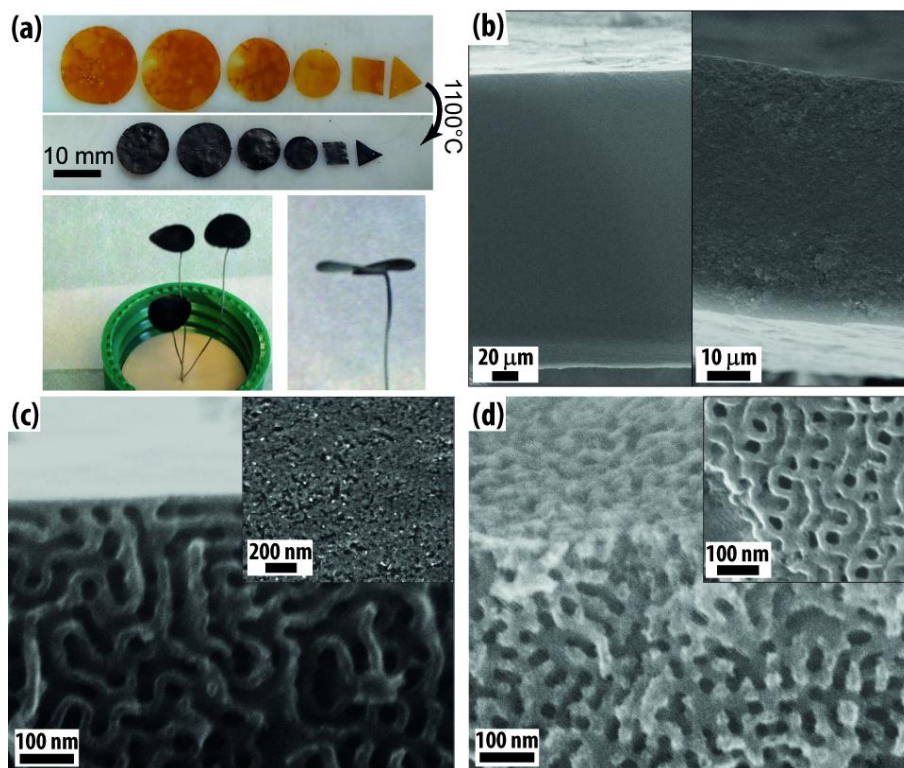


Figure 2.6. (a) Photographs of G^D MC#3-39-1200 monoliths from the top (bottom left) and conductively connected to silver wires (top left and right). Cross sectional SEM images of G^D MC#3-39-1200 monoliths of (b, left) 200 μm and (b, right) 50 μm thickness; higher magnification images at the edge of the surface (c) unexposed and (d) exposed to prior plasma treatment of the organic-organic hybrid. The insets in (c) and (d) show SEM images of the top surfaces only.

A common problem with continuous films of mesostructured materials obtained by soft templating is the orientation of the pores and an unstructured or closed surface layer on the top and bottom of the film (see Figure 2.6c, inset and Figure S2.1d) due to lamellar capping layers.^{14,30} This is caused by the different surface energies of the various block copolymer domains during the casting process. Due to the bicontinuous nature of the cubic, gyroidal morphology, the orientation of the structure with respect to the surfaces is irrelevant. By oxygen/argon plasma etching of the organic-organic hybrid monoliths, the lamellar capping layers could be removed and the gyroidal bulk structure became directly accessible from the surface (see Figure 2.6d and inset). After carbonization at temperatures as high as 1600 $^{\circ}\text{C}$, the surface showed gyroidal features, assuring a narrow pore size distribution also at the surface. The pores on the surface are slightly smaller according to SEM image analysis compared to the interior gyroidal porosity, however, most likely due to condensation of the polymeric materials on the surface during plasma

treatment. Additionally, this simple process allows for selective exposure of only a fraction of the surface to the plasma, hence leading to a tailored opening of surface sites. For example, we covered one surface of a hybrid film during plasma treatment, which led to a carbon monolith with one closed surface and one ordered, porous surface (similar to Figure 2.6c and d, respectively). Furthermore, this opened up the possibility of conductively connecting the monolith with silver or carbon paste on the closed side, making the monolith accessible for further electrochemical treatments, without the risk of the required binder to infiltrate the pores and, as a result, distort the measurements.

Conclusion

In this report, we have demonstrated the metal- and halogen-free synthesis of highly ordered double gyroidal mesoporous carbons, with tailored pore sizes of up to 39 nm, the largest reported pore size for soft-templated OMCs to date. By modification of the carbon precursor, to the best of our knowledge for the first time we synthesized single gyroidal carbon networks from organic-organic hybrids with alternating gyroid morphology. Through the rational design of the triblock terpolymers, we show high tunability of the porosity between 32–80 vol% combined with structural stability up to 1600 °C, unprecedented for soft-templated ordered mesoporous materials, ensuring a high degree of sp^2 -hybridization and low microporosity with a glassy carbon-like microstructure. Finally, we demonstrated the first silica-free soft-templating process to fabricate monolithic gyroidal mesoporous carbons with tailored macroscopic shape, and accessible surface pores through plasma treatment of the organic-organic hybrids before carbonization.

Since all the microstructural characteristics of the four reported double gyroidal mesoporous carbons are very similar to each other, this system is ideal for studies of the pore size dependence of the performance of such mesoporous carbon electrodes in energy technology or catalysis. Furthermore, the large and uniform pore size together with pore interconnectivity and the ability of making tailored monolithic materials thereof open up new possibilities for the fabrication of functional multi-component composites on the nanoscale, as illustrated on the right of Scheme 2.1.

Methods

Synthesis: Five poly(isoprene)-*block*-poly(styrene)-*block*-poly(ethylene oxide) (ISO) terpolymers were synthesized *via* sequential anionic polymerization as described before.⁴⁰ Results on molar mass, composition and polydispersity index (PDI) are summarized in Table 2.1. Polymer molar masses vary from 27 kg mol⁻¹ up to 108 kg mol⁻¹. Polydispersity indices were all below 1.1, demonstrating high control over the terpolymer synthesis.

Oligomeric phenol-formaldehyde resols with a molar mass of less than 500 g mol⁻¹ were synthesized using the well-known polymerization of phenol and formaldehyde under basic conditions and worked up in a modified way compared to what has been previously described.¹⁵ In a typical synthesis, 9.411 g of phenol (0.1 mol, redistilled, 99+%, Sigma-Aldrich) was melted in a three neck flask equipped with a reflux condenser in a water bath at 45 °C. A 20 wt% sodium hydroxide solution was prepared by dissolution of 0.4 g sodium hydroxide (0.01 mol, pellets, Mallinckrodt) in 1.6 g deionized water. The sodium hydroxide solution was added dropwise to the melted phenol. The sodium phenoxide solution was stirred for 10 minutes and 14.89 mL formalin solution (37 wt% in water, ACS Reagent, Sigma-Aldrich), containing 0.2 mol formaldehyde, was carefully added dropwise over 10 mins. The slightly orange-colored solution was heated to 75 °C and held at this temperature for 1 hour. The orange solution was allowed to cool to room temperature and subsequently neutralized with *para*-toluene sulfonic acid (\geq 98.5%, ACS reagent, Sigma-Aldrich). The orange/yellow solution was freeze-dried overnight on a vacuum line and the orange resols were dissolved in a mixture of tetrahydrofuran (Anhydrous, inhibitor free, \geq 99.9%, Sigma-Aldrich) and chloroform (anhydrous, \geq 99%, Sigma-Aldrich) (1:1 wt). The resulting cloudy solution was filtered through a PTFE syringe filter (0.2-0.4 μ m) to remove the precipitated sodium *para*-toluene sulfonate, dried again overnight on a vacuum line and dissolved in tetrahydrofuran:chloroform (1:1 wt) as a 25 wt% solution. Oligomeric resorcinol-formaldehyde resols were synthesized in a similar way. A highly concentrated resorcinol solution in water was used (50 wt%) and mixed with a 20 wt% sodium hydroxide solution and formalin solution. The molar ratio of resorcinol:NaOH:formaldehyde was 1:0.1:1. The mixture was stirred for 10 mins at room temperature and

promptly neutralized with *para*-toluene sulfonic acid. The red solution was freeze-dried overnight on a vacuum line and the solid resorcinol-formaldehyde resols were dissolved in tetrahydrofuran. The resulting cloudy solution was filtered through a PTFE syringe filter (0.2-0.4 μm) to remove the precipitated sodium *para*-toluene sulfonate and higher molar mass resins, dried again overnight on a vacuum line and dissolved in tetrahydrofuran as a 20 wt% solution. The molar mass of the synthesized resorcinol-formaldehyde resols was larger than the phenol based resols as indicated by a shorter elution time in gel permeation chromatography. However, the elution time was slightly longer than of a poly(styrene) standard with a molar mass of 1010 g mol^{-1} , indicating a smaller hydrodynamic radius than the poly(styrene) standard.

Organic-organic hybrids were synthesized through evaporation induced self-assembly (EISA). The prepared resols solution was added to solutions of the ISO terpolymers in a 1:1 weight mixture of tetrahydrofuran and chloroform yielding a 4-10 wt% solution and stirred for 24 hours in the case of phenol-formaldehyde resols and 1 hour in the case of resorcinol-formaldehyde resols. The ratios of resols to ISO to obtain the desired gyroidal morphology are summarized in Table 2.1. The solutions were cast in a Teflon dish at $50 \text{ }^\circ\text{C}$ covered with a glass dome to ensure a solvent saturated atmosphere throughout the drying process and subsequently cured at $110\text{-}130 \text{ }^\circ\text{C}$ in a convection oven for 24 hours. For carbonization, the cured hybrids were heated at $1 \text{ }^\circ\text{C min}^{-1}$ to $600 \text{ }^\circ\text{C}$ and pyrolyzed under inert atmosphere (nitrogen or argon) at $600 \text{ }^\circ\text{C}$ for 3 hours and then brought to the final temperature (see text) at a rate of $5 \text{ }^\circ\text{C min}^{-1}$.

Monolithic double gyroidal carbons ($\text{mG}^{\text{D}}\text{MC}$) were fabricated by cutting the cured organic-organic hybrid monoliths into the desired shape and subsequent heat treatment as described above. For carbon monoliths with open and structured surfaces, the hybrid monoliths were exposed to oxygen/argon plasma for 30-60 mins before carbonization.

Characterization: The composition of the triblock terpolymers was calculated using ^1H nuclear magnetic resonance ($^1\text{H NMR}$) spectroscopy. The polymers were dissolved in deuterated chloroform

(Chloroform-d, 99.8 atom% D, Aldrich) with a concentration of 15-20 mg mL⁻¹. ¹H NMR spectra were recorded on a Varian Mercury spectrometer at 300 MHz.

Gel permeation chromatography (GPC) was used to determine the molar mass of the triblock terpolymers and the oligomeric resols. Samples were prepared in tetrahydrofuran (THF) with a concentration of 1.5 mg mL⁻¹. GPC measurements were performed in THF at 23 °C (1 mL min⁻¹) on a Waters Ambient-Temperature GPC system equipped with a Waters 2410 differential refractive index (RI) detector.

The morphology of the organic-organic composites and porous carbon materials were determined using a combination of small angle X-ray scattering (SAXS), brightfield transmission electron microscopy (TEM) and scanning electron microscopy (SEM).

TEM samples of composite films were prepared by cryo ultramicrotoming to a thickness of 50-70 nm using a Leica Ultracut UCT Cryo-Ultramicrotome equipped with a diamond knife at -60 °C. The microtomed sections were floated on a water/DMSO (40:60 vol) mixture and subsequently placed on copper grids. Contrast was obtained by staining the samples with osmium tetroxide vapor (60 mins). Heat-treated porous materials were crushed in a ball mill, dispersed in ethanol and dropped onto carbon-coated copper grids. Bright field transmission electron microscopy (TEM) was performed on a FEI Tecnai T-12 TWIN TEM operating at an accelerating voltage of 120 kV equipped with a high resolution, thermoelectrically-cooled Gatan Orius® dual-scan CCD camera. HR-TEM images were obtained on a FEI-F20-TEM-STEM operating at an accelerating voltage of 200 kV. Scanning electron microscopy (SEM) of carbonized samples was carried out on a Zeiss LEO 1550 FE-SEM operating at an accelerating voltage of 10 kV. Due to the conductivity of the samples, no additional coating of the specimen was necessary.

For SAXS measurements, small squares of the cured composites and pyrolyzed films (ca. 2x2 mm²) were cut and placed in the hole of a metal washer that was covered on one side with Kapton tape. SAXS measurements were performed at the Cornell High Energy Synchrotron Source (CHESS). The sample to

detector distance was 2.6 m and the X-ray wavelength was 1.2015 Å. The scattering vector q is defined as $q = (4 \cdot \pi / \lambda) \cdot \sin\theta$, where θ is half of the scattering angle.

X-ray diffraction patterns were obtained on an Ultima IV multipurpose X-ray diffraction system from Rigaku using Cu K α radiation (40V, 44 mA, wavelength 1.5418 Å) in a 2θ range between 10° to 90° with a speed of 5° min⁻¹.

For Raman spectroscopy, a Renishaw InVia Confocal Raman microscope was used at room temperature in a backscattering geometry, equipped with a 488 nm diode laser as an excitation source focused on the sample with a 50x magnification.

Sorption isotherms were obtained on a Micromeritics ASAP 2020 surface area and porosity analyzer at -196 °C. The samples were degassed at 200 °C under vacuum for at least 10 hours prior to measurements. The specific surface areas were determined using the Brunauer-Emmett-Teller (BET) method. Pore size distributions were calculated using the Barrett-Joyner-Halenda (BJH) method.^{41,42}

Acknowledgements

This work was supported as part of the Energy Materials Center at Cornell (emc²), an Energy Frontier Research Center funded by the U.S. Department of Energy, Office of Science, Basic Energy Sciences under Award # DE-SC0001086. T.N.H. thanks the Swiss National Science Foundation (SNF) for a Postdoc fellowship. This work made use of the Cornell Center for Materials Research Shared Facilities which are supported through the NSF MRSEC program (DMR-1120296). This work was further based upon research conducted at the Cornell High Energy Synchrotron Source (CHESS) which is supported by the National Science Foundation and the National Institutes of Health/National Institute of General Medical Sciences under NSF award DMR-0936384. The authors also gratefully acknowledge Prof. D. Muller and B. Levin of Cornell University for helpful discussions and kind experiment assistant with the EELS measurements.

APPENDIX A

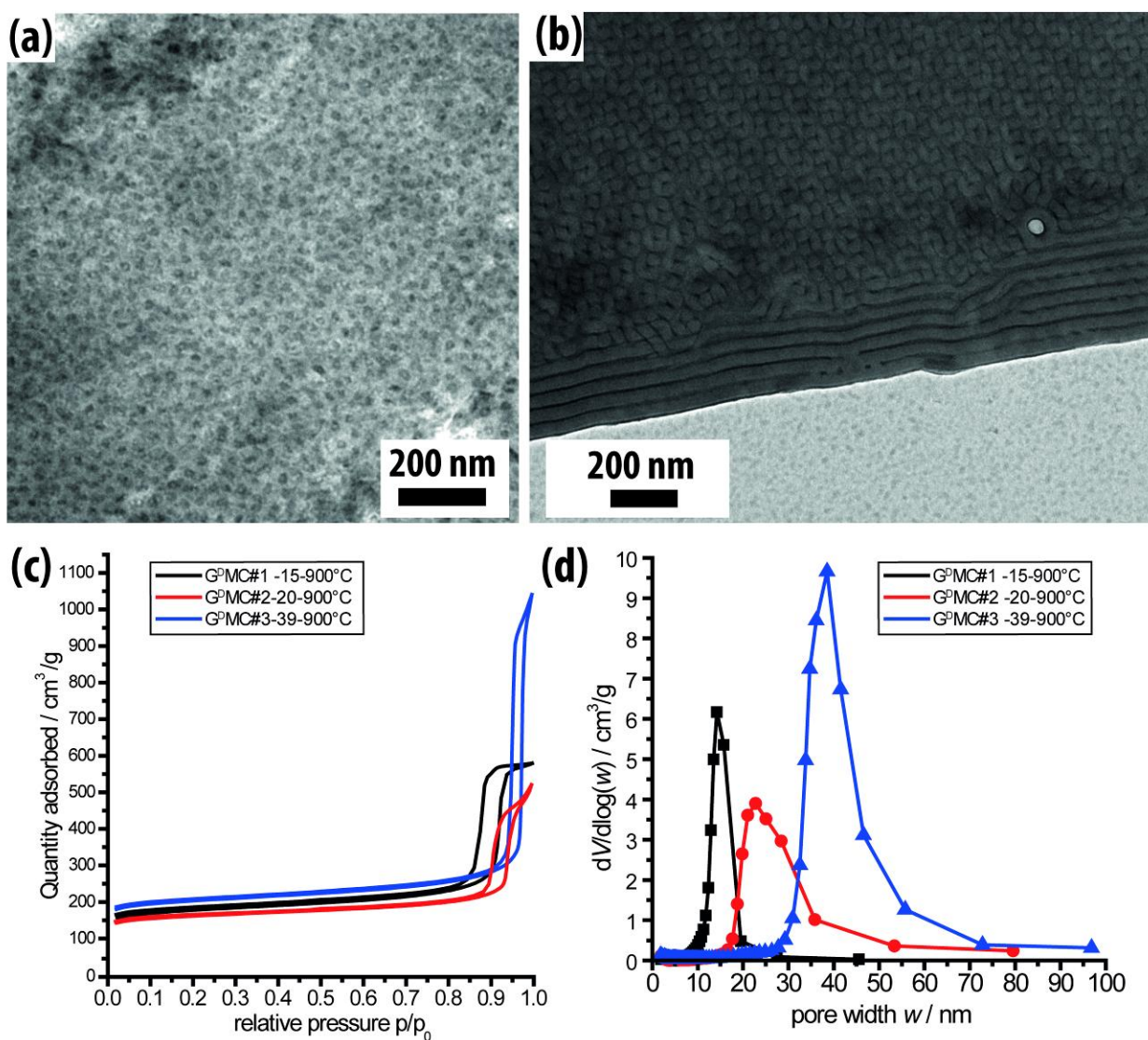


Figure S2.1. (a) Transmission electron microscopy image of ISO#2+resols following a synthetic procedure from the literature with only THF as the solvent and 1 hour stirring time only.¹⁵ (b) TEM image of the microtomed cross-section of a monolithic film mG^DMC#2-20-120 at the top surface. The lamellar sheets parallel to the surface are clearly distinguishable from the gyroidal bulk morphology. (c) Nitrogen sorption isotherms and (d) BJH pore size distributions of G^DMC#1-15-900, G^DMC#2-20-900, G^DMC#3-39-900.

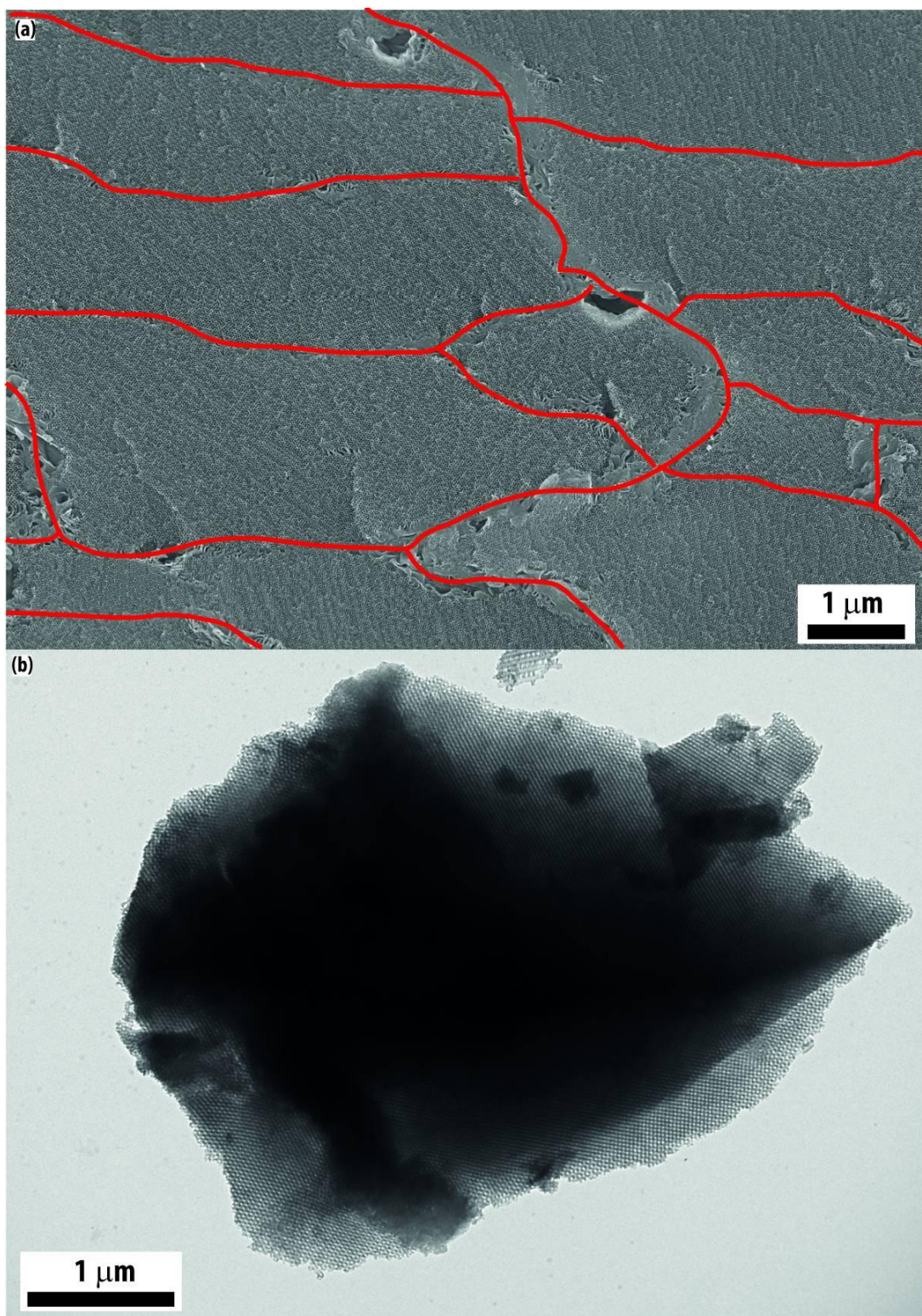


Figure S2.2. (a) Scanning electron microscopy image and (b) transmission electron microscopy image of G^D MC#1-15-1600 at low magnification showing a high degree of long range order and associated large gyroidal grain size of this carbon material.

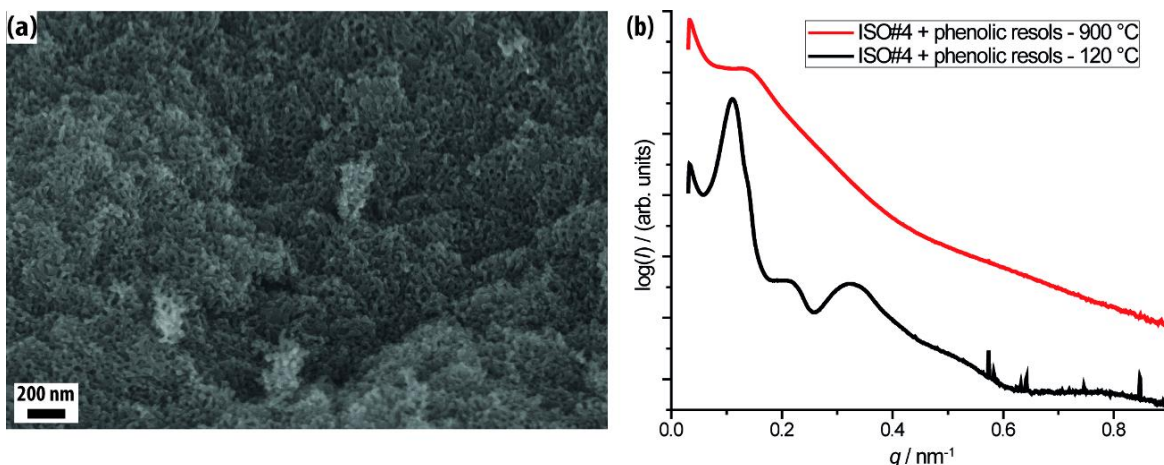


Figure S2.3. (a) Scanning electron microscopy image of a 900 °C pyrolyzed hybrid material of ISO#5 and phenol/formaldehyde resols suggesting the formation of a disordered network. (b) Small angle X-ray scattering patterns of the hybrid before pyrolysis (lower trace) and after pyrolysis (upper trace) revealing poor structure formation in the hybrid and loss of periodicity after heat treatment. The material was prepared the same way as the G^DMCs.

Raman Spectroscopy:

Raman spectra of the powdered carbons were measured at an excitation wavelength of 488 nm on a Renishaw InVia microRaman system equipped with a 50x objective with a numerical aperture of 0.45. Five spectra at different spots were measured for each sample.

The in plane graphitic cluster size, L_a , of the gyroidal mesoporous carbons was calculated using the empirical equation by Tuinstra and Koenig:^{36,37}

$$L_a = 43.9 \cdot \left(\frac{I_D}{I_G}\right)^{-1}$$

yielding the in plane graphitic cluster size, L_a , in Ångstrom. For this purpose, the spectra were fitted between 900 cm⁻¹ and 1900 cm⁻¹ using two peaks, a Lorentz line for the D band and a Breit-Wigner-Fano line for the G band. For the calculation of L_a , integrated intensities, I_D and I_G , of the peaks were employed. The reported values of L_a represent the mean value obtained from five spectra of the respective carbon with a confidence interval of 95%. Representative spectra with the corresponding peak fitting of gyroidal mesoporous carbons heated to 900 °C and 1600 °C are shown in Figure S2.4b.

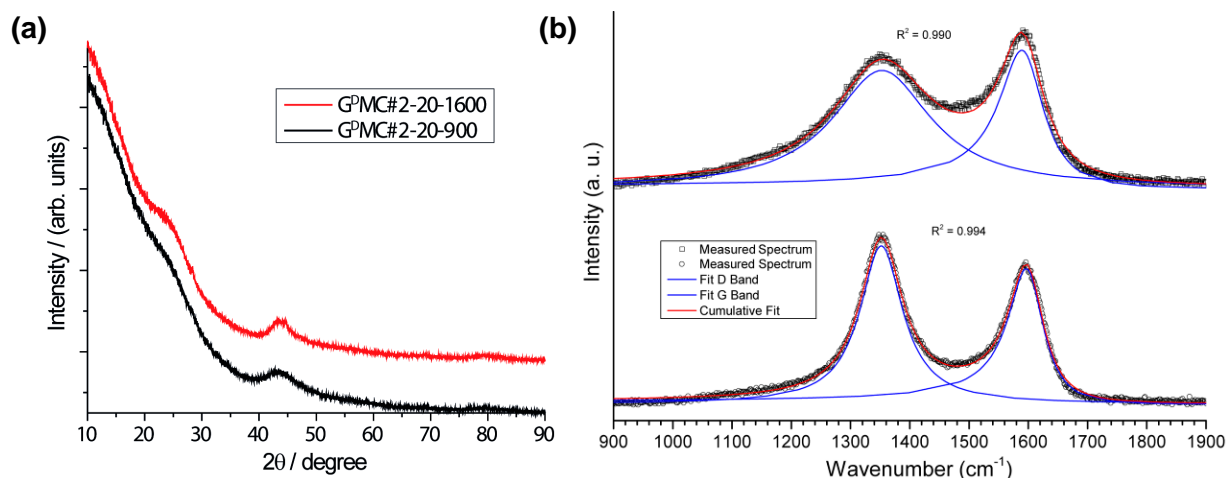


Figure S2.4. (a) Powder X-ray diffraction patterns of G^DMC#2-20-900 (lower trace) and G^DMC#2-20-1600 (upper trace) showing the evolution of the graphitic (200) reflex at 22-26° and the (100) and (101) reflexes at 42-46°. The broad peaks indicate the existence of small graphitic clusters in the material. (b) Representative Raman spectra of powdered gyroidal mesoporous carbons heated at 900 °C (top, open squares, derived from ISO#2) and 1600 °C (bottom, open circles, derived from ISO#1) with peaks from peak fitting for the D and the G bands.

Hexagonally oriented cylindrical carbon morphology

For resols loadings in ISO#1 and ISO#2 organic-organic hybrids above the double gyroid window, hybrid characterization results suggested a core-shell hexagonally oriented cylindrical morphology, designated as ISO#X-Hex-Y where X stands for the ISO used and Y represents the highest temperature at which the material was heat treated. In this morphology, the hydrophilic PEO-resols phase forms the matrix around hexagonally packed poly(styrene)-*block*-poly(isoprene) core-shell cylinders. After decomposition of the structure directing triblock terpolymer and carbonization of the resols, the cylinders constitute one dimensional pores. The well ordered structure can be seen in the SEM images in Figure S2.5a. Nitrogen sorption revealed BET surface areas of 145 m² g⁻¹ and 167 m² g⁻¹ and micropore surface areas of 77 m² g⁻¹ and 67 m² g⁻¹ for ISO#1-Hex-1600 and ISO#2-Hex-1600, respectively. The pore volumes shrank, compared to the double gyroidal carbon materials from the respective polymers, to 0.30 cm³ g⁻¹ and 0.46 cm³ g⁻¹ for ISO#1-Hex-1600 and ISO#2-Hex-1600, respectively, due to the higher resols to ISO ratio of 1.1:1 and 1.2:1. Microstructural analysis of the hexagonal carbon materials showed very similar results to the gyroidal carbon materials. The Raman spectrum for ISO#1-Hex-1600 is shown in Figure S2.5c and is similar to those of the G^DMCs. High resolution transmission electron microscopy

revealed graphitic clusters of 3–8 stacked graphitic sheets with up to 7 nm length that are randomly oriented and slightly bent (Figure S2.5d). This suggests that the mesostructure as well as the resols density in the hydrophilic PEO-resol phase does not influence the microstructure of the resulting carbon material.

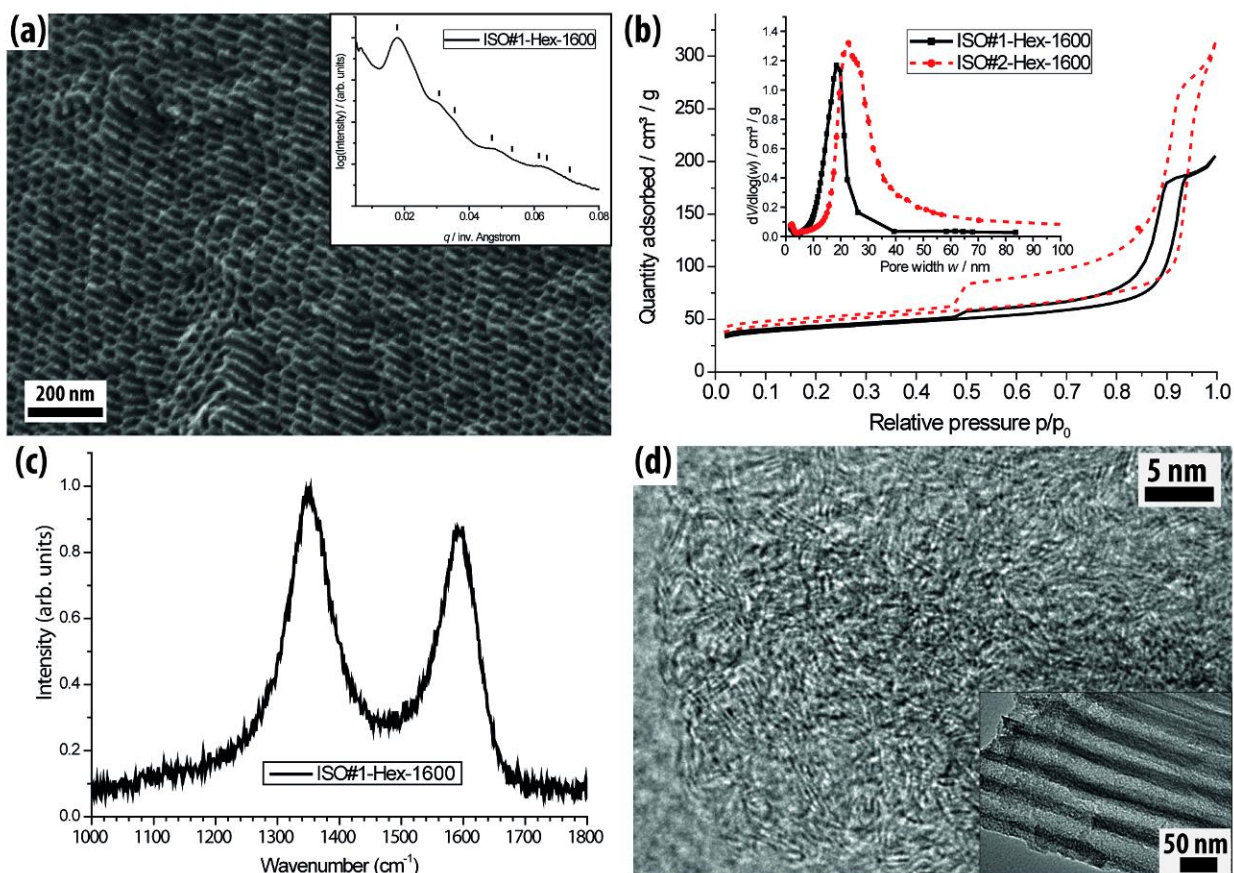


Figure S2.5. (a) Scanning electron microscopy image and small angle X-ray scattering (inset) pattern of ISO#1-Hex-1600 suggesting the formation of hexagonally oriented porous cylinders in a carbon matrix. The tick marks in the scattering pattern indicate the expected peak positions for hexagonal ordered cylinders. (b) Nitrogen sorption isotherms and BJH pore size distributions (inset) of ISO#1-Hex-1600 (solid line) and ISO#2-Hex-1600 (dashed line). (c) The Raman spectrum of ISO#1-Hex-1600 is similar to the spectra of the gyroidal mesoporous carbons pyrolyzed at 1600 °C. (d) High resolution – transmission electron microscopy image of ISO#2-Hex-1600 revealing the existence of small, bent graphitic clusters of a few stacked sheets with a length of 3–7 nm. Inset at a lower magnification of the same sample shows the mesostructure.

REFERENCES

- (1) Bansal, R. C.; Donnet, J. B.; Stoeckli, F. *Active Carbon*; Marcel Dekker: New York, 1988.
- (2) Yang, R. T. *Adsorbents - Fundamentals and Applications*; Wiley-Interscience: New York, 2003.
- (3) Gaffney, T. R. Porous Solids for Air Separation. *Curr. Opin. Solid State Mater. Sci.* **1996**, *1*, 69–75.
- (4) Ryoo, R.; Joo, S. H.; Jun, S. Synthesis of Highly Ordered Carbon Molecular Sieves via Template-Mediated Structural Transformation. *J. Phys. Chem. B* **1999**, *103*, 7743–7746.
- (5) Lee, J.; Yoon, S.; Hyeon, T.; Oh, M.; Bum, K. Synthesis of a New Mesoporous Carbon and Its Application to Electrochemical Double-Layer Capacitors. **1999**, 2177–2178.
- (6) Tian, B.; Che, S.; Liu, Z.; Liu, X.; Fan, W.; Tatsumi, T.; Terasaki, O.; Zhao, D. Novel Approaches to Synthesize Self-Supported Ultrathin Carbon Nanowire Arrays Templated by MCM-41. *Chem. Commun. (Camb)*. **2003**, 2726–2727.
- (7) Jun, S.; Joo, S. H.; Ryoo, R.; Kruk, M.; Jaroniec, M.; Liu, Z.; Ohsuna, T.; Terasaki, O. Synthesis of New, Nanoporous Carbon with Hexagonally Ordered Mesoporous Structure. *J. Am. Chem. Soc.* **2000**, *122*, 10712–10713.
- (8) Che, S.; Garcia-Bennett, A. E.; Liu, X.; Hodgkins, R. P.; Wright, P. a; Zhao, D.; Terasaki, O.; Tatsumi, T. Synthesis of Large-Pore Ia3d Mesoporous Silica and Its Tubelike Carbon Replica. *Angew. Chem. Int. Ed. Engl.* **2003**, *42*, 3930–3934.
- (9) Liu, X.; Tian, B.; Yu, C.; Gao, F.; Xie, S.; Tu, B.; Che, R.; Peng, L.-M.; Zhao, D. Room-Temperature Synthesis in Acidic Media of Large-Pore Three-Dimensional Bicontinuous Mesoporous Silica with Ia3d Symmetry. *Angew. Chem. Int. Ed. Engl.* **2002**, *41*, 3876–3878.
- (10) Kleitz, F.; Choi, S. H.; Ryoo, R. Cubic Ia3d Large Mesoporous Silica: Synthesis and Replication to Platinum Nanowires, Carbon Nanorods and Carbon Nanotubes. *Chem. Commun. (Camb)*. **2003**, 2136–2137.
- (11) Kim, T.-W.; Kleitz, F.; Paul, B.; Ryoo, R. MCM-48-like Large Mesoporous Silicas with Tailored Pore Structure: Facile Synthesis Domain in a Ternary Triblock Copolymer-Butanol-Water System. *J. Am. Chem. Soc.* **2005**, *127*, 7601–7610.

- (12) Yang, H.; Shi, Q.; Liu, X.; Xie, S.; Jiang, D.; Zhang, F.; Yu, C.; Tu, B.; Zhao, D. Synthesis of Ordered Mesoporous Carbon Monoliths with Bicontinuous Cubic Pore Structure of Ia3d Symmetry. *Chem. Commun. (Camb)*. **2002**, 2842–2843.
- (13) Liang, C.; Hong, K.; Guiochon, G. A.; Mays, J. W.; Dai, S. Synthesis of a Large-Scale Highly Ordered Porous Carbon Film by Self-Assembly of Block Copolymers. *Angew. Chem. Int. Ed. Engl.* **2004**, *43*, 5785–5789.
- (14) Tanaka, S.; Nishiyama, N.; Egashira, Y.; Ueyama, K. Synthesis of Ordered Mesoporous Carbons with Channel Structure from an Organic–Organic Nanocomposite. *Chem. Commun. (Camb)*. **2005**, 2125–2127.
- (15) Meng, Y.; Gu, D.; Zhang, F.; Shi, Y.; Cheng, L.; Feng, D.; Wu, Z.; Chen, Z.; Wan, Y.; Stein, A.; *et al.* A Family of Highly Ordered Mesoporous Polymer Resin and Carbon Structures from Organic–Organic Self-Assembly. *Chem. Mater.* **2006**, *18*, 4447–4464.
- (16) Liu, L.; Wang, F.-Y.; Shao, G.-S.; Ma, T.-Y.; Yuan, Z.-Y. Synthesis of Ultra-Large Mesoporous Carbons from Triblock Copolymers and Phloroglucinol/formaldehyde Polymer. *Carbon N. Y.* **2010**, *48*, 2660–2664.
- (17) Fulvio, P. F.; Mayes, R. T.; Wang, X.; Mahurin, S. M.; Bauer, J. C.; Presser, V.; McDonough, J.; Gogotsi, Y.; Dai, S. “Brick-and-Mortar” Self-Assembly Approach to Graphitic Mesoporous Carbon Nanocomposites. *Adv. Funct. Mater.* **2011**, *21*, 2208–2215.
- (18) Kosonen, H.; Valkama, S.; Nykänen, a.; Toivanen, M.; ten Brinke, G.; Ruokolainen, J.; Ikkala, O. Functional Porous Structures Based on the Pyrolysis of Cured Templates of Block Copolymer and Phenolic Resin. *Adv. Mater.* **2006**, *18*, 201–205.
- (19) Deng, Y.; Yu, T.; Wan, Y.; Shi, Y.; Meng, Y.; Gu, D.; Zhang, L.; Huang, Y.; Liu, C.; Wu, X.; *et al.* Ordered Mesoporous Silicas and Carbons with Large Accessible Pores Templated from Amphiphilic Diblock Copolymer Poly(ethylene Oxide)-B-Polystyrene. *J. Am. Chem. Soc.* **2007**, *129*, 1690–1697.
- (20) Zhang, J.; Deng, Y.; Wei, J.; Sun, Z.; Gu, D.; Bongard, H.; Liu, C.; Wu, H.; Tu, B.; Schüth, F.; *et al.* Design of Amphiphilic ABC Triblock Copolymer for Templating Synthesis of Large-Pore Ordered Mesoporous Carbons with Tunable Pore Wall Thickness. *Chem. Mater.* **2009**, *21*, 3996–4005.
- (21) Wei, J.; Deng, Y.; Zhang, J.; Sun, Z.; Tu, B.; Zhao, D. Large-Pore Ordered Mesoporous Carbons with Tunable Structures and Pore Sizes Templated from Poly(ethylene Oxide)-B-Poly(methyl Methacrylate). *Solid State Sci.* **2011**, *13*, 784–792.

- (22) Deng, Y.; Liu, J.; Liu, C.; Gu, D.; Sun, Z.; Wei, J.; Zhang, J.; Zhang, L.; Tu, B.; Zhao, D. Ultra-Large-Pore Mesoporous Carbons Templated from Poly(ethylene Oxide)- B -Polystyrene Diblock Copolymer by Adding Polystyrene Homopolymer as a Pore Expander. *Chem. Mater.* **2008**, *20*, 7281–7286.
- (23) Li, J.; Lin, Y.; Kuo, S. From Microphase Separation to Self-Organized Mesoporous Phenolic Resin through Competitive Hydrogen Bonding with Double-Crystalline Diblock Copolymers of Poly(ethylene Oxide- B -E-Caprolactone). *Macromolecules* **2011**, *44*, 9295–9309.
- (24) Wang, X.; Liang, C.; Dai, S. Facile Synthesis of Ordered Mesoporous Carbons with High Thermal Stability by Self-Assembly of Resorcinol-Formaldehyde and Block Copolymers under Highly Acidic Conditions. *Langmuir* **2008**, *24*, 7500–7505.
- (25) Huang, Y.; Cai, H.; Feng, D.; Gu, D.; Deng, Y.; Tu, B.; Wang, H.; Webley, P. a; Zhao, D. One-Step Hydrothermal Synthesis of Ordered Mesostructured Carbonaceous Monoliths with Hierarchical Porosities. *Chem. Commun. (Camb)*. **2008**, 2641–2643.
- (26) Liang, C.; Dai, S. Dual Phase Separation for Synthesis of Bimodal Meso-/macroporous Carbon Monoliths. *Chem. Mater.* **2009**, *21*, 2115–2124.
- (27) Mayes, R. T.; Tsouris, C.; Kiggans Jr., J. O.; Mahurin, S. M.; DePaoli, D. W.; Dai, S. Hierarchical Ordered Mesoporous Carbon from Phloroglucinol-Glyoxal and Its Application in Capacitive Deionization of Brackish Water. *J. Mater. Chem.* **2010**, *20*, 8674.
- (28) Hao, G.-P.; Li, W.-C.; Qian, D.; Wang, G.-H.; Zhang, W.-P.; Zhang, T.; Wang, A.-Q.; Schüth, F.; Bongard, H.-J.; Lu, A.-H. Structurally Designed Synthesis of Mechanically Stable Poly(benzoxazine-Co-Resol)-Based Porous Carbon Monoliths and Their Application as High-Performance CO₂ Capture Sorbents. *J. Am. Chem. Soc.* **2011**, *133*, 11378–11388.
- (29) Hao, G.-P.; Li, W.-C.; Wang, S.; Wang, G.-H.; Qi, L.; Lu, A.-H. Lysine-Assisted Rapid Synthesis of Crack-Free Hierarchical Carbon Monoliths with a Hexagonal Array of Mesopores. *Carbon N. Y.* **2011**, *49*, 3762–3772.
- (30) Wei, H.; Lv, Y.; Han, L.; Tu, B.; Zhao, D. Facile Synthesis of Transparent Mesostructured Composites and Corresponding Crack-Free Mesoporous Carbon/Silica Monoliths. *Chem. Mater.* **2011**, *23*, 2353–2360.
- (31) Florent, M.; Xue, C.; Zhao, D.; Goldfarb, D. Formation Mechanism of Cubic Mesoporous Carbon Monolith Synthesized by Evaporation-Induced Self-Assembly. *Chem. Mater.* **2012**, *24*, 383–392.
- (32) Leibler, L. Theory of Microphase Separation in Block Copolymers. *Macromolecules* **1980**, *13*, 1602–1617.

- (33) Toombes, G. E. S.; Finnefrock, A. C.; Tate, M. W.; Ulrich, R.; Wiesner, U.; Gruner, S. M. A Re-Evaluation of the Morphology of a Bicontinuous Block {Copolymer–Ceramic} Material. *Macromolecules* **2007**, *40*, 8974–8982.
- (34) Epps, T. H.; Cochran, E. W.; Bailey, T. S.; Waletzko, R. S.; Hardy, C. M.; Bates, F. S. Ordered Network Phases in Linear Poly(isoprene-B-Styrene-B-Ethylene Oxide) Triblock Copolymers. *Macromolecules* **2004**, *37*, 8325–8341.
- (35) Stefik, M.; Wang, S.; Hovden, R.; Sai, H.; Tate, M. W.; Muller, D. a.; Steiner, U.; Gruner, S. M.; Wiesner, U. Networked and Chiral Nanocomposites from ABC Triblock Terpolymer Coassembly with Transition Metal Oxide Nanoparticles. *J. Mater. Chem.* **2012**, *22*, 1078.
- (36) Ferrari, a.; Robertson, J. Interpretation of Raman Spectra of Disordered and Amorphous Carbon. *Phys. Rev. B* **2000**, *61*, 14095–14107.
- (37) Tuinstra, F.; Koenig, L. Raman Spectrum of Graphite. *J. Chem. Phys.* **1970**, *53*, 1126–1130.
- (38) Ko, T.-H.; Kuo, W.-S.; Chang, Y.-H. Raman Study of the Microstructure Changes of Phenolic Resin during Pyrolysis. *Polym. Compos.* **2000**, *21*, 745–750.
- (39) Subban, C. V.; Smith, I. C.; Disalvo, F. J. Interconversion of Inverse Opals of Electrically Conducting Doped Titanium Oxides and Nitrides. *Small* **2012**, *8*, 2824–2832.
- (40) Bailey, T. S.; Hardy, C. M.; Epps, T. H.; Bates, F. S. A Noncubic Triply Periodic Network Morphology in Poly(isoprene-B-Styrene-B-Ethylene Oxide) Triblock Copolymers. *Macromolecules* **2002**, *35*, 7007–7017.
- (41) Gregg, S. J.; Sing, K. S. W., Adsorption, Surface Area and Porosity , 2nd Edition, Academic Press, London 1982.
- (42) Barrett, E. P.; Joyner, L. G.; Halenda, P. P. The Determination of Pore Volume and Area Distributions in Porous Substances. I. Computations from Nitrogen Isotherms. *J. Am. Chem. Soc.* **1951**, *73*, 373–380.

CHAPTER 3

CARBON-SULFUR COMPOSITES FROM CYLINDRICAL AND GYROIDAL MESOPOROUS

CARBONS WITH TUNABLE PROPERTIES IN LITHIUM-SULFUR BATTERIES

Abstract

Sulfur is a high-potential candidate for next generation electrical energy storage due to its abundance, low cost and non-toxicity. The electrically insulating property of sulfur and lithium sulfide and the solubility of polysulfides in the electrolyte, however, pose great challenges for the realization of long-lasting lithium-sulfur batteries for commercial applications. In recent years, much attention has been focused on mesoporous carbon-sulfur composites as cathode material. Fundamental studies on the performance of such electrodes correlated to systematic variations of structural and porosity characteristics of the carbons remain elusive, however. In this work a variety of block copolymer (BCP) derived mesoporous carbons were studied with uniform and tunable pore sizes as sulfur hosts. Morphologies included hexagonally packed cylinders and co-continuous gyroids, with one- and three-dimensional porosity, respectively. Dependence of the cyclability of carbon-sulfur composites was tested on mesopore size, morphology and carbonization temperatures of up to 1600 °C. Results demonstrate the significant impact of the carbon properties related to the carbonization temperature, such as heteroatom content, on capacity retention of carbon-sulfur cathodes, while morphological parameters and mesopore sizes (between 15 and 40 nm) of carbons studied here have little influence on performance. The high-temperature derived gyroidal mesoporous carbons (1600 °C) exhibited remarkable structural stability towards activation. This allowed for the introduction of nanopores (<4 nm) with a large pore volume of 0.8 cm³ g⁻¹ in addition to the BCP-derived mesopores (15-40 nm), with total pore volumes over 2 cm³ g⁻¹, surface areas over 2000 m² g⁻¹, and retention of the well-ordered gyroidal morphology. Highly activated, gyroidal carbon-sulfur composites showed good cyclability and rate capability with discharge capacities after 100 cycles of 831 mAh g⁻¹ at 0.1C and 730 mAh g⁻¹ at 1C.

Reprinted with permission from Werner, J. G., Johnson, S. S., Vijay, V., Wiesner, U.: Carbon-Sulfur Composites from Cylindrical and Gyroidal Mesoporous Carbons with Tunable Properties in Lithium-Sulfur Batteries, *Chem. Mater.* **27**, 3349-3357 (2015). Copyright 2015 American Chemical Society.

Introduction

Energy production, storage and transportation is one of the biggest challenges that societies around the globe face in the twenty first century. With the emergence of sustainable and renewable energy sources such as solar cells and wind energy, new energy management concepts will be unavoidable.^{1,2} The inherent intermittence of solar and wind make advances in the field of energy storage inevitable. This need is enhanced by the increasing demand for consumer electronics and electric transportation systems.³⁻⁵ However, due to varying requirements on energy storage characteristics for different applications, it is unlikely that one system will fit all needs.^{5,6}

Sulfur has been proposed as a very intriguing cathode material for lithium-ion or lithium-metal batteries for its abundance, cheapness, and low toxicity, making it a very promising candidate for large scale applications.^{7,8} Additionally, the charge storage mechanism *via* conversion reaction allows for a high specific capacity of 1672 mAh g⁻¹ of sulfur when fully reduced to Li₂S.⁹ During the complex reduction and oxidation mechanisms between sulfur and lithium sulfide, a variety of polysulfides are involved that are soluble in most commonly employed organic electrolyte solvents.^{10,11} This solubility leads to loss of the active material over charge and discharge, and therefore, to poor capacity retention over cycling. Additionally, the diffusion of polysulfides during charging and continued reduction/oxidation on anode and cathode, respectively, leads to low energy efficiency (shuttle effect).⁷ While the shuttle effect can be mitigated by adding lithium nitrate to the electrolyte, the poor cycling performance remains.^{12,13}

Mesoporous carbon materials have attracted much attention as sulfur hosts for lithium-sulfur batteries since 2009, when the Nazar group reported success in the diminution of polysulfide dissolution and correspondingly an improvement in capacity retention over cycling using the mesoporous carbon CMK-3 and infiltrating its small mesopores with sulfur.¹⁴

A lot of work on porous carbon structures for lithium sulfur batteries has subsequently been reported.¹⁵⁻²⁸ More recently, heteroatom doped carbon hosts, polymeric, and inorganic hosts or reservoirs for sulfur have been explored.²⁹⁻³³ Other approaches involve electrolyte modifications.^{34,35} Reported

carbon structures range from spheres, tubes, micro- and mesoporous carbide-derived-carbons (CMCs), ordered and disordered mesoporous and macroporous carbon frameworks all the way to graphene.^{22,36-41} Pore sizes over multiple orders of magnitude have been studied, ranging from microns down to micropores that are smaller than the S₈ molecule.^{42,43} Recently, some systematic studies on porous carbon spheres in lithium-sulfur batteries and the influence of conductivity, particle, and pore morphology with pore sizes below 10 nm were reported.^{44,45} However, while characteristics of carbon materials vary dramatically between different reports, carbon-sulfur composites often show similar performance. Moreover, due to differences in carbon precursors, templating chemistry, carbonization conditions, etc., across different literature reports it is rather difficult to reach conclusions about the influence of specific structural and porosity characteristics on battery performance.

Here, we present a fundamental study on ordered mesoporous carbons as hosts for sulfur with a variety of structures, porosities, and thermal histories, all derived from the co-assembly of block copolymers (BCP) with phenolic-formaldehyde resols. Due to the nature of BCP structure direction, carbon morphologies with different dimensionalities, pore sizes and porosities can be achieved using the same polymer and precursor chemistry by simply changing copolymer to precursor ratios.⁴⁶ We synthesized ordered mesoporous carbons with hexagonally packed, one-dimensional cylindrical mesopores, three-dimensionally (3D) networked gyroidal minority mesopores, and 3D networked gyroidal majority mesopores. Mesopore sizes were tuned between 15 and 40 nm. Mesoporous carbons show exceptionally good thermal stability up to 1600 °C, allowing for thermal tunability of the materials over a significant range of temperatures. The thermal history of carbonaceous materials is of great importance, since the heteroatom content, graphitization, conductivity and microporosity can be significantly altered through the carbonization temperature. We demonstrate that these factors have a significant influence on the cycling performance of carbon-sulfur composites. Furthermore, physical activation with carbon dioxide was used to investigate the influence of micropores and small mesopores on the performance as a sulfur host in lithium-sulfur batteries. High-temperature treated gyroidal mesoporous carbons show remarkable structural stability towards this kind of activation. This allowed

introduction of pore volumes up to $0.8 \text{ cm}^3 \text{ g}^{-1}$ for pores smaller than 4 nm, in addition to the BCP derived larger mesopores, without collapse of the gyroidal mesostructure. Results show that these pores can greatly improve capacity retention. However, an electrolyte-dependent decrease in discharge potential over cycling is observed for these highly activated mesoporous carbons. Activated gyroidal mesoporous carbons exhibited good rate capability, likely due to bimodal nanopore size distributions. Overall, the great tunability of BCP structure direction and the exceptional stability of the mesoporous carbons allowed identification of the most influential parameters of carbon hosts towards lithium-sulfur battery performance. Our work demonstrates that heteroatom content, such as significant amount of oxygen in the carbon host due to low-temperature carbonization, as well as microporosity have great impact on the capacity retention capability.

Results and Discussion

Structural properties can have significant impact on the performance of nanomaterials in device applications. Understanding these correlations requires precise synthetic control over characteristics such as material's composition, dimensionality, thickness and pore size. In this study, we used the co-assembly of the triblock terpolymer poly(isoprene)-*block*-poly(styrene)-*block*-poly(ethylene oxide) (ISO) and phenol- or resorcinol-formaldehyde resols to obtain ordered mesoporous carbon materials with good control over a variety of the afore mentioned properties that were tested as host materials for sulfur regarding their performance in lithium-sulfur batteries. The use of BCP structure direction allows for the independent control over morphology, pore size, and porosity. Three distinctly different carbon morphologies, namely the double gyroid (G^D) matrix, the single alternating gyroid (G^A) network, and carbons with hexagonally packed cylinder pores, were prepared and characterized following procedures described previously.⁴⁶ BCP compositions, molecular weights, PDIs, terpolymer to precursor ratios for the carbon materials as well as the carbon sample notation used throughout this study are summarized in Table 3.1. Scanning electron microscopy images of the materials are shown in Figure 3.1 together with illustrations of carbon and sulfur composite structures. While the carbon phase is three-dimensional in all

Table 3.1. Triblock terpolymer compositions, resols loadings for ordered mesoporous carbons, and carbon sample notations used in this study.

| Polymer | Carbon | M_N^a / g/mol | PDI | $f_V(\text{PI})^b$ / vol % | $f_V(\text{PS})^b$ / vol % | $f_V(\text{PEO})^b$ / vol % | Resols: ISO ^c |
|---------|----------------------|-----------------|------|----------------------------|----------------------------|-----------------------------|--------------------------|
| ISO#1 | G ^D MC-15 | 38,891 | 1.06 | 17.7 | 32.5 | 49.8 | 0.58 : 1 |
| ISO#2 | Hex-25 | 55,993 | 1.06 | 16.7 | 31.2 | 52.1 | 1.20 : 1 |
| ISO#3 | G ^D MC-39 | 108,311 | 1.07 | 17.7 | 31.6 | 50.7 | 0.50 : 1 |
| ISO#5 | G ^A MC-35 | 68,959 | 1.04 | 33.1 | 62.0 | 4.9 | 0.32 : 1 |

^a determined by combination of ¹H-NMR and GPC; ^b determined by ¹H-NMR; ^c weight ratio.

structures, the porous phase is only three-dimensionally connected in the gyroidal morphologies and is one-dimensional in the cylindrical case. As illustrated in Figure 3.1, the two gyroidal morphologies differ in their "openness". While the single alternating gyroidal network is constituted of thin carbon struts that form a 3D-net with very open and unrestricted porosity in which the sulfur infiltrates, the double gyroidal matrix represents a continuous carbon wall that is wrapped up into 3D-space, forming a torturous and more enclosed pore-network with a cylindrical pore cross-section.

All ordered carbon-sulfur composites were prepared using liquid infiltration of sulfur at 155 °C as often employed in literature with a 1:1 weight ratio of carbon to sulfur.¹⁴ X-ray diffraction patterns of carbon sulfur composites show only a broad signal in the range of the main sulfur peaks (between 20 and 30 degrees, Figure S3.6), demonstrating that the melt-infiltrated sulfur is amorphous in all of the carbon hosts, independent of the carbon history. Electrodes were casted on aluminum foil current collectors without conductive additives and with 10 wt% poly(vinylidifluoride) (PVDF) binder. Due to the amount of sulfur and electrolyte in the tested coin cells, it can be assumed that the polysulfides are solvated during reduction and oxidation. However, it is worth noting that Wang *et al.* proposed that polysulfides in micropores react in a quasi-solid-state.²⁷ Since the batteries were tested at a slow charge/discharge rate of 0.1C, our results are a good estimation of the degree of interaction between the polysulfide species and the carbon host during charge and discharge of the batteries.

Influence of carbon mesostructure: First, we investigated the "physical" polysulfide sequestration capabilities of the mesoporous carbons with different morphologies and corresponding capacity retention

Table 3.2. Structural characteristics of ordered mesoporous carbons.

| Carbon | Pore size ^a / nm | Pore volume ^b (micropore ^c) / cm ³ /g | BET surface area (micropore ^c) / m ² /g | Carbon : oxygen ratio ^d |
|-----------------------------|-----------------------------|--|---|---------------------------------------|
| G ^A MC-1600°C | 31 ± 9 | 1.41 (0.05) | 348 (120) | 93:7 |
| Hex-25-1600°C | 25 ± 6 | 0.46 (0.03) | 167 (77) | - |
| G ^D MC-39-1600°C | 39 ± 5 | 1.15 (0.03) | 202 (74) | 90:10 |
| G ^D MC-39-900°C | 39 ± 4 | 1.56 (0.23) | 692 (506) | 85:15 |
| G ^D MC-15-1600°C | 16 ± 2 | 0.80 (0.06) | 318 (136) | 91:9 |
| G ^D MC-15-900°C | 15 ± 2 | 0.89 (0.20) | 606 (427) | 88:12 |

^a determined by BJH-model applied to nitrogen sorption isotherms with the error representing the FWHM; ^b based on amount adsorbed at relative pressure of 0.99; ^c determined using the t-plot method; ^d based on XPS data.

during cycling using materials that were carbonized at 1600 °C. The very high carbonization temperature yields ordered mesoporous carbons with negligible microporosity (less than 7% of the pore volume, Table 3.2) and very low oxygen content that is associated with low surface functionality.⁴⁶ This assures that any effect on the cycling performance can be associated with the mesoporosity, its dimensionality and pore size. Carbon hosts for sulfur with the three aforementioned structures and pore sizes between 25 and 40 nm and pore volumes ranging from 0.5 to 1.4 cm³ g⁻¹ (Figure 3.1e and Table 3.2) but otherwise identical properties were tested at a charge and discharge rate of 0.1C to assess the ability of the mesoporous carbon hosts to prevent capacity fading and loss of sulfur/polysulfides. Batteries were tested with and without the addition of lithium nitrate, which has been reported to improve the coulombic efficiency through passivation of the lithium metal anode.^{12,13} The discharge capacities over the first 100 cycles are shown in Figure 3.1f. All carbon hosts show very similar performance over cycling with a relatively low initial capacity (below 1200 mAh g⁻¹) and rapid capacity fade over the first 10 cycles, resulting in less than 500 mAh g⁻¹ after 100 cycles for all materials. No substantial differences in capacity retention were observed between the various carbon morphologies, despite significant differences in pore volume and dimensionality. It is worth mentioning that the pore volume of the hexagonally packed cylindrical carbon is significantly smaller than those of the gyroidal carbons and close to the volume occupied by sulfur in the 1:1 carbon-sulfur composites. Therefore, we also tested the cylindrical carbon

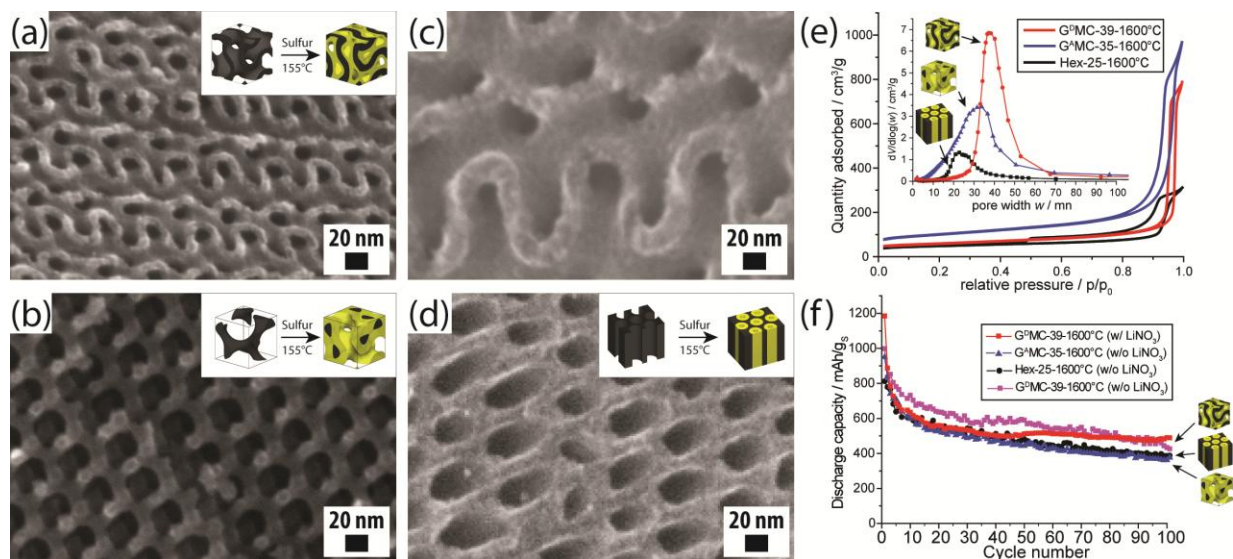


Figure 3.1. (a-d) Scanning electron microscopy (SEM) images of the four investigated ordered mesoporous carbon materials carbonized at 1600 °C: (a) Double gyroidal carbon with 15 nm pore size (G^D MC-15-1600°C), (b) single gyroidal carbon network (G^A MC-1600°C), (c) double gyroidal carbon with 39 nm pore size (G^D MC-39-1600°C), and (d) hexagonally packed cylindrical carbon (Hex-25-1600°C). The images have the same field of view for facile comparison. Insets in (a-d) show illustrations of the ordered carbon mesostructures and carbon-sulfur composites. (e) Nitrogen sorption isotherms and corresponding BJH pore size distribution (inset) of G^D MC-39-1600°C (red), G^A MC-1600°C (blue), and Hex-25-1600°C (black). (f) Discharge capacities of the first 100 cycles at 0.1C of 1:1 carbon-sulfur composites from G^A MC-1600°C (blue), Hex-25-1600°C (black), G^D MC-39-1600°C with (red) and without (purple) lithium nitrate as electrolyte additive.

for carbon to sulfur ratios of 2:1, yielding very similar cycling performance (Figure S3.1). The addition of lithium nitrate to the electrolyte improved the coulombic efficiency from about 80% to close to 100% (Figure S3.1), however, without any difference in cyclability leading to similarly large capacity fade with or without the additive, as demonstrated for the double gyroidal carbon host with 39 nm pore size (Figure 3.1f).

Influence of mesopore size: The influence of pore size of the mesoporous carbon was investigated using two double gyroidal mesoporous carbon materials with pore sizes of 15 nm and 39 nm, referred to as G^D MC-15-1600°C and G^D MC-39-1600°C, respectively (Figure 3.1a,c and Figure 3.2). While both high-temperature treated gyroidal mesoporous carbons showed similar initial capacities of close to 1200 mAh g^{-1} in the first cycle, the 15 nm pore sized carbon exhibited a smaller capacity fade over the

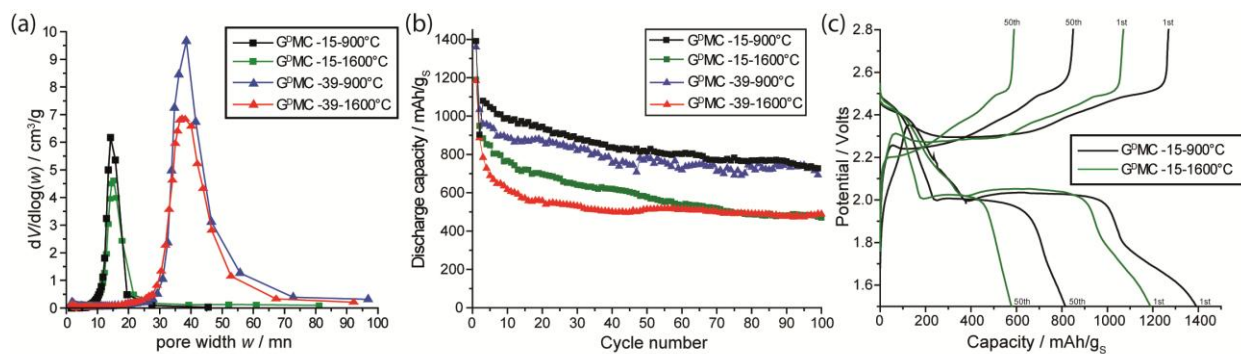


Figure 3.2. (a) BJH pore size distributions of double gyroidal mesoporous carbons with 15 or 39 nm pore size and carbonized at 900 °C or 1600 °C. (b) Discharge capacities of the first 100 cycles at 0.1C of 1:1 carbon-sulfur composites from G^DMC-39-1600°C (red triangle), G^DMC-15-1600°C (green square), G^DMC-39-900°C (blue triangle), and G^DMC-15-900°C (black square), demonstrating the significant impact of carbonization temperature with little influence of mesopore size on cycling stability. (c) 1st and 50th charge and discharge curves at 0.1C of 1:1 carbon-sulfur composites from G^DMC-15-1600°C (green) and G^DMC-15-900°C (black) demonstrating sharp discharge plateaus at the expected voltages without voltage decay over cycling for either of the host materials.

first 50 cycles than the 39 nm gyroidal carbon. After 100 cycles, however, the capacity for both carbon-sulfur composites were at similarly low values of 470 and 489 mAh g⁻¹ for the 15 and 39 nm carbon, respectively.

These results suggest that "physical" trapping of polysulfides using high-temperature treated mesoporous carbons with pore sizes between 15 and 39 nm is not effective in preventing the dissolution and loss of polysulfides during battery cycling, independent of the structural and porosity characteristics.

Influence of carbonization temperature: Carbonization temperature is an important parameter in the synthesis of carbon materials to influence the physical and chemical properties of the material. High-temperature carbonization typically results in more graphitic characteristics, such as higher conductivity, sp²-hybridization and purity. Mesoporous carbons heat-treated at lower temperatures often possess a significant amount of microporosity and heteroatom content, which can be beneficial for some applications. In order to investigate the impact of carbonization temperature on the capacity

retention of the respective carbon-sulfur composites, we tested the two above mentioned double gyroidal carbon materials with pore sizes of 15 and 39 nm after heat treatment at only 900 °C, referred to as G^DMC-15-900°C and G^DMC-39-900°C. While the mesopore size distribution for the two different

carbonization temperatures of 900 °C and 1600 °C was almost identical, the contribution of microporosity to the total pore volume and surface area was much more significant for the lower carbonization temperature (Figure 3.2a and Table 3.2). The oxygen content was higher, as expected, for the 900 °C materials. The differences in these physical and chemical properties of the mesoporous carbons had a dramatic influence on the cyclability of the resulting carbon-sulfur nanocomposites. The initial capacity was significantly increased to 1392 mAh g⁻¹ and the capacity fade was vastly reduced, retaining a high discharge capacity of 728 mAh g⁻¹ after 100 cycles for G^DMC-15-900°C, more than 50% higher than its 1600 °C counterpart (Figure 3.2b). The initial capacity fade and the average capacity fades per cycle between the 3rd and 100th cycle are summarized in Table S3.1. The numbers demonstrate that the better performance of the low-temperature carbonized hosts are due to both, higher initial capacity as well as significantly reduced capacity fade over the cycling period.

The discharge curves displayed in Figure 3.2c show two distinct plateaus at 2.4 V and 2.05 V for either of the host materials carbonized at different temperatures, indicating no significant influence of the carbonization temperature of the mesoporous carbons on the sulfur electrochemistry. Therefore, the improved capacity retention of G^DMC-15-900°C and G^DMC-39-900°C can be attributed to the existence of a significant amount of microporosity and surface functionality from the higher oxygen content. Again, little difference in battery performance was observed for the two pore sizes. The results of these carbons are very similar to a number of literature reports on mesoporous carbons as sulfur hosts that exhibit a variety of structural and porosity characteristics with often only one common parameter, that is a relatively low carbonization temperature. Results suggest that materials properties associated with low carbonization temperature such as higher oxygen content (surface functional groups) and microporosity have a significant influence on the performance as a sulfur host in lithium-sulfur batteries. In contrast, structural properties of ordered mesoporous carbons as studied here have little or no impact.

Influence of micro- to mesoporosity from activation:

Effects of activation on structural characteristics. In order to assess the influence of micropores and small mesopores without significant contributions of heteroatoms, we activated our high temperature treated double gyroidal mesoporous carbons (referred to as aG^DMC). To that end, after carbonization of the materials at 1600 °C as described above, the gyroidal carbons were subjected to another heat treatment at 950 °C under carbon dioxide (CO₂) for a specified time. This physical activation method leads to homogeneous activation of carbon materials without the introduction of heteroatoms, such as oxygen, due to the extraction mechanism of individual carbon atoms.⁴⁷ The treatment of the ordered gyroidal mesoporous carbons prior to the activation yields very stable and resistant materials, which allows for good control over the degree of activation through the exposure time. We subjected high temperature derived (1600 °C) gyroidal mesoporous carbons with pore sizes of 15 nm and 39 nm to 6 hours of activation (aG^DMC-15-6h and aG^DMC-39-6h), while the 15 nm pore sized material was also subjected to 10 hours of activation (aG^DMC-15-10h). The CO₂-activation leads to a significant material loss of up to 79 wt% for aG^DMC-15-10h. Despite the large loss of material, the gyroidal mesostructure and the mesoporosity are remarkably well preserved as demonstrated by SEM, small angle X-ray scattering (SAXS), and sorption analysis (Figure 3.3). The SAXS pattern of the un-activated G^DMC-15-1600°C shows the allowed (211), (022), (321), (042), and (332) reflections, as well as the forbidden (110) and (200) reflections, which appear, most likely, due to non-uniform shrinkage of the structure during the synthesis lowering the symmetry (Figure 3.3b). After CO₂-activation for 6 hours, four of the allowed and the two forbidden reflections still appear, demonstrating good structure retention. Remarkably, after 10 hours of activation, accompanied by 79% weight loss, the material still shows a broad scattering peak corresponding to the overlay of the (200), (211), and (022) reflections as well as a broad higher order peak at the (332) position. Peak broadening and loss of higher order peaks can be explained with the increased surface roughness due to the introduction of micro- and small mesopores after activation resulting in diffuse interfaces between carbon and void space and, therefore, to the loss of scattering resolution.

Table 3.3. Structural characteristics of activated gyroidal mesoporous carbons.

| Carbon | Pore size ^a / nm | Pore volume ^b (micropore ^c) / cm ³ /g | BET surface area (micropore ^c) / m ² /g | Weight loss |
|----------------------------|-----------------------------|--|---|-------------|
| aG ^D MC-15- 6h | 15 ± 2 | 1.32 (0.28) | 1076 (611) | 26 wt% |
| aG ^D MC-15- 10h | 14 ± 2 | 2.45 (0.01) | 2029 (78) | 78 wt% |
| aG ^D MC-39- 6h | 40 ± 4 | 2.25 (0.31) | 1341 (700) | 37 wt% |

^a determined by BJH-model applied to nitrogen sorption isotherms with the error representing the FWHM; ^b based on amount adsorbed at relative pressure of 0.99; ^c determined using the t-plot method.

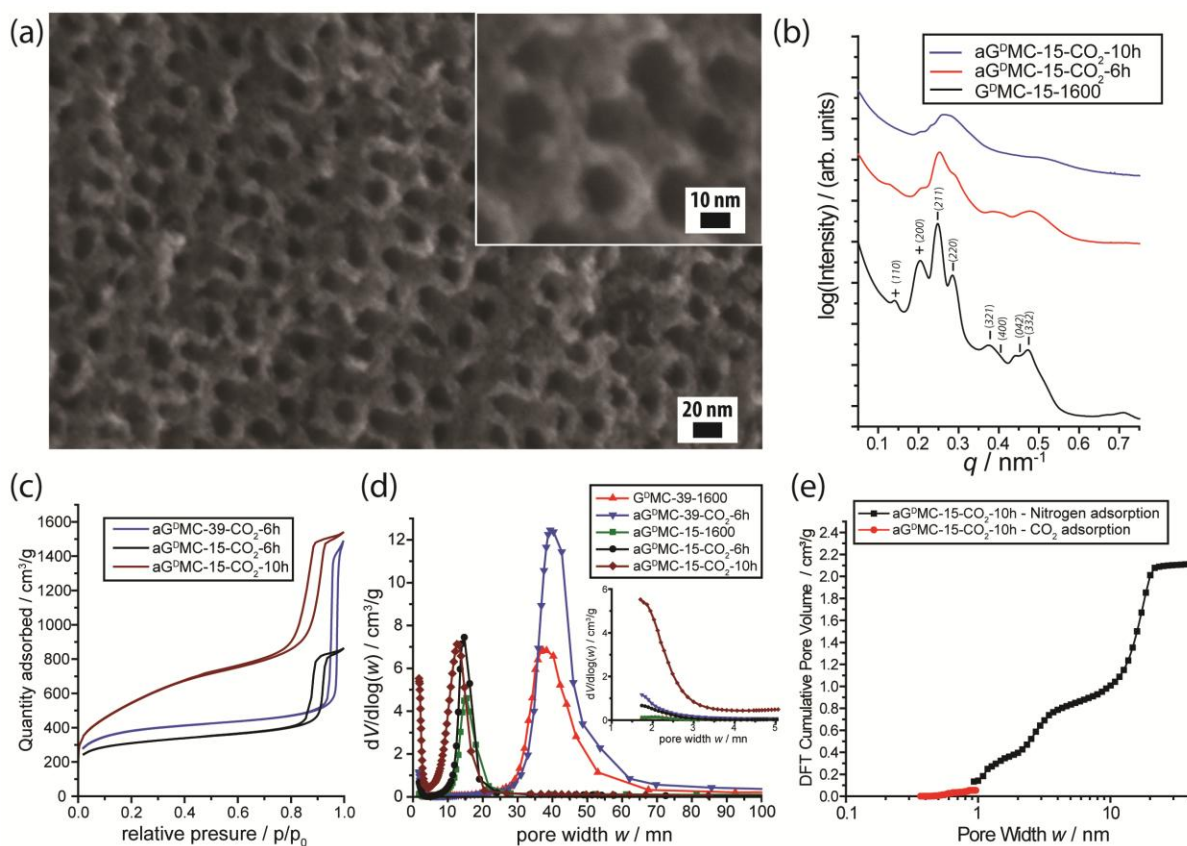


Figure 3.3. Structural and porosity characterization of CO₂-activated high temperature (1600 °C) derived gyroidal mesoporous carbons (aGDMC): (a) SEM image of 15 nm gyroidal mesoporous carbon after 10 hours of activation (aGDMC-15-10h) demonstrating good retention of gyroidal mesostructure during activation and roughening of the mesopore walls due to introduction of small nanopores. (b) Small-angle X-ray scattering (SAXS) patterns of GDMC-15-1600 °C before (black), and after CO₂-activation for 6 hours (aGDMC-15-6h, red), and for 10 hours (aGDMC-15-10h, blue). The patterns are shifted vertically for clarity. (c) Nitrogen sorption isotherms and (d) BJH pore size distributions (PSDs) of all activated double gyroidal mesoporous carbons. For comparison, the PSDs of the non-activated parent gyroidal mesoporous carbons are also plotted. The inset in (d) depicts an enlarged section at small pore width, showing the significant contribution of pores below 4 nm to the pore volume for aGDMC-15-10h. (e) Cumulative pore volume as a function of pore width analyzed using the NL-DFT model for slits on the nitrogen (black) and carbon dioxide (red) adsorption isotherms of aGDMC-15-10h, demonstrating the large pore volume contributed by the activation-induced small nanopores below 4nm.

The effect of activation is also observable in the SEM images of aG^DMC-15-10h (Figure 3.3a). The SEM images show the well preserved gyroidal mesostructure with small pores distributed over the walls. The change in porosity during activation was further characterized using nitrogen, argon and CO₂ sorption analysis. In Figure 3.3c and d, the nitrogen isotherms and BJH pore size distributions (PSD) of the activated materials are shown, respectively. For reference, the pore size distributions of the parent, non-activated gyroidal mesoporous carbons are also plotted. The BET surface area increase with activation was confirmed using nitrogen and argon adsorption, yielding 2029 m² g⁻¹ (N₂) and 2078 m² g⁻¹ (Ar), respectively, for 10 hours of activation (Figure 3.3c and Table 3.3). The BJH pore size distribution confirms the preservation of the narrowly dispersed mesoporosity with an increase in specific mesopore volume (area under the peak) due to weight loss during the activation process. After 6 hours of activation, the micropore area and volume significantly increased, leading to a total surface area of more than 1000 m² g⁻¹ (Table 3.3). Additionally, the BJH pore size distributions of the 6 hours activated carbons show the appearance of small mesopores (below 3 nm). For aG^DMC-15-10h, the t-plot-microporosity decreased and a large fraction of small mesopores (below 4 nm) is apparent from the PSD. For a better evaluation of the bimodal pore size distribution of aG^DMC-15-10h, we used DFT analysis on the CO₂ and low pressure nitrogen adsorption isotherms (Figure 3.3e and S3.3). Two kinds of porosity contribute significantly to the total pore volume; about 1.2 cm³ g⁻¹ from the 15 nm pores of the gyroidal structure, and about 0.8 cm³ g⁻¹ from pores obtained *via* activation with a size of less than 4 nm. The structural stability of the parent gyroidal mesoporous carbon allows for this extensive activation to introduce a large fraction of micropores and small mesopores without destroying the initial ordered mesostructure and mesoporosity.

In order to investigate the location of the sulfur in these carbon hosts, we performed nitrogen adsorption analysis of the sulfur infiltrated 15 nm gyroidal mesoporous carbons heat-treated at 900 °C, 1600 °C, and after activation with CO₂ for 10 hours (Figure S3.5). The results of the measurements suggest that the mesopores of the non-activated carbons are mostly filled with sulfur as expected from the available pore volume. In contrast, for the CO₂ activated carbon the 15 nm sized mesopores are retained

while the small nanopores with sizes below 4 nm disappear after sulfur loading, indicating that for the activated carbon the sulfur resides in the small nanopores.

Effects of activation on battery performance at 0.1C. When tested as sulfur-hosts in lithium-sulfur batteries using TEGDME as electrolyte, the activated gyroidal mesoporous carbons aG^DMC-15-6h and aG^DMC-39-6h perform very similar to the same materials carbonized at only 900 °C without activation, again without any significant differences between the two mesopore sizes (compare Figures 4a with 2b). For example, aG^DMC-39-6h demonstrates a high initial capacity of 1351 mAh g⁻¹ with a slow but steady capacity fade after the first few cycles leading to a value of 720 mAh g⁻¹ after 100 cycles. Considering the large differences in surface area and microporosity between the high-temperature carbonized, activated carbons and the low temperature carbonized materials G^DMC-15-900°C and G^DMC-39-900°C, the significant influence of oxygen content in the low-temperature carbon materials on cycling performance as sulfur-host becomes apparent. Further, we tested the highly activated aG^DMC-15-10h as sulfur host. This material has enough pore volume from pores below 4 nm in size to accommodate the entire amount of sulfur in a 1:1 composite by weight. The composite showed great initial capacity close to 1600 mAh g⁻¹ and good capacity over the first 25 cycles above 1000 mAh g⁻¹ each cycle. However, this material

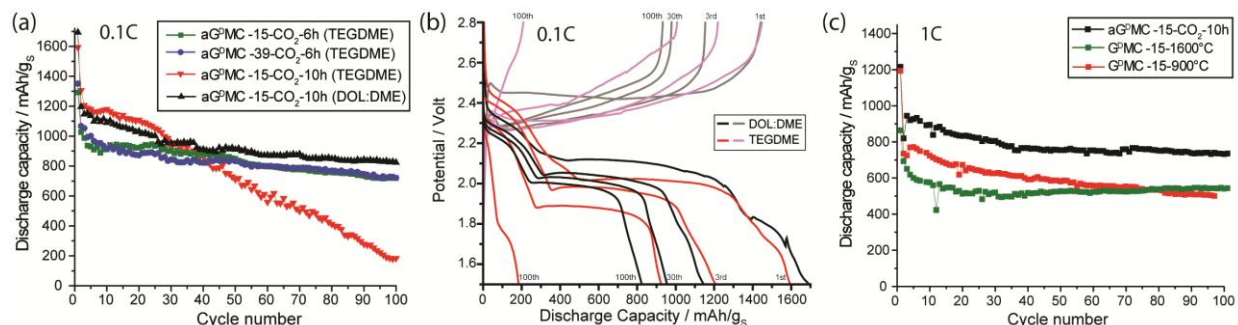


Figure 3.4. (a) Discharge capacities of the first 100 cycles at 0.1C of 1:1 carbon-sulfur composites from aG^DMC-15-6h (green triangle), aG^DMC-39-6h (blue square), aG^DMC-15-10h with TEGDME electrolyte (red triangle) and with DOL:DME electrolyte (black triangle). (b) 1st, 3rd, 30th and 100th charge and discharge curves at 0.1C of 1:1 carbon-sulfur composites of aG^DMC-15-10h with TEGDME electrolyte (discharge: red; charge: magenta) and DOL:DME electrolyte (discharge: black; charge: grey), indicating significant voltage decay of the discharge plateau and increase of the charge plateau over cycling in TEGDME. (c) Discharge capacities of first 100 cycles at 1C of 1:1 carbon-sulfur composites from aG^DMC-15-10h (black), G^DMC-15-1600°C (green), and G^DMC-15-900°C.

reproducibly suffered a dramatic capacity fade after 30-50 good cycles that yielded in capacities of below 500 mAh g⁻¹ after 80 cycles (Figure 3.4a and S4). The sudden increase in capacity fade is accompanied with a decrease in coulombic efficiency to below 80% (Figure S3.4). The discharge curves reveal a significant decrease in the plateau voltage over cycling (Figure 3.4b), indicating an increase in overpotential during charge and discharge of the battery. To investigate the influence of electrolyte on this phenomenon, we tested the same composite (aG^DMC-15-10h filled with sulfur) with the commonly employed mixture of dimethoxy ethane (DME) and dioxolane (DOL), which has been shown to be of advantage for high-rate operation due to lower viscosity. As previously reported, the first discharge plateau corresponding to the formation of long-chain polysulfides appears at a lower voltage, while the second discharge plateau occurs at a higher voltage using the DOL:DME as compared to TEGDME as the electrolyte solvent. This behavior has been associated with the differences in viscosity of the solvents and resultant differences in local concentrations of the different polysulfide species.⁴⁸ Furthermore, voltage decrease over cycling is significantly less when DOL:DME is used. This yields in a cycling performance even better than the less activated or low-temperature carbonized gyroidal carbon materials with discharge capacities above 1000 mAh g⁻¹ for the first 25 cycles and 830 mAh g⁻¹ after 100 cycles. Our results demonstrate the ability of micropores and small mesopores below 4 nm to sequester polysulfides during low-rate cycling and delay capacity decays significantly.

The decrease in discharge voltage that is very significant in TEGDME electrolyte suggests an increase in cell polarization during continued cycling. It is possible that insulating lithium sulfide (Li₂S) continuously forms inside the pores of the carbon host during discharge, without getting oxidized on charge. Therefore, an increase in ionic resistance might lead to the increase in cell polarization over continued cycling. It has been reported that formation of insoluble lithium sulfide (Li₂S) during discharge can lead to electrode passivation before full sulfur utilization.¹¹ This effect, however, strongly depends on the ability of the system to reach equilibrium between sulfur, lithium sulfide, and the different polysulfide species. It was suggested that in equilibrium short-chain polysulfides would first react with left-over oxidized species before being fully reduced and precipitated as Li₂S.⁴⁹ During battery operation, however,

the distribution of sulfur species differs from equilibrium and strongly depends on the electrolyte, local concentration differences, and the general local environment of the polysulfide species.⁴⁹ The lower viscosity solvent system DOL:DME might reduce the electrode passivation due to Li_2S precipitation compared to TEGDME in our small-nanopore carbon host and, therefore, yield better cyclability of the composite.

Effects of activation on battery performance at 1C. The highly activated gyroidal mesoporous carbon material is well suited for higher rate operation due to the bimodal porosity with small micro- and mesopores of enough pore volume to accommodate an equal amount of sulfur with an addition of large mesopores of 15 nm for good electrolyte accessibility. For comparison, we tested three different 15 nm pore sized gyroidal mesoporous carbons; $\text{G}^{\text{D}}\text{MC-15-900}^\circ\text{C}$, $\text{G}^{\text{D}}\text{MC-15-1600}^\circ\text{C}$, and $\text{aG}^{\text{D}}\text{MC-15-10h}$ at a 1C-rate (1672 mA g^{-1}). To aid with conductivity, an additional 10 wt% of carbon black was added to the electrode formulation for the 1C rate tests. Figure 3.4c shows the discharge capacities of the first 100 cycles of the three gyroidal carbon hosts infiltrated with an equal amount of sulfur. Both, the highly activated and the low-temperature carbonized sulfur-host show good initial capacity of about 1200 mAh g^{-1} . While $\text{G}^{\text{D}}\text{MC-15-900}^\circ\text{C}$ shows a large capacity drop after the first cycle with significant further capacity fade to less than 500 mAh g^{-1} after 97 cycles, $\text{aG}^{\text{D}}\text{MC-15-10h}$ demonstrated a moderate capacity drop after the first cycle and very stable cycling performance after that with a retention of 731 mAh g^{-1} after 100 cycles at 1C. The carbon-sulfur composite of the purely mesoporous, high-temperature carbonized material $\text{G}^{\text{D}}\text{MC-15-1600}^\circ\text{C}$, shows low initial capacity of 864 mAh g^{-1} , however, with remarkable cycling stability with virtually no capacity loss between the 15th and the 100th cycle. Since the detrimental effect of the polysulfide migration can be reduced with faster cycling due to slow diffusion, other properties of the carbon host become more important, such as accessibility of the active material (ionic resistance of the electrode) and electronic conductivity. The 1C-rate cycling data demonstrates that the highly porous carbon-sulfur composite from the activated $\text{aG}^{\text{D}}\text{MC-15-10h}$ facilitates fast access to sulfur in the small nanopores due to its bimodal porosity.

Conclusions

In this study, we have systematically investigated the influence of numerous structural and porosity characteristics of ordered mesoporous carbons on the polysulfide sequestration abilities when used in lithium-sulfur batteries. Three different carbon morphologies were compared with three- or one-dimensional porosity, treated at carbonization temperatures of 900 °C and 1600 °C, and exhibiting mesopore sizes between 15 nm and 40 nm. The results clearly demonstrate the importance of carbon properties related to the carbonization temperature, such as heteroatom content, indicating much improved cycling performance for the low temperature (900 °C) carbonized sulfur-hosts with higher oxygen content, while no or little influence of the carbon morphology, mesopore size (between 15 and 40 nm) or pore dimensionality was observed. Furthermore, we show that our high-temperature carbonized gyroidal mesoporous carbon material is structurally stable towards extensive physical activation with CO₂, achieving surface areas above 2000 m² g⁻¹ with retention of the ordered gyroidal mesostructure. This activation introduces a bimodal pore size distribution with small pores below 4 nm in addition to the block copolymer directed mesopores of e.g. 15 nm. The additional small pores exhibit a large pore volume of up to 0.8 cm³ g⁻¹, enough to accommodate all the sulfur in a 1:1 carbon-sulfur composite. This composite exhibits good performance at 0.1C and remarkable capacity retention at a discharge capacity of 1C.

Experimental

Synthesis. Four poly(isoprene)-*block*-poly(styrene)-*block*-poly(ethylene oxide) (ISO) triblock terpolymers were synthesized in a stepwise anionic polymerization as described previously.⁵⁰ Molecular weights ranged from 39 kDa to 108 kDa with polydispersities (PDIs) below 1.1 and varying compositions. BCP compositions, molecular weights, PDIs and terpolymer to precursor ratios used to obtain the different carbon materials are summarized in Table 3.1. Phenol-formaldehyde resols with a molar mass of less than 500 g mol⁻¹ were synthesized using the well known polymerization of phenol and formaldehyde under basic conditions at 70 °C for one hour with a molar ratio of 1:2:0.1 between phenol,

formaldehyde and sodium hydroxide (20 wt% in water).⁵¹ Oligomeric resorcinol-formaldehyde resols were synthesized similarly at room temperature for 10 mins with a molar ratio of 1:0.1:1 of resorcinol (50 wt% in water), sodium hydroxide (20 wt% in water), and formaldehyde. The synthesis procedures of the carbon precursors were previously described in detail.⁴⁶ Ordered mesoporous carbon materials were synthesized using evaporation induced co-assembly of the triblock terpolymers ISO with phenol- or resorcinol-formaldehyde resols.⁴⁶ The respective ISO polymer and phenol-formaldehyde resols were dissolved (4-10 wt%) in a mixture of tetrahydrofuran (THF) and chloroform (1:1 by weight), stirred for 24 hours and cast in a PTFE dish for solvent evaporation at 50 °C. For single gyroidal mesoporous carbons, the respective ISO polymer and resorcinol-formaldehyde resols were dissolved (5 wt%) in THF, stirred for 1 hour and cast in a PTFE dish for solvent evaporation at 50 °C. The organic-organic hybrid films were annealed at 125 °C for 24 hours, and subsequently pyrolyzed under inert gas (nitrogen or argon). For pyrolysis, materials were heated at 1 °C min⁻¹ to 600 °C, held for three hours and then heated to their final temperature (as described below) at 5 °C min⁻¹ and held for 3 hours. For an in-depth description of the characterization of meso- and microstructures of the resulting carbons the reader is referred to reference 46.

For carbon activation, physical activation using carbon dioxide (CO₂) with a flow rate of 1 sccm at a temperature of 950 °C was employed. Powders of the gyroidal mesoporous carbons were heated at a rate of 5 °C min⁻¹ under argon flow to 950 °C at which temperature the gas was changed to CO₂ for a specified amount of time (as described below). The powders were subsequently cooled down to room temperature under argon flow.

Material characterization. Scanning electron microscopy (SEM) of carbonized samples was carried out on a Zeiss LEO 1550 FE-SEM operating at an accelerating voltage of 10-20 kV. For SAXS measurements, small squares of the pyrolyzed films (ca. 2x2 mm²) were cut and placed in the hole of a metal washer that was covered on one side with Kapton tape. Activated powders were placed in glass capillaries with a diameter of 0.9 mm. SAXS measurements were performed at the Cornell High Energy Synchrotron Source (CHESS). The sample to detector distance was 2.6 m and the X-ray wavelength, λ ,

was 1.2015 Å. The scattering vector, q , is defined as $q = (4\pi/\lambda)\sin \theta$, where θ is half of the scattering angle. Nitrogen and argon sorption isotherms were obtained on a Micromeritics ASAP 2020 surface area and porosity analyzer at -196 °C. Carbon dioxide sorption isotherms were obtained at 0 °C. The carbon and carbon-sulfur materials were degassed at 150 °C and room temperature, respectively, under vacuum for at least 10 hours prior to measurements. The specific surface areas were determined using the Brunauer-Emmett-Teller (BET) method.⁵² Mesopore size distributions were calculated using the Barrett-Joyner-Halenda (BJH) method, as well as density functional theory (DFT) analysis on the adsorption isotherms.⁵³⁻⁵⁵ X-ray diffraction patterns were obtained on an Ultima IV multipurpose X-ray diffraction system from Rigaku using Cu K α radiation (40V, 44 mA, wavelength 1.5418 Å) in a 2θ range between 17° to 35° with a speed of 3° min⁻¹.

Composite and electrode preparation. The ordered mesoporous carbon materials with an equal amount of sulfur were ball-milled for 10 mins. These physically mixed carbon-sulfur powders were heated to 155 °C in a sealed flask for infiltration of the sulfur into the mesopores of the carbon. The carbon-sulfur composites were subsequently dispersed in a solution of poly(vinyl difluoride) in N-methyl pyrrolidone with a weight ratio of 45:45:10 of carbon:sulfur:PVDF. For electrodes tested at 1 C, 10 wt% carbon black (Vulcan XC32) were added to the dispersion, while all electrodes tested at 0.1 C did not contain carbon black. Electrodes were casted on aluminum foil as the current collector using a doctor blade, and dried at 80 °C over night. Electrodes with a diameter of 16 mm were used as the working electrode with lithium foil (MTI) as the reference and counter electrode. The electrolyte consisted of 1 molar lithium bis(trifluoromethane)sulfonimide (LiTFSI) in tetraethyleneglycol dimethylether (TEGDME), optionally with 1 wt% lithium nitrate (as described below). For electrodes tested at a rate of 1 C, a 1:1 volume mixture of dimethoxy ethane (DME) and dioxolane (DOL) was used as the electrolyte solvent. Celgard 2020 separators were used. Standard CR2032 coin cells (MTI) were assembled in an argon filled glove box with typical sulfur loadings of >0.8 mg/cm² and 30 μ L of electrolyte.

Electrochemical characterization. Coin cell batteries were tested using a BST8-WA 8-channel battery analyzer from MTI Corporation. Batteries were discharged and charged between 1.5 V and 2.8 V with the

same charging and discharging rate of 0.1 C or 1 C (see text, with 1672 mA g⁻¹ corresponding to 1C) and 5 minutes rest between each step.

Acknowledgement

This work was supported as part of the Energy Materials Center at Cornell (emc²), an Energy Frontier Research Center funded by the U.S. Department of Energy, Office of Science, Basic Energy Sciences under Award # DE-SC0001086. J.G.W. acknowledges support by the U.S. Department of Energy, Office of Science, Basic Energy Sciences, under Award # DE-SC0010560. This work made use of the Cornell Center for Materials Research Shared Facilities supported through the NSF MRSEC program (DMR-1120296). This work was further based upon research conducted at the Cornell High Energy Synchrotron Source (CHESS) supported by the National Science Foundation and the National Institutes of Health/National Institute of General Medical Sciences under NSF award DMR-1332208.

APPENDIX B

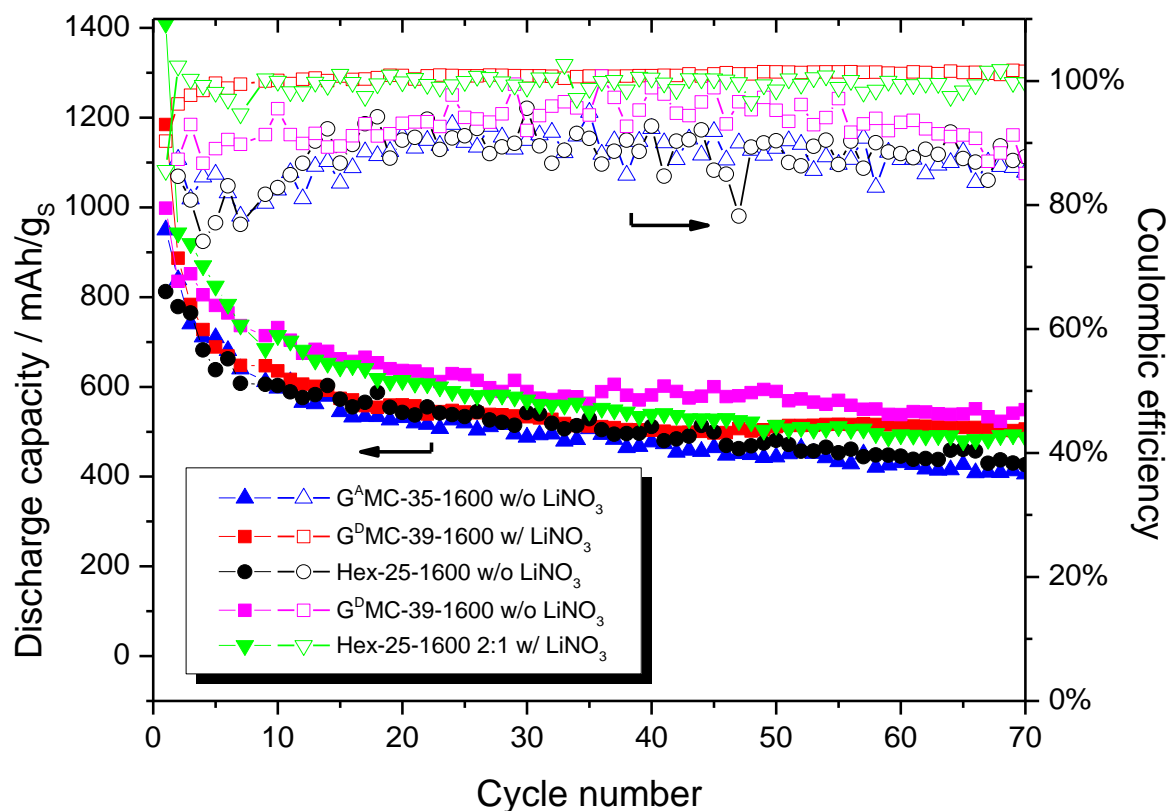


Figure S3.1. Discharge capacities and coulombic efficiencies of first 100 cycles at 0.1C of 1:1 carbon-sulfur composites from G^AMC-1600°C (blue), Hex-25-1600°C (black), and G^DMC-39-1600°C with (red) and without (purple) lithium nitrate as electrolyte additive, and of a 2:1 carbon-sulfur composite from Hex-25-1600°C (green) with lithium nitrate as electrolyte additive. Solid symbols correspond to the discharge capacities, open symbols to the coulombic efficiencies.

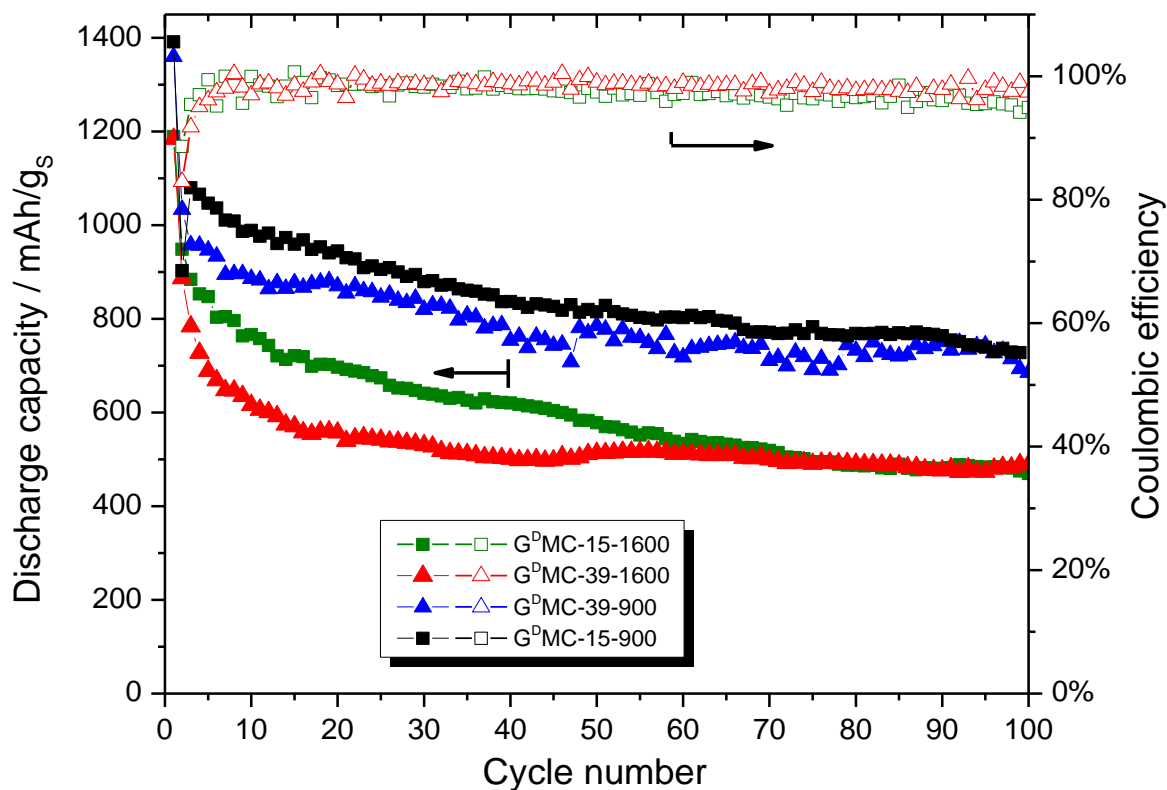


Figure S3.2. Discharge capacities and coulombic efficiencies of the first 100 cycles at 0.1C of 1:1 carbon-sulfur composites from G^DMC-39-1600°C (red triangle), G^DMC-15-1600°C (green square), G^DMC-39-900°C (blue triangle), and G^DMC-15-900°C (black square). Solid symbols correspond to the discharge capacities, open symbols to the coulombic efficiencies.

Table S3.1. Capacity values of the first, third and 100th cycle, initial capacity decay and per cycle decay rate of selected 1:1 (by weight) carbon-sulfur composites at a rate of 0.1C, and tapped density of the gyroidal carbon-sulfur composites with 15 nm mesopores. Tapped density was measured after tapping of the composites 200 times.

| | GaMC-35-1600C | Hex-25-1600 | GdMC-39-1600 | GdMC-39-900 | aGdMC-39-CO2-6h | GdMC-15-1600 | GdMC-15-900 | aGdMC-15-CO2-6h | aGdMC-15-CO2-10h |
|---|---------------|-------------|--------------|-------------|-----------------|--------------|-------------|-----------------|------------------|
| Capacity decrease between 1st and 3rd cycle | 22% | 6% | 34% | 30% | 22% | 26% | 22% | 24% | 32% |
| Average capacity decrease per cycle between 3rd and 100th | 0.74% | 0.70% | 0.49% | 0.35% | 0.39% | 0.64% | 0.41% | 0.32% | 0.33% |
| Tapped density / g/cm ³ | | | | | | 0.6 | 0.6 | | 0.2 |

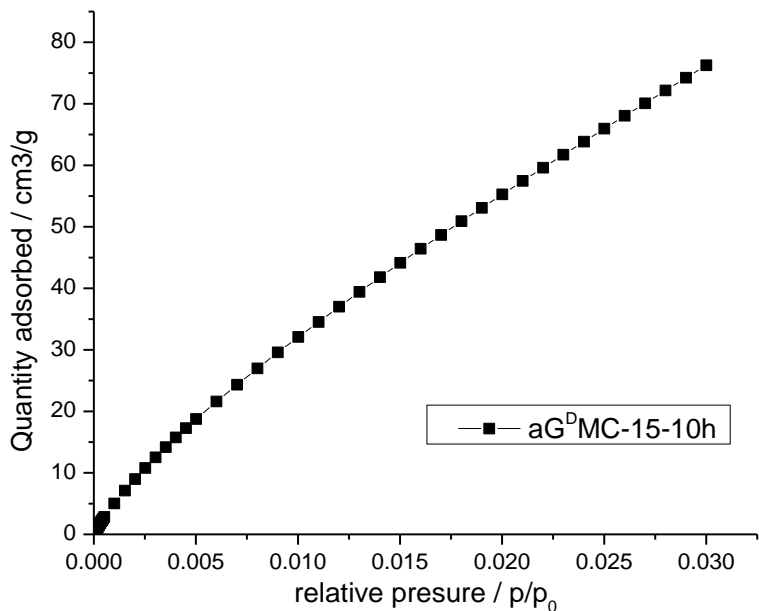


Figure S3.3. Carbon dioxide adsorption isotherm of the gyroidal mesoporous carbon with 15 nm pore size after CO₂-activation for 10 hours at 950 °C (aG^DMC-15-10h).

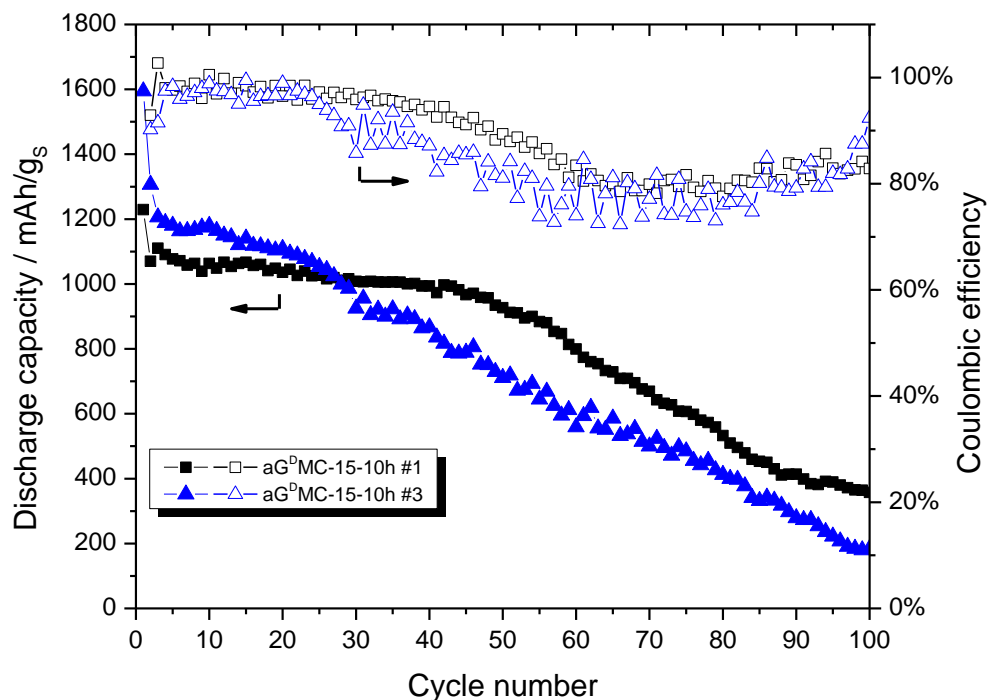


Figure S3.4. Discharge capacities and coulombic efficiencies of first 100 cycles at 0.1C of two separately prepared 1:1 carbon-sulfur composites from aG^DMC-15-10h. Solid symbols correspond to the discharge capacities, open symbols to the coulombic efficiencies.

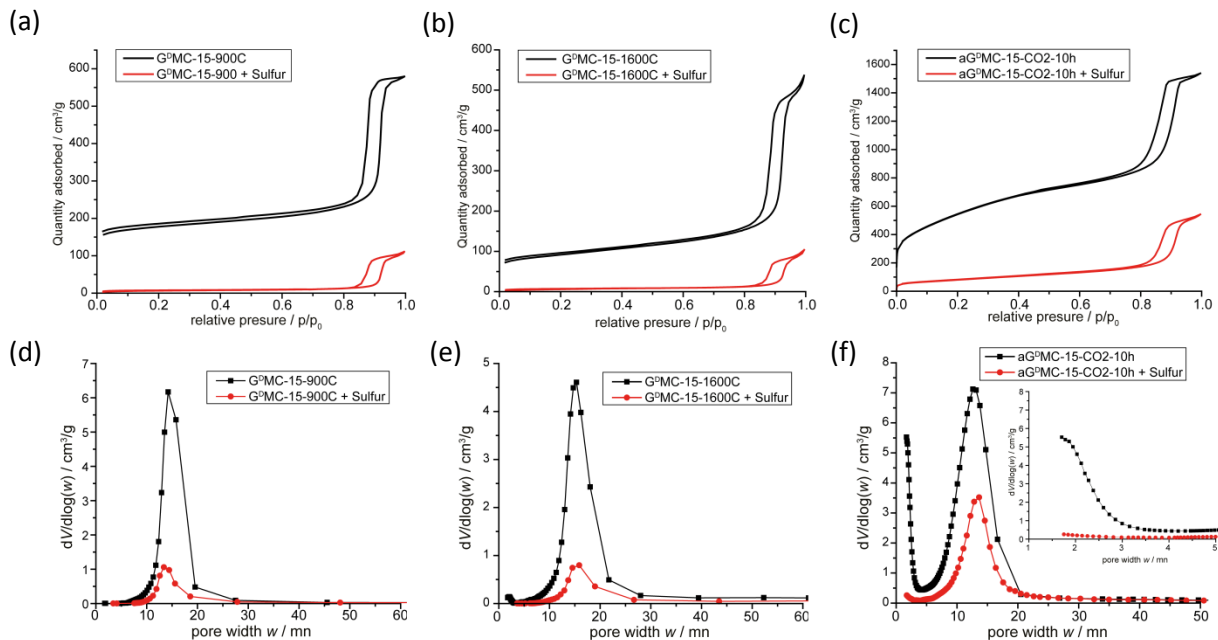


Figure S3.5. Nitrogen sorption isotherms and BJH pore size distributions of gyroidal carbon hosts with (red) and without (black) infiltrated sulfur (1:1 by weight) of G^DMC-15-900°C (a, d), G^DMC-15-1600°C (b, e), and aG^DMC-15-CO₂-10h (c, f). The BET surface areas of G^DMC-15-900°C, G^DMC-15-1600°C, and aG^DMC-15-CO₂-10h infiltrated with an equal amount of sulfur are 27, 26, and 291 m² g⁻¹, respectively, with mesopore volumes of 0.17, 0.15, and 0.83 cm³ g⁻¹ (calculated at a relative pressure of 0.99), respectively. The data confirms that the sulfur fills up most of the mesoporosity in the non-activated carbon hosts (900 °C and 1600 °C), while the small nanopores below 4 nm are filled in the highly activated gyroidal mesoporous carbon host (aG^DMC-15-CO₂-10h) and the larger 15 nm mesopores are still porous after sulfur infiltration.

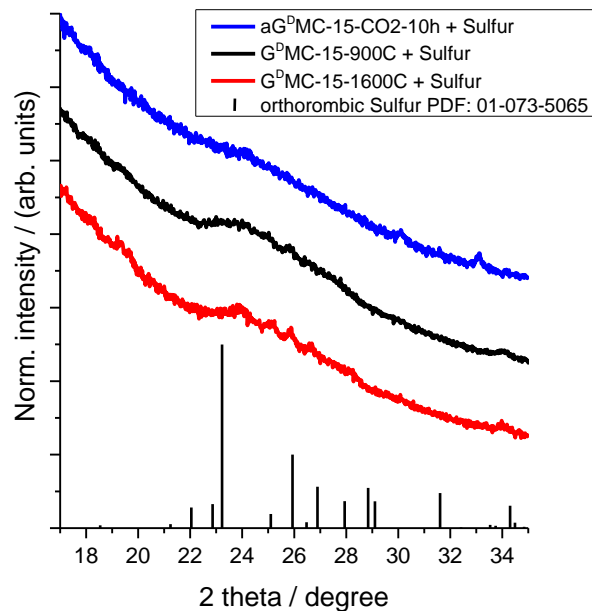


Figure S3.6. Powder X-ray diffraction (PXRD) patterns of gyroidal mesoporous carbon filled with sulfur at 155 °C (1:1 by weight): G^DMC-15-1600°C (red), G^DMC-15-900°C (black), and aG^DMC-15-CO₂-10h (blue). A broad signal between 22 and 29 degrees was obtained for the non-activated carbon hosts (carbonized at 900 °C and 1600 °C). The main peaks of orthorhombic sulfur are in this range. However, from the data, it was determined that the sulfur is amorphous in all carbon hosts.

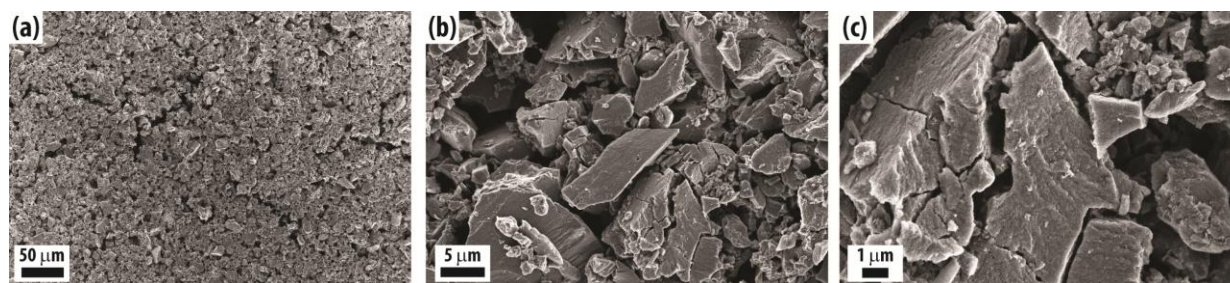


Figure S3.7. Scanning electron microscopy images at different magnifications of an electrode casted from aG^DMC-15-CO₂-10h infiltrated with Sulfur (1:1 by weight) with 10 wt% PVDF binder. Powder particles of the carbon hosts are between 100s of nanometers and 10s of microns in size.

REFERENCES

- (1) Divya, K. C.; Østergaard, J. Battery Energy Storage Technology for Power systems—An Overview. *Electr. Power Syst. Res.* **2009**, *79*, 511–520.
- (2) Zhou, W.; Lou, C.; Li, Z.; Lu, L.; Yang, H. Current Status of Research on Optimum Sizing of Stand-Alone Hybrid Solar–wind Power Generation Systems. *Appl. Energy* **2010**, *87*, 380–389.
- (3) Armand, M.; Tarascon, J.-M. Building Better Batteries. *Nature* **2008**, *451*, 652–657.
- (4) Tarascon, J. M.; Armand, M. Issues and Challenges Facing Rechargeable Lithium Batteries. *Nature* **2001**, *414*, 359–367.
- (5) Dunn, B.; Kamath, H.; Tarascon, J.-M. Electrical Energy Storage for the Grid: A Battery of Choices. *Science* **2011**, *334*, 928–935.
- (6) Lukic, S. M.; Bansal, R. C.; Rodriguez, F.; Emadi, A. Energy Storage Systems for Automotive Applications. *IEEE Trans. Ind. Electron.* **2008**, *55*, 2258–2267.
- (7) Kolosnitsyn, V. S.; Karaseva, E. V. Lithium-Sulfur Batteries: Problems and Solutions. *Russ. J. Electrochem.* **2008**, *44*, 506–509.
- (8) Larcher, D.; Tarascon, J.-M. Towards Greener and More Sustainable Batteries for Electrical Energy Storage. *Nat. Chem.* **2014**, *7*, 19–29.
- (9) Etacheri, V.; Marom, R.; Elazari, R.; Salitra, G.; Aurbach, D. Challenges in the Development of Advanced Li-Ion Batteries: A Review. *Energy Environ. Sci.* **2011**, *4*, 3243–3262.
- (10) Lowe, M. a.; Gao, J.; Abruña, H. D. Mechanistic Insights into Operational Lithium–sulfur Batteries by in Situ X-Ray Diffraction and Absorption Spectroscopy. *RSC Adv.* **2014**, *4*, 18347.
- (11) Cuisinier, M.; Cabelguen, P.-E.; Evers, S.; He, G.; Kolbeck, M.; Garsuch, A.; Bolin, T.; Balasubramanian, M.; Nazar, L. F. Sulfur Speciation in Li–S Batteries Determined by Operando X-Ray Absorption Spectroscopy. *J. Phys. Chem. Lett.* **2013**, *4*, 3227–3232.
- (12) Zhang, S. S.; Read, J. A. A New Direction for the Performance Improvement of Rechargeable Lithium/sulfur Batteries. *J. Power Sources* **2012**, *200*, 77–82.

- (13) Liang, X.; Wen, Z.; Liu, Y.; Wu, M.; Jin, J.; Zhang, H.; Wu, X. Improved Cycling Performances of Lithium Sulfur Batteries with LiNO₃-Modified Electrolyte. *J. Power Sources* **2011**, *196*, 9839–9843.
- (14) Ji, X.; Lee, K. T.; Nazar, L. F. A Highly Ordered Nanostructured Carbon-Sulphur Cathode for Lithium-Sulphur Batteries. *Nat. Mater.* **2009**, *8*, 500–506.
- (15) Jayaprakash, N.; Shen, J.; Moganty, S. S.; Corona, a.; Archer, L. a. Porous Hollow Carbon@sulfur Composites for High-Power Lithium-Sulfur Batteries. *Angew. Chem. Int. Ed. Engl.* **2011**, *50*, 5904–5908.
- (16) Tachikawa, N.; Yamauchi, K.; Takashima, E.; Park, J.-W.; Dokko, K.; Watanabe, M. Reversibility of Electrochemical Reactions of Sulfur Supported on Inverse Opal Carbon in Glyme-Li Salt Molten Complex Electrolytes. *Chem. Commun. (Camb)*. **2011**, *47*, 8157–8159.
- (17) Liang, C.; Dudney, N. J.; Howe, J. Y. Hierarchically Structured Sulfur/Carbon Nanocomposite Material for High-Energy Lithium Battery. *Chem. Mater.* **2009**, *21*, 4724–4730.
- (18) Demir-Cakan, R.; Morcrette, M.; Nouar, F.; Davoisne, C.; Devic, T.; Gonbeau, D.; Dominko, R.; Serre, C.; Férey, G.; Tarascon, J.-M. Cathode Composites for Li-S Batteries via the Use of Oxygenated Porous Architectures. *J. Am. Chem. Soc.* **2011**, *133*, 16154–16160.
- (19) Zheng, G.; Yang, Y.; Cha, J. J.; Hong, S. S.; Cui, Y. Hollow Carbon Nanofiber-Encapsulated Sulfur Cathodes for High Specific Capacity Rechargeable Lithium Batteries. *Nano Lett.* **2011**, *11*, 4462–4467.
- (20) Liang, X.; Wen, Z.; Liu, Y.; Zhang, H.; Huang, L.; Jin, J. Highly Dispersed Sulfur in Ordered Mesoporous Carbon Sphere as a Composite Cathode for Rechargeable Polymer Li/S Battery. *J. Power Sources* **2011**, *196*, 3655–3658.
- (21) Li, S.; Xie, M.; Liu, J.; Wang, H.; Yan, H. Layer Structured Sulfur/Expanded Graphite Composite as Cathode for Lithium Battery. *Electrochem. Solid-State Lett.* **2011**, *14*, A105.
- (22) Wang, J.-Z.; Lu, L.; Choucair, M.; Stride, J. a.; Xu, X.; Liu, H.-K. Sulfur-Graphene Composite for Rechargeable Lithium Batteries. *J. Power Sources* **2011**, *196*, 7030–7034.
- (23) Schuster, J.; He, G.; Mandlmeier, B.; Yim, T.; Lee, K. T.; Bein, T.; Nazar, L. F. Spherical Ordered Mesoporous Carbon Nanoparticles with High Porosity for Lithium-Sulfur Batteries. *Angew. Chemie - Int. Ed.* **2012**, *51*, 3591–3595.

- (24) He, G.; Ji, X.; Nazar, L. High “C” Rate Li-S Cathodes: Sulfur Imbided Bimodal Porous Carbons. *Energy & Environmental Science*, 2011, 4, 2878–2883.
- (25) Ji, L.; Rao, M.; Aloni, S.; Wang, L.; Cairns, E. J.; Zhang, Y. Porous Carbon Nanofiber–sulfur Composite Electrodes for Lithium/sulfur Cells. *Energy & Environmental Science*, 2011, 4, 5053–5059.
- (26) Elazari, R.; Salitra, G.; Garsuch, A.; Panchenko, A.; Aurbach, D. Sulfur-Impregnated Activated Carbon Fiber Cloth as a Binder-Free Cathode for Rechargeable Li-S Batteries. *Adv. Mater.* **2011**, 23, 5641–5644.
- (27) Wang, D.-W.; Zeng, Q.; Zhou, G.; Yin, L.; Li, F.; Cheng, H.-M.; Gentle, I. R.; Lu, G. Q. M. Carbon-Sulfur Composites for Li-S Batteries: Status and Prospects. *J. Mater. Chem. A* **2013**, 1, 9382–9394.
- (28) Zhou, G.; Wang, D.-W.; Li, F.; Hou, P.-X.; Yin, L.; Liu, C.; Lu, G. Q. (Max); Gentle, I. R.; Cheng, H.-M. A Flexible Nanostructured Sulphur–carbon Nanotube Cathode with High Rate Performance for Li-S Batteries. *Energy & Environmental Science*, 2012, 5, 8901-8906.
- (29) Wei Seh, Z.; Li, W.; Cha, J. J.; Zheng, G.; Yang, Y.; McDowell, M. T.; Hsu, P.-C.; Cui, Y. Sulphur–TiO₂ Yolk–shell Nanoarchitecture with Internal Void Space for Long-Cycle Lithium–sulphur Batteries. *Nat. Commun.* **2013**, 4, 1331.
- (30) Xiao, L.; Cao, Y.; Xiao, J.; Schwenzer, B.; Engelhard, M. H.; Saraf, L. V.; Nie, Z.; Exarhos, G. J.; Liu, J. A Soft Approach to Encapsulate Sulfur: Polyaniline Nanotubes for Lithium-Sulfur Batteries with Long Cycle Life. *Adv. Mater.* **2012**, 24, 1176–1181.
- (31) Ji, X.; Evers, S.; Black, R.; Nazar, L. F. Stabilizing Lithium-Sulphur Cathodes Using Polysulphide Reservoirs. *Nat. Commun.* **2011**, 2, 325.
- (32) Song, J.; Xu, T.; Gordin, M. L.; Zhu, P.; Lv, D.; Jiang, Y. B.; Chen, Y.; Duan, Y.; Wang, D. Nitrogen-Doped Mesoporous Carbon Promoted Chemical Adsorption of Sulfur and Fabrication of High-Areal-Capacity Sulfur Cathode with Exceptional Cycling Stability for Lithium-Sulfur Batteries. *Adv. Funct. Mater.* **2014**, 24, 1243–1250.
- (33) Yang, C. P.; Yin, Y. X.; Ye, H.; Jiang, K. C.; Zhang, J.; Guo, Y. G. Insight into the Effect of Boron Doping on Sulfur/carbon Cathode in Lithium-Sulfur Batteries. *ACS Appl. Mater. Interfaces* **2014**, 6, 8789–8795.
- (34) Xu, R.; Belharouak, I.; Li, J. C. M.; Zhang, X.; Bloom, I.; Bareño, J. Role of Polysulfides in Self-Healing Lithium-Sulfur Batteries. *Adv. Energy Mater.* **2013**, 3, 833–838.

- (35) Lin, Z.; Liang, C. Lithium-Sulfur Batteries: From Liquid to Solid Cells. *J. Mater. Chem. A* **2014**, *00*, 1–23.
- (36) Wang, H.; Yang, Y.; Liang, Y.; Robinson, J. T.; Li, Y.; Jackson, A.; Cui, Y.; Dai, H. Graphene-Wrapped Sulfur Particles as a Rechargeable Lithium-Sulfur Battery Cathode Material with High Capacity and Cycling Stability. *Nano Lett.* **2011**, *11*, 2644–2647.
- (37) Evers, S.; Nazar, L. F. Graphene-Enveloped Sulfur in a One Pot Reaction: A Cathode with Good Coulombic Efficiency and High Practical Sulfur Content. *Chem. Commun. (Camb)*. **2012**, *48*, 1233–1235.
- (38) Zhao, M.-Q.; Zhang, Q.; Huang, J.-Q.; Tian, G.-L.; Nie, J.-Q.; Peng, H.-J.; Wei, F. Unstacked Double-Layer Templated Graphene for High-Rate Lithium-Sulphur Batteries. *Nat. Commun.* **2014**, *5*, 3410.
- (39) Thieme, S.; Brückner, J.; Bauer, I.; Oschatz, M.; Borchardt, L.; Althues, H.; Kaskel, S. High Capacity Micro-Mesoporous Carbon-sulfur Nanocomposite Cathodes with Enhanced Cycling Stability Prepared by a Solvent-Free Procedure. *J. Mater. Chem. A* **2013**, *1*, 9225.
- (40) Hoffmann, C.; Thieme, S.; Brückner, J.; Oschatz, M.; Biemelt, T.; Mondin, G.; Althues, H.; Kaskel, S. Nanocasting Hierarchical Carbide-Derived Carbons in Nanostructured Opal Assemblies for High-Performance Cathodes in Lithium-Sulfur Batteries. *ACS Nano* **2014**, *8*, 12130–12140.
- (41) Thieme, S.; Brückner, J.; Meier, A.; Bauer, I.; Gruber, K.; Kaspar, J.; Helmer, A.; Althues, H.; Schmuck, M.; Kaskel, S. A Lithium-sulfur Full Cell with Ultralong Cycle Life: Influence of Cathode Structure and Polysulfide Additive. *J. Mater. Chem. A* **2015**, *3*, 3808–3820.
- (42) Xin, S.; Gu, L.; Zhao, N.-H.; Yin, Y.-X.; Zhou, L.-J.; Guo, Y.-G.; Wan, L.-J. Smaller Sulfur Molecules Promise Better Lithium-Sulfur Batteries. *J. Am. Chem. Soc.* **2012**, *134*, 18510–18513.
- (43) Li, Z.; Jiang, Y.; Yuan, L.; Yi, Z.; Wu, C.; Liu, Y.; Strasser, P.; Huang, Y. A Highly Ordered Meso@microporous Carbon-Supported Sulfur@smaller Sulfur Core-Shell Structured Cathode for Li-S Batteries. *ACS Nano* **2014**, *8*, 9295–9303.
- (44) Xu, T.; Song, J.; Gordin, M. L.; Sohn, H.; Yu, Z.; Chen, S.; Wang, D. Mesoporous Carbon-Carbon Nanotube-Sulfur Composite Microspheres for High-Areal-Capacity Lithium-Sulfur Battery Cathodes. *ACS Appl. Mater. Interfaces* **2013**, *5*, 11355–11362.
- (45) Sohn, H.; Gordin, M. L.; Xu, T.; Chen, S.; Lv, D.; Song, J.; Manivannan, A.; Wang, D. Porous Spherical Carbon/sulfur Nanocomposites by Aerosol-Assisted Synthesis: The Effect of Pore Structure and Morphology on Their Electrochemical Performance as Lithium/sulfur Battery Cathodes. *ACS Appl. Mater. Interfaces* **2014**, *6*, 7596–7606.

- (46) Werner, J. G.; Hoheisel, T. N.; Wiesner, U. Synthesis and Characterization of Gyroidal Mesoporous Carbons and Carbon Monoliths with Tunable Ultralarge Pore Size. *ACS Nano* **2014**, *8*, 731–743.
- (47) Harry Marsh, Francisco Rodríguez Reinoso, *Activated Carbon*, Elsevier, Oxford, 2006, Ch. 5, Pp. 274-289.; Vol. 2.
- (48) Gao, J.; Lowe, M. A.; Kiya, Y.; Abruña, H. D. Effects of Liquid Electrolytes on the Charge-Discharge Performance of Rechargeable Lithium/sulfur Batteries: Electrochemical and in-Situ X-Ray Absorption Spectroscopic Studies. *J. Phys. Chem. C* **2011**, *115*, 25132–25137.
- (49) Cuisinier, M.; Hart, C.; Balasubramanian, M.; Garsuch, A.; Nazar, L. F. Radical or Not Radical : Revisiting Lithium – Sulfur Electrochemistry in Nonaqueous Electrolytes. *Adv. Energy Mater.* **2015**, DOI:10.1002/aenm.201401801.
- (50) Bailey, T. S.; Hardy, C. M.; Epps, T. H.; Bates, F. S. A Noncubic Triply Periodic Network Morphology in Poly(isoprene-B-Styrene-B-Ethylene Oxide) Triblock Copolymers. *Macromolecules* **2002**, *35*, 7007–7017.
- (51) Meng, Y.; Gu, D.; Zhang, F.; Shi, Y.; Cheng, L.; Feng, D.; Wu, Z.; Chen, Z.; Wan, Y.; Stein, A.; *et al.* A Family of Highly Ordered Mesoporous Polymer Resin and Carbon Structures from Organic–Organic Self-Assembly. *Chem. Mater.* **2006**, *18*, 4447–4464.
- (52) Brunauer, S.; Emmett, P. H.; Teller, E. Adsorption of Gases in Multimolecular Layers. *J. Am. Chem. Soc.* **1938**, *60*, 309–319.
- (53) Barrett, E. P.; Joyner, L. G.; Halenda, P. P. The Determination of Pore Volume and Area Distributions in Porous Substances. I. Computations from Nitrogen Isotherms. *J. Am. Chem. Soc.* **1951**, *73*, 373–380.
- (54) Tarazona, P. Free-Energy Density Functional for Hard Spheres. *Phys. Rev. A* **1985**, *31*, 2672–2679.
- (55) Tarazona, P.; Marconi, U. M. B.; Evans, R. Phase Equilibria of Fluid Interfaces and Confined Fluids. *Mol. Phys.* **1987**, *60*, 573–595.

CHAPTER 4

GYROIDAL MESOPOROUS MULTIFUNCTIONAL NANOCOMPOSITES

VIA ATOMIC LAYER DEPOSITION

Abstract

We demonstrate the preparation of rationally designed, multifunctional, monolithic and periodically ordered mesoporous core-shell nanocomposites with tunable structural characteristics. Three-dimensionally (3D) co-continuous gyroidal mesoporous polymer monoliths are fabricated from solution-based triblock terpolymer-resols co-assembly and used as the functional templates for the fabrication of free-standing core-shell carbon-titania composites using atomic layer deposition (ALD). The deposition depth into the torturous gyroidal nanonetwork is investigated as a function of ALD conditions and the resulting composites are submitted to different thermal treatments. Results suggest that ALD can homogeneously coat mesoporous templates with well defined pore sizes below 50 nm and thicknesses above 10 μm . Structural tunability like titania shell thickness and pore size control is demonstrated. The ordered nanocomposites exhibit triple functionality; a 3D continuous conductive carbon core that is coated with a crystalline titania shell that in turn is in contact with a 3D continuous mesopore network in a compact monolithic architecture. This materials design is of interest for applications including energy conversion and storage. Gyroidal mesoporous titania monoliths can be obtained through simultaneous titania crystallization and template removal in air.

Adapted from Werner, J. G., Scherer, M. R. J., Steiner, U., Wiesner, U.: Gyroidal Mesoporous Multifunctional Nanocomposites via Atomic Layer Deposition, *Nanoscale* **6**, 8736-8742 (2014) with permission from The Royal Society of Chemistry.

Introduction

Battery electrode materials suffer from insufficient power densities due to slow solid state diffusion of ions in the active material, poor accessibility of electrolyte to the active material, and low electrical conductivity.¹⁻³ Nanomaterials, such as nanoparticles, have been successfully applied to increase the rate capability by decreasing the solid state ion diffusion length.⁴⁻⁶ Additionally, nanocomposites of electrochemically active and electronically conductive materials have been shown to further decrease capacity losses at high-rate operations of electrodes in energy storage systems due to increased conductivity.^{7,8} However, in many architectures, the active and conductive materials are still separated on the macroscale or the composite electrodes exhibit large free volumes with low effective electrode densities that yield low volumetric energy densities.^{9,10} In this work, we demonstrate the fabrication of rationally designed, free-standing ordered mesoporous core-shell nanocomposites with a double gyroid morphology and tunable structural characteristics. The double gyroid is a cubic, bicontinuous structure that can be described by Schoen's G surface, a triply periodic minimal surface that divides room into two equally sized volumes without self-intersections.¹¹ Nature adapts the single gyroid structure in butterfly wings, similarly artificial block copolymers can self-assemble into gyroidal morphologies.¹² The porous three-dimensionally (3D) continuous gyroidal matrix used here represents the gyroidal surface with finite thickness and separates two interpenetrating 3D continuous networks of pores that are enantiomeric to each other. These porous networks consist of triple nodes that are connected by struts (top left of Scheme 4.1; majority 3D gyroidal matrix in black and two minority 3D continuous pore networks in yellow).^{11,12} Flexible gyroidal mesoporous polymeric monoliths with ultralarge pore sizes and large footprint areas were used as functional or sacrificial templates for the fabrication of free-standing micrometer thick core-shell polymer-metal oxide composites or ordered mesoporous titania monoliths, respectively, using atomic layer deposition (ALD) followed by different heat treatments. This deposition technique is widely used in the electronics industry and well studied for flat substrate applications.¹³ The self-limiting nature of the deposition process makes ALD an ideal technique for the controlled deposition of conformal thin films with thicknesses of a few nanometers. Despite recent efforts on nanomaterials as substrates for

ALD, only a limited amount of work has been performed on purely mesoporous templates.¹⁴⁻¹⁸ Only macroporous (pore sizes > 50 nm) substrates e.g. from carbon nanotubes or gold have been demonstrated to result in an ALD penetration depth above 10 μm .^{10,19} The use of a functional mesoporous template with pore sizes less than 50 nm and thicknesses above 10 μm as the substrate for another functional material that is deposited using ALD with retention of mesoporosity, to the best of our knowledge, has not been reported to date.

Monolithic mesoporous template films with thickness dimensions of tens of microns, and pore sizes in the nanometer range, are expected to significantly hinder the diffusion of the ALD precursor gases throughout the template. This leads to limitations in the applicability of ALD towards free-standing monolithic mesoporous nanocomposites. In order to quantitatively assess what these limitations are, and thereby the potential of ALD to generate homogeneous multifunctional nanomaterials with applications in energy conversion and storage, we investigated the deposition depth of an ALD oxide coating into a torturous gyroidal porous polymer resin with nanoscopic pore dimensions as a function of the ALD conditions. The ultralarge mesopore size (up to ~40 nm) of the template allows for the tunable deposition of more than 10 nm of functional metal oxide coating onto the resin-type substrate while retaining accessibility *via* sufficiently large (~20 nm) and ordered 3D interconnected mesopores. The composites were subsequently converted into ordered multifunctional nanocomposites *via* heat treatment. The resulting materials exhibit a rationally designed nano-architecture with a conductive carbon core that is coated with an electrochemically active, crystalline functional material such as titania, which in turn is in contact with a 3D continuous mesopore network. This triple functionality of a conductive core, an active shell and mesoporosity in a compact monolithic architecture of a periodic nanomaterial is expected to be of interest for applications in energy conversion and storage.

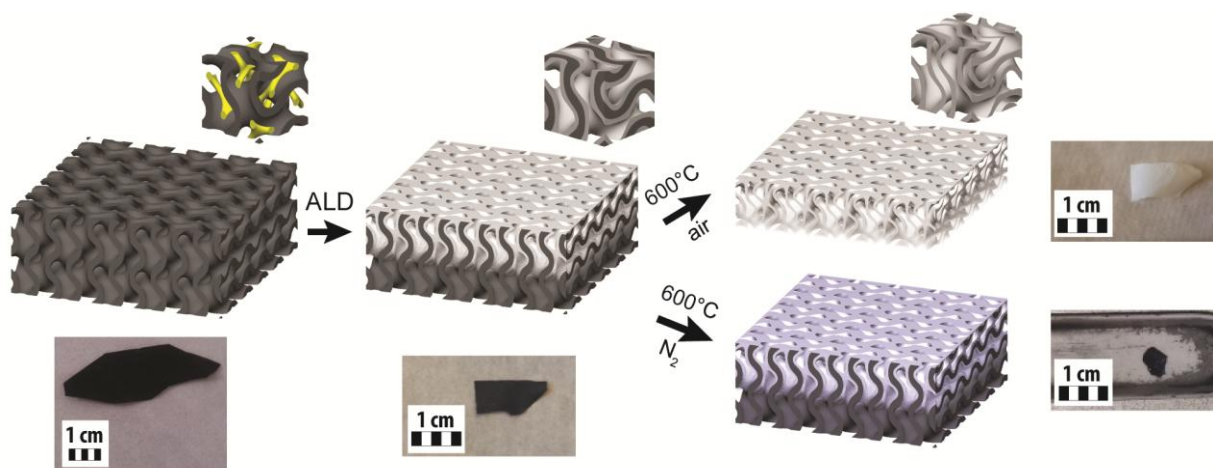
Results and Discussion

The fabrication of free-standing core-shell resin-titania composites and their conversion into ordered multifunctional composites is illustrated in Scheme 4.1. First, free-standing ordered organic-organic hybrid films with gyroidal morphology were fabricated using the structure direction of phenol-

formaldehyde resols with the triblock terpolymer poly(isoprene)-*block*-poly(styrene)-*block*-poly(ethylene oxide) (ISO) as described in an earlier study.²⁰ ISO had a large molar mass of 130 kDa and low polydispersity index of 1.09. For an in-depth structural characterization of the gyroidal monoliths using a combination of small-angle X-ray scattering (SAXS) and transmission and scanning electron microscopy (TEM/SEM), the interested reader is referred to reference 20. Plasma etching and subsequent pyrolysis of the organic–organic hybrids under inert atmosphere at 450 °C yielded flexible gyroidal mesoporous resin templates with pore sizes of 40 nm, thicknesses of 50–80 μm and a large footprint area of more than 1 cm² (Scheme 4.1 and Figure S4.1). Due to the low pyrolysis temperature and high oxygen content of the precursor, it can safely be assumed that the surface of the polymeric template is covered with oxygen containing functional groups. The monolithic gyroidal mesoporous resins were used as a nanostructured template for the atomic layer deposition (ALD) of titanium dioxide with 250 cycles (unless otherwise noted) at 150 °C using TiCl₄ and water as precursors. Four different protocols were tested in order to investigate the deposition depth and conformity as a function of the deposition conditions as summarized in Table 4.1 and described in the experimental section. The thickness of the template was intentionally chosen to be larger than the expected penetration depth for the ALD process for such torturous nanoporous networks in order to investigate the maximum deposition depth into the template.

Table 4.1. Summary of the ALD conditions employed for the formation of ordered mesoporous multifunctional multicomponent titania nanocomposites.

| Sample | Cycles | Type | TiCl ₄ -Pulse time / s | H ₂ O-Pulse time / s | Soaking Time / s |
|---------------------------------|--------|--------------|-----------------------------------|---------------------------------|------------------|
| TiO ₂ /C-0.4s | 250 | Flow over | 0.4 | 0.4 | - |
| TiO ₂ /C-1s-soak | 250 | Flow over | 1 | 0.025 | 6 |
| TiO ₂ /C-0.4s-direct | 250 | Flow through | 0.4 | 0.4 | - |
| TiO ₂ /C-1s-direct | 250 | Flow through | 1 | 1 | - |
| TiO ₂ /C-1s-dir-125 | 125 | Flow through | 1 | 1 | - |



Scheme 4.1. Illustration of the process employed for the formation of periodically ordered gyroidal mesoporous multifunctional titania nanocomposites, together with photographs of the resulting materials and gyroidal models illustrating the respective structures. From left to right: Monolithic 3D continuous gyroidal mesoporous resin; monolithic 3D continuous gyroidal mesoporous core-shell polymer-titania composite after atomic layer deposition (ALD) of amorphous titania exhibiting decreased deposition thickness away from the top surface; monolithic 3D continuous gyroidal mesoporous crystalline anatase titania (top) and monolithic 3D continuous gyroidal mesoporous core-shell carbon-titania composite (bottom) after heat-treatment at 600 °C in air or inert atmosphere, respectively. The insets show double gyroidal unit cells of the respective structures with indication of the 3D pore (yellow; left) and titania (white; middle and right) connectivity.

Two protocols used standard ALD sample positioning in the reactor with the precursor gases pulsed for 0.4 and 1 second, respectively, flowing over the template (see Figure S4.1). Only one of these protocols included a six second soaking time after the precursor gas pulse before the reactor was purged to allow for more efficient diffusion into the template. The resulting samples are referred to as TiO₂/C-0.4s and TiO₂/C-1s-soak. For the two other protocols, the templates were directly placed on top of the gas inlet of the reactor in order to direct the flow of precursor gases toward the porous template (see Figure S4.1). Only the influence of pulse time was investigated for this directed flow method. The resulting samples are referred to as TiO₂/C-0.4s-direct and TiO₂/C-1s-direct. The ALD template employed here has multiple advantages over commonly used ones: The polymeric resin withstands temperatures well above 100 °C. Such temperatures are typically used for ALD processes, but are inaccessible with normal polymeric templates due to low glass transition temperatures. The template can also be easily burned off in air. In contrast inorganic templates that are commonly used for higher temperature ALD syntheses of

nanostructures have to be etched out in tedious post-synthesis steps. A disadvantage over regular polymeric templates is that as a result of cross-linking the template used here cannot be removed by dissolution.

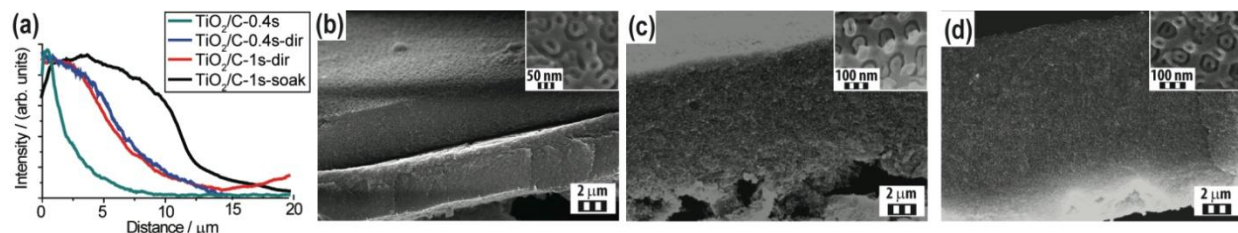


Figure 4.1. (a) Titania EDX line scans from the surface of the as-made polymer-titania composites with 250 deposition cycles. Cross-section SEM images of TiO₂/C-0.4s (b), TiO₂/C-1s-direct (c), and TiO₂/C-1s-soak (d) after removal of the polymeric template by heat treatment. These images directly visualize the increase of ALD depth with increasing pulse and soaking time. Insets depict SEM images of the titania shell structure at higher magnification. Note that in (b) the titania films resulting from both surfaces after removal of the polymer template are collapsed onto each other, whereas in (c) and (d) only one of these films is shown.

Figure 4.1a shows energy-dispersive X-ray spectroscopy (EDX) line-scans of the titanium K-edge from the top surface of freshly cleaved cross-sections of the monolithic carbon-titania nanocomposites. It is noteworthy that the resolution of EDX in a scanning electron microscope (SEM) is on the order of one micrometer. Therefore, the results from this analysis method are only qualitative. It is evident from the data presented in Figure 4.1a, however, that both directed flow of the precursor gases as well as soaking after each precursor pulse significantly increase the deposition depth. The titanium signal for TiO₂/C-0.4s decreased with increasing distance from the surface and reached less than 15% of the surface signal intensity after 5 μm. The sample with the same pulse time but directed flow of the precursor gases, TiO₂/C-0.4s-direct, showed a constant titanium signal for the first 4 μm from the top surface, after which it decreased to 15% of the plateau intensity at a depth of 10 μm. Interestingly, the pulse time did not show a distinguishable difference for the directed flow method, as is evident from the overlaying titanium line-scans for TiO₂/C-0.4s-direct and TiO₂/C-1s-direct. The line-scan for the sample with soaking time, TiO₂/C-1s-soak, evidenced the best result. It showed a relatively constant titanium signal for the first 10 μm from the template surface that rapidly decreased to less than 15% of its plateau value at a distance of 14.5 μm from the surface.

The maximum penetration depth of the processes was also investigated using SEM analysis of freshly cleaved edges of the titania composites after heat treatment to remove the polymer template. The thickness of the remaining titania film after removal of the polymeric membrane can be used to estimate the maximum penetration depth of the ALD process under the respective conditions. The cross-sections of TiO₂/C-0.4s, TiO₂/C-1s-direct and TiO₂/C-1s-soak after polymer removal are shown in Figure 4.1b–d, and exhibit a thickness of 4.5, 9 and 12.5 μm, respectively, thereby directly visualizing the increase of ALD depth with increasing pulse and soaking time. These results corroborate that the precursor gas diffusion is significantly hindered by the torturous porosity with nanometer sized pores, but that increased exposure of the nanoporous template to the reactive gases by either directed flow or soaking of the template in the gas atmosphere can substantially increase the deposition depth.

The deposition conformity and thickness was further investigated using high-resolution SEM on TiO₂/C-1s-soak, the sample with the highest deposition depth (Figure 4.2).²¹ For reference, Figure 4.2a shows a SEM image of the characteristic (211) gyroidal projection of the porous template before deposition together with a simulation of this projection in the inset. Figure 4.2b and 4.2c display high-resolution SEM images of the nanocomposite after heat treatment at 600 °C in inert atmosphere at distances of 1 μm and 6.5 μm from the surface, respectively. The layer thickness of the titania "tubes" is approximately 13 nm for both distances from the surface. For comparison the inset of Figure 4.2b depicts a simulation of a projection along the [110] zone axis of the gyroid shell, consistent with the images displayed in Figure 4.2b–f. Calcination of the polymer-titania composite in air lead to removal of the polymer template and the formation of a free-standing ordered titania monolith (upper right in Scheme 4.1). The variation of the titania shell thickness can be better evaluated after such template removal. The titania phase, constituting the shell of the two interpenetrating 3D continuous gyroidal pore networks, did not collapse during the calcination. Figure 4.2d–f show SEM images of the calcined titania monolith at the top surface, and at distances of 5 μm and 10 μm away from the surface, respectively. While the titania layer thickness appears similar at the top and at 5 μm, it is significantly decreased to approximately 5 nm

at a distance of 10 μm from the top (Figure 4.2f), as is particularly evident from the insets showing larger magnification images.

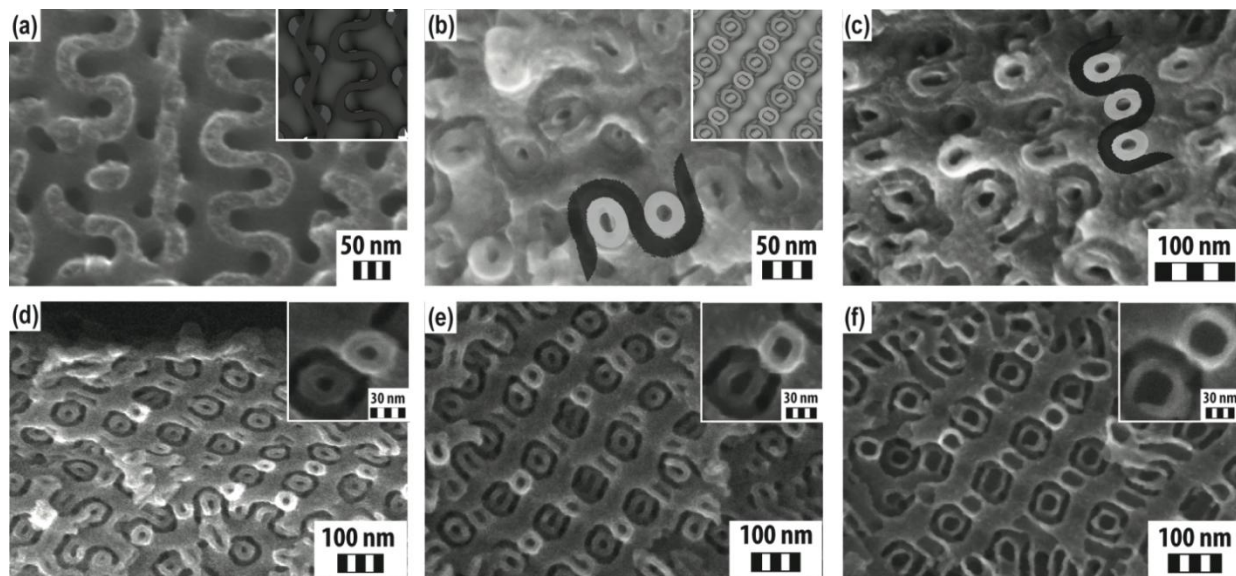


Figure 4.2. SEM images of the double gyroidal mesoporous polymer template (a), TiO_2/C -1s-soak after pyrolysis at 600 $^\circ\text{C}$ under nitrogen at distances of 1 μm (b) and 6.5 μm (c) from the surface, and after calcination at 600 $^\circ\text{C}$ in air at the surface (d), as well as at 5 μm (e) and 10 μm (f) from the surface, showing a homogeneous titania layer thickness over the first ~ 7 μm from the template surface. Insets in (a) and (b) show SEM simulations of the double gyroid matrix (211) plane (a) and the double gyroid shell along the [110] zone axis (b). Overlays in (b) and (c) are guides for the eye for a clear identification of the carbon (black) and titania (grey) phases. Insets in (d-f) show parts of the respective SEM images at higher magnification facilitating direct titania layer thickness comparison.

Images and data on display in Figures 2 and 3 reveal the multifunctionality of the materials as illustrated in Scheme 4.1. Since the polymeric template can either be converted into carbon *via* heat treatment at or above 600 $^\circ\text{C}$ in inert atmosphere, or can be burned out at 450 $^\circ\text{C}$ in air, two types of multifunctional nanocomposites can be obtained after the ALD process. When heated at 600 $^\circ\text{C}$ under nitrogen, the phenolic resin is converted into carbon while the titania shell crystallizes. During this process, mesostructure and mesoporosity are retained as is evident from the images. No change of the shape of the titania phase, collapse of the pores, or disconnection of the titania from the carbon core could be observed by SEM, see Figure 4.2b and 4.2c. The formation of the carbon core and the crystalline titania shell was corroborated by Raman spectroscopy and X-ray diffraction analysis (XRD), respectively, as shown for the samples using the directed gas flow synthesis conditions with different cycle numbers in

Figure 4.3 and 4.4. However, the heat treatment results were similar for all samples, independent of the ALD conditions. Figure 4.3a shows XRD data of TiO₂/C-1s-direct heat treated under different conditions. After pyrolysis at 600 °C in nitrogen (bottom, red trace), the diffraction peaks match the expected reflections for anatase titania (PDF No. 21-1272) with an average crystallite size of 14 nm, approximated using the Scherrer equation for the five main peaks. The crystallite size is on the order of the titania layer thickness, which explains the retention of the periodically ordered core-shell nanostructure. It is important to note that approximation of crystallite size using the Scherrer analysis does not take into account the influence of microstrains on XRD peak broadening. Microstrains are likely in our materials due to titania crystallization on the torturous gyroidal surfaces as well as in confined spaces. When the pyrolysis temperature in nitrogen is raised to 900 °C, the XRD pattern exhibits the same diffraction peaks consistent with anatase titania (top, black trace). Under these higher temperature conditions, however, the crystallite size is increased to 33 nm, which is larger than the titania layer thickness. As revealed in Figure 4.3c this further growth of the crystallites resulted in a disruption of the ordered core-shell structure. Large titania crystals are randomly distributed in the carbon matrix. For comparison, after calcination in air at 600 °C leading to polymer resin removal, the crystallite size obtained from the XRD pattern (middle, blue trace) of the resulting monolithic gyroidal mesoporous titania is 17 nm, slightly larger than under inert atmosphere at that temperature.

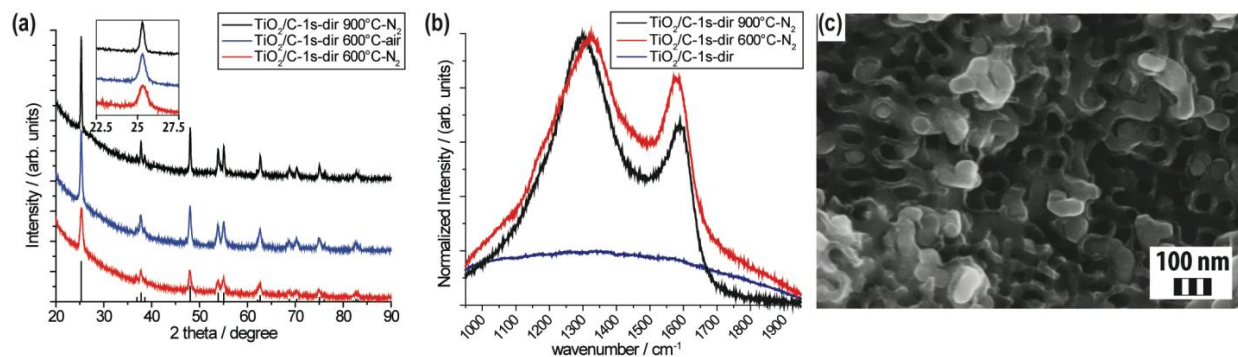


Figure 4.3. (a) XRD patterns of TiO₂/C-1s-direct heat treated under different conditions. (b) Raman spectra of TiO₂/C-1s-direct before (blue) and after pyrolysis in nitrogen at 600 °C (red) or 900 °C (black) showing the evolution of D- and G-bands, typical for disordered carbon materials. (c) SEM image of TiO₂/C-1s-direct after pyrolysis in nitrogen at 900 °C revealing the random growth of titania crystallites in the ordered carbon framework.

Raman spectroscopy shows the appearance of D- and G-bands at 1323 or 1296 cm^{-1} and 1578 or 1590 cm^{-1} after pyrolysis at 600 °C or 900 °C, respectively, with narrowing of the bands with higher temperature (Figure 4.3b).^{22,23} These bands are indicative for disordered carbon material. The Raman, XRD and SEM data together corroborate the formation of ordered core-shell carbon-titania composites after pyrolysis in nitrogen at 600 °C. However, when heat treated in nitrogen at 900 °C, the growth of the titania crystals disrupts the ordered shell structure while the ordered carbon matrix is retained. There is no indication of rutile formation in the XRD data. As previously reported, crystalline titania nanomaterials only form the thermodynamically more stable rutile crystal structure above a critical crystallite size, due to the higher surface energy of the rutile phase.^{24,25} Interestingly, the crystallite size of over 30 nm observed here for the anatase phase at 900 °C is more than twice as big as previously assumed to be thermodynamically stable from kinetic experiments.²⁵ We speculate that the rigid carbon support matrix plays a role in the prevention of the anatase-to-rutile phase transformation even at temperatures as high as 900 °C.

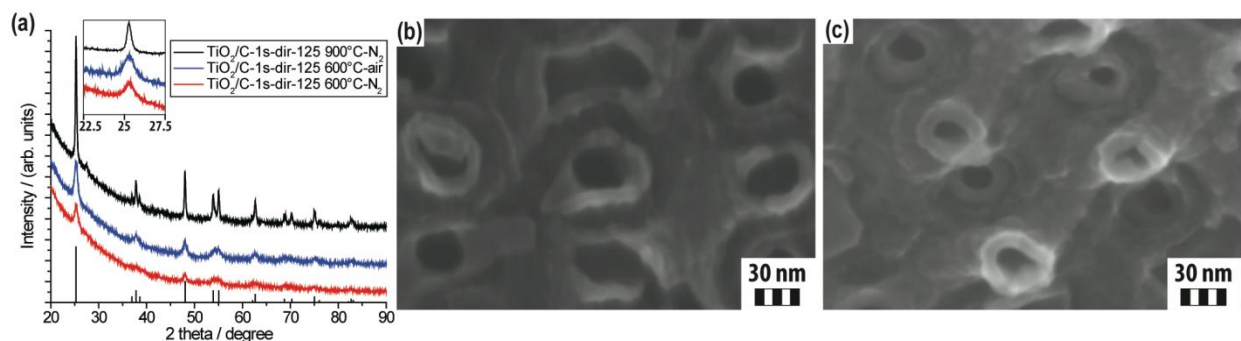


Figure 4.4. (a) XRD patterns of $\text{TiO}_2/\text{C-1s-direct-125}$ heat-treated under different conditions. SEM images of $\text{TiO}_2/\text{C-1s-direct-125}$ (b) and $\text{TiO}_2/\text{C-1s-direct}$ (c) close to the top surface after pyrolysis at 600 °C in nitrogen showing the titania layer thickness dependence on the ALD cycle number.

The titania deposition thickness on flat substrates can be controlled by the number of ALD cycles. We explored ALD thickness control in our 3D continuous gyroidal nanostructured templates for a depth from the surface of uniform deposition thickness using the directed flow method by reducing the cycle number from 250 to 125. Figure 4.4a and 4.4b show XRD patterns and a SEM image, respectively, of $\text{TiO}_2/\text{C-1s-direct-125}$ pyrolyzed at 600 °C in nitrogen. From SEM image analysis, the titania deposition thickness is

measured to be 9 nm, similar to the Scherrer crystallite size of 10 nm calculated from the XRD pattern. It is noteworthy that in contrast to flat substrates, the layer thickness dependence on cycle number for the deposition inside the torturous gyroidal nanonetwork is not linear (Figure 4.4b and 4.4c).¹³ This may be due both, to increased curvature as well as decreased accessibility with increasing layer thickness in the mesoporous channels. Tailoring of the titania layer thickness also allows for control of the remaining pore size in the periodically ordered multifunctional core-shell nanocomposites. When pyrolyzed in nitrogen at 900 °C, the crystallite size from the XRD pattern (top, black trace) again increased to 31 nm leading to the disruption of the ordered titania shell structure.

After calcination in air at 600 °C of the as-made TiO₂/C-1s-direct-125, the template is removed with retention of the ordered phase. From the XRD pattern in Figure 4.4a (middle, blue trace), the crystallite size is calculated to be 10 nm for the ordered mesoporous titania monolith from 125 ALD cycles.

Conclusions

In this report, we demonstrated the applicability of atomic layer deposition for the formation of multifunctional ordered mesoporous core-shell nanocomposites using self-standing nanoporous templates obtained from block copolymer self-assembly. Functional, free-standing, polymeric templates with gyroidal morphology and ultralarge pore size obtained from a solution-based approach allow for the deposition of more than 10 nm of a functional material such as titania while porosity is retained with large pore sizes above 10 nm. The thickness of the functional shell and remaining pore size can be tailored through the structure of the original template and the number of ALD cycles. Periodically ordered 3D continuous gyroidal mesoporous crystalline titania monoliths were obtained after calcinations of the composite at 600 °C in air. We further demonstrated that the titania shell can also be crystallized at 600 °C under inert atmosphere forming an ordered porous nanocomposite with a conductive 3D continuous gyroidal carbon core and electrochemically active, crystalline shell. Our results demonstrate that purely mesoporous templates in the form of monolithic films with thicknesses up to about 15 μm and 3D co-continuous gyroidal morphology with open and accessible pores on both surfaces can be used for the

fabrication of homogeneous multifunctional ordered mesoporous core-shell nanocomposites using standard ALD conditions.

Experimental Section

The structure directing triblock terpolymer poly(isoprene)-*block*-poly(styrene)-*block*-poly(ethylene oxide) (ISO) with a total molecular weight of 129.6 kDa and weight fractions of 15.4%, 31.4% and 53.2% for the three respective blocks was synthesized using sequential anionic polymerization according to published protocols.²¹ Phenol-formaldehyde resols with molar mass of less than 500 g mol⁻¹ were used as the template precursor and synthesized using the well-known basic polymerization of phenol and formaldehyde.²¹ Double gyroidal organic-organic hybrids of the triblock terpolymer ISO and phenol-formaldehyde resols were casted as films of approximately 100 μm thickness as described previously.²⁰ The hybrid films were exposed to argon-oxygen plasma for 30 minutes prior to pyrolysis at 450 °C under nitrogen.

For continuous flow ALD, a Beneq TFS200 system was used with titanium tetrachloride (TiCl₄, purum, ≥98%, Sigma-Aldrich) and deionized water as the titania precursors. An Arradiance GemStar benchtop ALD system was used for ALD with soaking time. Pulse, purge and soaking times are summarized in Table 1. All depositions were done at 150 °C. The polymer-titania composites were subsequently pyrolyzed at 600 °C or 900 °C under nitrogen, respectively, or calcined at 600 °C in air (see text).

SEM and EDX of composites were carried out on a Zeiss LEO 1550 FE-SEM operating at an accelerating voltage of 10 kV equipped with an in-lens detector and an EDX spectrometer (Quantax EDS, XFlash 3000 silicon drift detector, Bruker Nano GmbH). X-ray diffraction patterns were obtained on an Ultima IV multipurpose X-ray diffraction system from Rigaku using Cu Kα radiation (40 V, 44 mA, wavelength 1.5418 Å) in a 2θ range between 20 and 90 degree with a speed of 5 degree min⁻¹. For Raman spectroscopy, a Renishaw InVia confocal Raman microscope was used at room temperature in a backscattering geometry, equipped with a 785 nm diode laser as an excitation source focused on the sample with a 50x magnification.

Acknowledgement

This work was supported as part of the Energy Materials Center at Cornell (emc2), an Energy Frontier Research Center funded by the U.S. Department of Energy, Office of Science, Basic Energy Sciences under Award # DE-SC0001086. This work made use of the Cornell Center for Materials Research Shared Facilities which are supported through the NSF MRSEC program (DMR-1120296). The authors also gratefully acknowledge Dr. Pedro Cunha for helpful discussions.

APPENDIX C

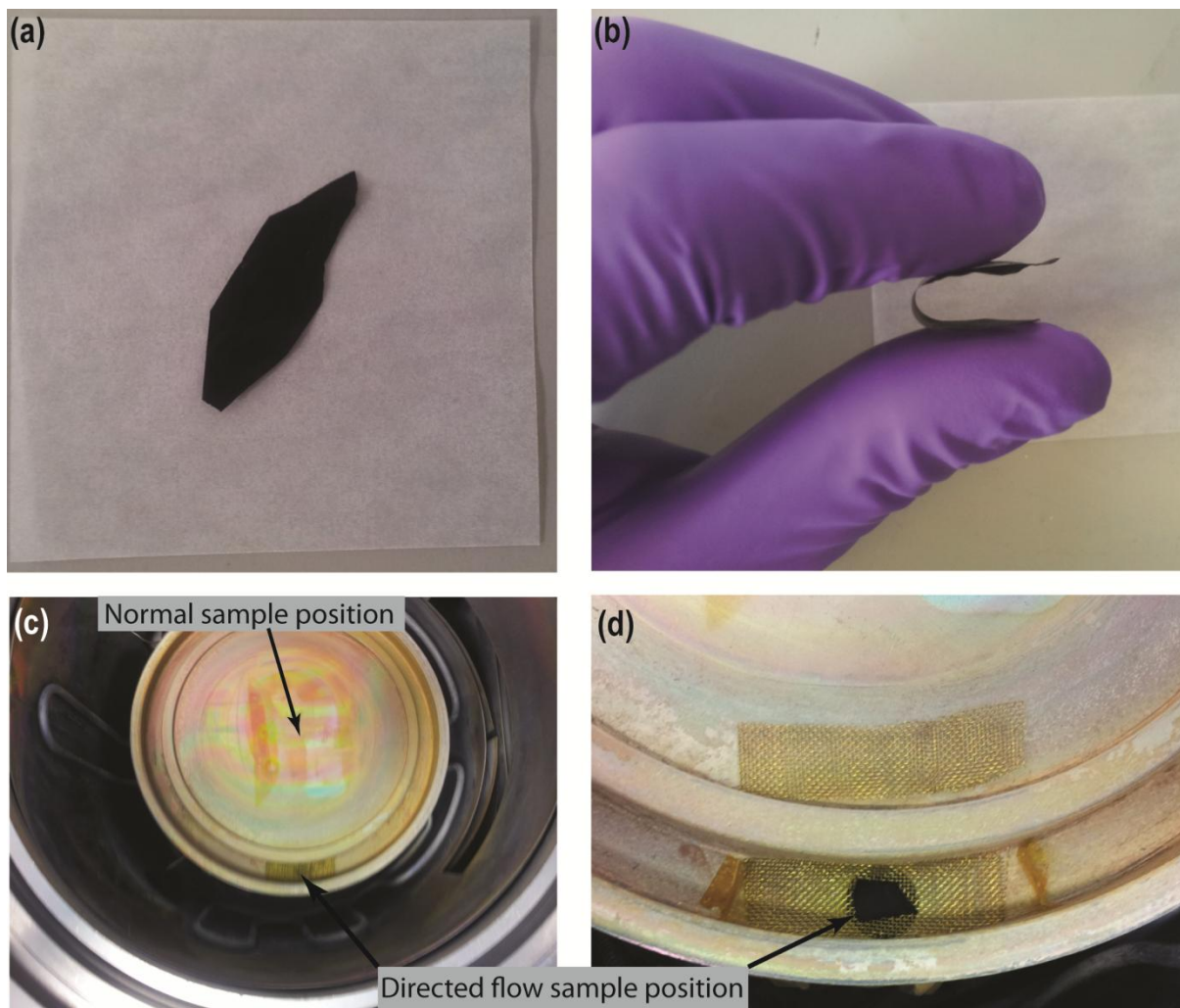


Figure S4.1. Photographs of a large, flexible gyroidal mesoporous resin template (a+b) and of the Beneq TFS200 ALD system used for part of the samples described in this report, indicating the sample position for the normal "flow over" and the "directed flow" procedure.

REFERENCES

- (1) Tarascon, J. M.; Armand, M. Issues and Challenges Facing Rechargeable Lithium Batteries. *Nature* **2001**, *414*, 359–367.
- (2) Armand, M.; Tarascon, J.-M. Building Better Batteries. *Nature* **2008**, *451*, 652–657.
- (3) Dunn, B.; Kamath, H.; Tarascon, J.-M. Electrical Energy Storage for the Grid: A Battery of Choices. *Science* **2011**, *334*, 928–935.
- (4) Arico, A. S.; Bruce, P.; Scrosati, B.; Tarascon, J.-M.; van Schalkwijk, W. Nanostructured Materials for Advanced Energy Conversion and Storage Devices. *Nat. Mater.* **2005**, *4*, 366–377.
- (5) Poizot, P.; Laruelle, S.; Grugeon, S.; Dupont, L.; Tarascon, J. M. Nano-Sized Transition-Metal Oxides as Negative-Electrode Materials for Lithium-Ion Batteries. *Nature* **2000**, *407*, 496–499.
- (6) Bruce, P. G.; Scrosati, B.; Tarascon, J.-M. Nanomaterials for Rechargeable Lithium Batteries. *Angew. Chemie Int. Ed.* **2008**, *47*, 2930–2946.
- (7) Guo, Y.-G.; Hu, Y.-S.; Sigle, W.; Maier, J. Superior Electrode Performance of Nanostructured Mesoporous TiO₂ (Anatase) through Efficient Hierarchical Mixed Conducting Networks. *Adv. Mater.* **2007**, *19*, 2087–2091.
- (8) Lee, J.; Jung, Y. S.; Warren, S. C.; Kamperman, M.; Oh, S. M.; DiSalvo, F. J.; Wiesner, U. Direct Access to Mesoporous Crystalline TiO₂/Carbon Composites with Large and Uniform Pores for Use as Anode Materials in Lithium Ion Batteries. *Macromol. Chem. Phys.* **2011**, *212*, 383–390.
- (9) Wang, Y.; Zeng, H. C.; Lee, J. Y. Highly Reversible Lithium Storage in Porous SnO₂ Nanotubes with Coaxially Grown Carbon Nanotube Overlayers. *Adv. Mater.* **2006**, *18*, 645–649.
- (10) Chen, X.; Zhu, H.; Chen, Y.; Shang, Y.; Cao, A.; Hu, L.; Rubloff, G. W. MWCNT/V₂O₅ Core/shell Sponge for High Areal Capacity and Power Density Li-Ion Cathodes. *ACS Nano* **2012**, *6*, 7948–7955.
- (11) Schoen, A. H. *Infinite Periodic Minimal Surfaces without Self-Intersections*; NASA Technical Note D-5541, **1970**.
- (12) Hajduk, D. A.; Harper, P. E.; Gruner, S. M.; Honeker, C. C.; Kim, G.; Thomas, E. L.; Fetters, L. J. The Gyroid: A New Equilibrium Morphology in Weakly Segregated Diblock Copolymers. *Macromolecules* **1994**, *27*, 4063–4075.

- (13) George, S. M. Atomic Layer Deposition: An Overview. *Chem. Rev.* **2010**, *110*, 111–131.
- (14) Marichy, C.; Bechelany, M.; Pinna, N. Atomic Layer Deposition of Nanostructured Materials for Energy and Environmental Applications. *Adv. Mater.* **2012**, *24*, 1017–1032.
- (15) Kim, E.; Vaynzof, Y.; Sepe, A.; Guldin, S.; Scherer, M.; Cunha, P.; Roth, S. V.; Steiner, U. Gyroid-Structured 3D ZnO Networks Made by Atomic Layer Deposition. *Adv. Funct. Mater.* **2014**, *24*, 863–872.
- (16) Hamann, T. W.; Martinson, A. B. F.; Elam, J. W.; Pellin, M. J.; Hupp, J. T. Aerogel Templated ZnO Dye-Sensitized Solar Cells. *Adv. Mater.* **2008**, *20*, 1560–1564.
- (17) Cameron, M. A.; Gartland, I. P.; Smith, J. A.; Diaz, S. F.; George, S. M. Atomic Layer Deposition of {SiO₂} and {TiO₂} in Alumina Tubular Membranes: Pore Reduction and Effect of Surface Species on Gas Transport. *Langmuir* **2000**, *16*, 7435–7444.
- (18) Knez, M.; Nielsch, K.; Niinistö, L. Synthesis and Surface Engineering of Complex Nanostructures by Atomic Layer Deposition. *Adv. Mater.* **2007**, *19*, 3425–3438.
- (19) Biener, M. M.; Biener, J.; Wichmann, A.; Wittstock, A.; Baumann, T. F.; Bäumer, M.; Hamza, A. V. ALD Functionalized Nanoporous Gold: Thermal Stability, Mechanical Properties, and Catalytic Activity. *Nano Lett.* **2011**, *11*, 3085–3090.
- (20) Werner, J. G.; Hoheisel, T. N.; Wiesner, U. Synthesis and Characterization of Gyroidal Mesoporous Carbons and Carbon Monoliths with Tunable Ultralarge Pore Size. *ACS Nano* **2014**, *8*, 731–743.
- (21) The titania thickness of the witness sample (flat control substrate) was 12.8 nm.
- (22) Tuinstra, F.; Koenig, L. Raman Spectrum of Graphite. *J. Chem. Phys.* **1970**, *53*, 1126–1130.
- (23) Ko, T.-H.; Kuo, W.-S.; Chang, Y.-H. Raman Study of the Microstructure Changes of Phenolic Resin during Pyrolysis. *Polym. Compos.* **2000**, *21*, 745–750.
- (24) Zhou, Y.; Fichtorn, K. a. Microscopic View of Nucleation in the Anatase-to-Rutile Transformation. *J. Phys. Chem. C* **2012**, *116*, 8314–8321.
- (25) Zhang, H.; Banfield, J. F. Thermodynamic Analysis of Phase Stability of Nanocrystalline Titania. *J. Mater. Chem.* **1998**, *8*, 2073–2076.

CHAPTER 5

GYROIDAL NANO-INTEGRATED SOLID-STATE 3D-BATTERY

Abstract

New energy storage concepts are indispensable in meeting increasing energy needs of a modern society. Battery technology in particular is lacking behind the fast-paced developments in the electronics sector, including portable electronics and disconnected autonomous systems. The need for long-lasting energy supply and high power capability combined with small volume requirements poses fundamental challenges for electrochemical energy storage. Solid-state three-dimensional (3D) batteries as a revolutionizing energy storage architecture may disconnect the unfavorable link between power capability, energy density and device size. At the same time it may increase battery safety due to the lack of volatile and flammable liquid organic electrolytes. While 3D-batteries with component dimensions of microns have been realized, they suffer from rate-limiting ion diffusion through thick solid layers. Here we present a solid-state nano-integrated 3D-battery architecture with macroscopic dimensions and anode, electrolyte, and cathode layer dimensions below 20 nm. This nano-3D-battery uses a block copolymer self-assembly directed double gyroidal mesoporous carbon anode that is conformally coated with an ultra-thin poly(phenylene oxide) electrolyte and backfilled with sulfur and poly(ethylene dioxothiophene) as the cathode phase. All materials are either polymer based or low to moderate temperature processable, beneficial for large scale processing. The battery exhibits a reversible discharge plateau at 2.5 V with 0.25 mAh cm² reversible capacity and a maximum capacity of 2.6 mAh cm² or 43 mAh cm³.

Introduction

Portable electronics including communication devices, sensors, hand-held entertainment devices, and autonomous systems such as medical monitoring devices are becoming increasingly distributed and at the same time smaller in size.^{1,2} While research in the field of electronics over the past decades has enabled continuous miniaturization of the active parts of these devices, mobile energy sources necessary to power disconnected systems lack behind the demand in capabilities.³⁻⁶ Battery systems like lithium ion batteries (LIB) as one option for energy and power supplies of portable and autonomous systems don't meet the requirements of miniaturized devices. As a result the battery is often many times larger than the device itself.⁷ Furthermore, bridging the gap between the power densities of capacitors (fast energy release) and the energy densities of batteries (long-lasting energy) remains a fundamental problem in electrochemical energy storage (EES).

Batteries have to be improved in several categories: Energy density (per mass, volume and footprint), power capability, variable power output, and longevity, to name only a few of the most important ones.⁸ Over the past decade, much emphasize has been put on two categories of battery research: The discovery of new materials with higher energy density and power capability, and nanostructuring and compositing of existing materials to increase their performance. The first of these research directions focuses on enhancing charge storage capability per unit mass and volume of the active material through high-valent ions or conversion reactions as charge storage mechanisms, next to faster solid-state ion-diffusion for more rapid energy accessibility. The second research direction improves charge storage capabilities through morphology and structure control over the active materials, in particular using nanostructuring and multifunctional composite formation.^{9,10} This approach holds particularly high promise for electrodes meant for high-power demanding applications due to large nanomaterial porosity leading to good accessibility of liquid electrolytes as well as short ion diffusion paths through solid electrode materials.⁷ Often these two categories overlap and some advanced energy storing materials, such as silicon or titania, only perform well when nanostructured while others, such as sulfur, need to be composited.¹¹⁻¹³ While

specific energy and power densities (per mass) are often improved in such nanomaterials, volumetric and areal densities are tough to assess and often not reported. These metrics suffer from the high porosity of nanostructured materials and concomitantly from the extra electrolyte necessary to fill the highly porous nanomaterials adding substantially to total system weight and thereby further decreasing the total energy density of the device.

These issues are particularly detrimental for use of batteries as energy sources in devices such as microelectromechanical systems (MEMS), or implantable medical sensors, where a small footprint and volume of the energy source is crucial. In fact, in many of these devices the overall size is determined by the dimensions of the battery.^{5,6,14,15} The problem lies in the battery assembly and architecture. In traditional batteries, anode and cathode materials are often compounded with some conductive additive and polymeric binder and subsequently casted onto current collectors such as metal foils. In the final battery assembly an inert and porous separator soaked in liquid electrolyte or a solid electrolyte is then sandwiched between anode and cathode. In this stacked architecture of composite electrodes the individual layers are typically 10s to 100s of microns in thickness. While this architecture works well for conventional use in applications such as laptops and cell phones, it is poorly transferrable to small-scale devices. Thin film batteries on the other hand, which are often employed in MEMS applications, have electrode films only a few microns thick that are separated by a few microns of solid electrolyte, such as LiPON, and supported on a substrate.¹⁶⁻¹⁸ The areal energy density of thin film batteries is correlated to electrode film thickness. Since solid electrode materials are often poor ionic conductors, higher energy density typically yields in a reduction of power capability.¹⁶ An approach to disconnect areal energy density from power capabilities of batteries has been proposed over a decade ago, where not only the active materials are nanostructured, but the entire battery with all its components is integrated into a three-dimensional (3D) micro- or even nanoarchitecture.^{6,14,16,19} This energy storage architecture was termed a 3D-battery. In 3D batteries the necessary three-layer design of anode-electrolyte-cathode is still present, albeit on the micron- or nanoscale, while at the same time utilizing the third dimension to

increase areal energy density without increasing electrode thickness.^{14,19} This architecture ensures that the energy density increase by exploiting thicker films does not decrease the rate of energy accessibility or even the utilization efficiency of the active material, since anode-cathode separation is independent of device thickness. This argument assumes that electronic conductivity through anode and cathode phases is sufficiently high and is not rate-determining.

Different architectures have been proposed for 3D batteries including interdigitated pillar-like and plate-like electrodes, as well as porous rod-arrays or networked electrodes coated with the electrolyte and backfilled with the counter electrode.^{7,14,15} Some of the proposed architectures have been realized, but only on the micron scale. For example, Min *et al.* employed photolithography to generate interdigitated carbon rods where each alternating row of rods was separately electronically accessible.²⁰ In this way, every other row was functionalized with a polypyrrole coating and it was demonstrated that this architecture exhibited a higher energy density than a similarly prepared planar film. The 3D-battery performance was limited, however, due to shortage between the opposing electrode rods. In a similar synthesis strategy, Braun, King *et al.* used photolithographically defined interdigitated gold electrodes to electrodeposit 3D current collectors, and then selectively deposited the anode and cathode materials on alternating gold electrodes.^{21,22} This approach combined the 3D battery architecture concept on the macroscale with nanoporosity in the electrodes, yielding the highest areal power density reported for such a device. This study as well as the nanopore-battery concept of Liu *et al.* demonstrated the need of an integrated current collector for high-power cells.²³ These and other examples, including 3D-printing of microbatteries, all employed liquid electrolytes between electrodes with microns of separation distance.²⁴ While this assures fast ion transport between anode and cathode, sealing of the device and flammability of organic liquid electrolytes pose challenges and safety concerns. The inefficient use of space due to the large “dead” volume of the electrolyte might also result in limitations of these designs.

All-solid-state 3D-battery architectures avoid these limitations and offer a safe alternative. Such devices have primarily been accomplished on the macro scale with component dimensions of order of

microns.^{16,25-27} While compared to planar architectures a significant areal energy density improvement was obtained for these 3D-batteries, power capabilities suffer from microns of solid-state ion-diffusion. Since the diffusion time is proportional to the square of the critical dimension, decreasing component dimensions down to the nanoscale would mean a significant increase in power capability. While quite promising, only very few three-dimensionally integrated composites with components on the nanoscale have been reported, however.^{28,29} Rhodes *et al.* used manganese oxide aerogels supported on an ITO substrate as a nanoporous electrode, which was subsequently electrochemically coated with an ultra-thin polymer electrolyte and backfilled with ruthenium oxide as the second electrode material. To the best of our knowledge, despite the successful placement of all three battery components (anode, electrolyte, and cathode), no working device on the nanoscale has been reported to date. The requirements for the successful synthesis of a working nano-integrated 3D-battery are challenging: Both electrode phases have to be electronically conducting or composited with a current collecting material on the nanoscale. The conformal coating of the nanometer-thick solid electrolyte has to be pin-hole free and sufficiently electronically insulating, while providing a reasonable ionic conductivity. In the case of a lithium-ion 3D-battery, one of the electrodes has to be lithiated (present in the reduced state), either chemically or electrochemically. Finally, independent contacting of anode and cathode nanophases has to be accomplished without disrupting the solid electrolyte. The synthesis of multiple functional materials with spatial control on the nanoscale also requires the compatibility of the individual chemistries. This is in contrast to conventional composite batteries, where anode, electrolyte/separator, and cathode can be prepared individually and then physically sandwiched together.

Here, we describe an approach to “synthesize” a nano-integrated 3D solid-state battery using block copolymer self-assembly directed free-standing mesoporous double gyroidal carbon as the starting platform. The gyroidal carbon material with a pore size of 40 nm acts as the conductive anode and is electrochemically coated with an ultra-thin polymer electrolyte. This mesoporous solid anode-electrolyte assembly is subsequently back-filled with sulfur as the active cathode material and poly(ethylene

dioxothiophene) (PEDOT) as current collector. After electrochemically reducing the cathode material, the carbon-lithium sulfide 3D-battery shows reversible battery cycling performance. To the best of our knowledge, this is the first report of a working 3D-battery with all components integrated on the nanoscale. Our nano-3D battery architecture allows a decrease in footprint area by more than three orders of magnitude, due to wrapping up all nanoscaled battery components into a network and exploiting the third dimension. As an illustration, keeping all other parameters and materials the same, a flat three-layer battery design with the same interfacial area as the device described here would take up an area of approximately 520 cm², compared to 0.1 cm² for the current device, a difference of 3-4 orders of magnitude. Moreover, all components for this first realization of the nano-integrated 3D battery concept are chosen to be compatible with large scale processing. This means they are either polymer based (polymer based anode formation; electropolymerization of solid electrolyte; solution polymerization of cathode current collector) or low to moderate temperature processable (active cathode material). In particular, the synthesis does not include any expensive and prohibitively time consuming nanofabrication processes, making the chosen approach compatible with many high throughput fabrication processes.

Results and discussion

The assembly of an all-integrated battery on the nanoscale requires precise spatial control over the synthesis and deposition of every individual component. It is of crucial importance that the electrodes are continuous throughout the entire device and exhibit no bottlenecks. Furthermore, the electrode phases need to be electrically conducting, either intrinsically or in form of a composite, to make their redox-activity electrically accessible. This is due to the absence of conductive additives or binders that are commonly employed in standard composite electrodes. Additionally, anode and cathode phases have to be separated by a sufficiently electronically insulating but ionically conducting phase (electrolyte) to avoid short-circuits and leakage currents. The nano-3D-battery assembly procedure pursued here starts with a monolithic double gyroidal mesoporous carbon (mG^DMC) framework as the anode active material and current collector in one. The gyroidal carbon is conformally coated through electropolymerization of

poly(phenylene oxide) (PPO) as the solid polymer electrolyte, followed by infiltration of sulfur and *in-situ* polymerized poly(ethylene dioxothiophene) (PEDOT) as the active cathode material and current collector, respectively (schematically shown in Figure 5.1a).

The bicontinuous gyroidal morphology offers a three-dimensionally homogeneous structure with two interpenetrating minority networks that have relatively constant cross-sectional diameter that constitute the pores in our mG^DMCs, separated by a majority matrix with constant thickness (Figure 5.1a, left). We believe that the homogeneity of the gyroid morphology makes it a preferred candidate for a nano-integrated 3D-battery as compared to e.g. inverse opal structures. The mG^DMC material was synthesized using the self-assembly of triblock terpolymer poly(isoprene)-*block*-poly(styrene)-*block*-poly(ethylene oxide) (ISO) in the presence of oligomeric phenol-formaldehyde resols as carbon precursor. Polymer characteristics and details of the ISO-resols co-assembly can be found in the experimental section and in previous work.³¹ After pyrolysis the carbonized material retains its monolithic integrity, an essential characteristic for the successful assembly of the full 3D-cell (Figure 5.1b). In order to allow enough space for successive electrolyte coating and cathode back-filling, sufficiently large pore sizes without bottlenecks are required. The large molar mass ISO (130 kDa) used here allowed for the synthesis of mG^DMC with ultra-large unit cell size of 131 nm, pore size of 40 nm, and carbon wall thickness of 16-17 nm (Figure 5.1c,d and S5.1). The mesopores constitute a pore volume of 0.9 cm³ g⁻¹ corresponding to a porosity of 64%. Irrespective of morphology it is common in block copolymer (BCP) self-assembly to observe lamellar layers on surfaces of casted films due to the surface energy differences between individual blocks and their corresponding affinity to air and the casting dish material.³¹ These surface reconstituted lamellar capping layers were removed using plasma treatment of the polymeric-organic hybrid films prior to carbonization. This treatment is essential to make the interior porosity accessible from the surfaces, but also causes the surface pores to be slightly smaller than in the bulk (Figure 5.1c). The monolithic gyroidal carbon materials used in this study have a thickness of approximately 60-70 microns and geometrical areas of 8-12 mm² (Figure 5.1b,c). This geometry leads to an average

areal carbon loading of approximately 4 mg cm^{-2} assuming a carbon density of 2 g cm^{-3} . The carbon monoliths were attached to a wire with silver epoxy in edge-on geometry (Figure 5.1b). In order to avoid unwanted side reactions of the silver connection in subsequent steps, the contact was sealed with silicone sealant.

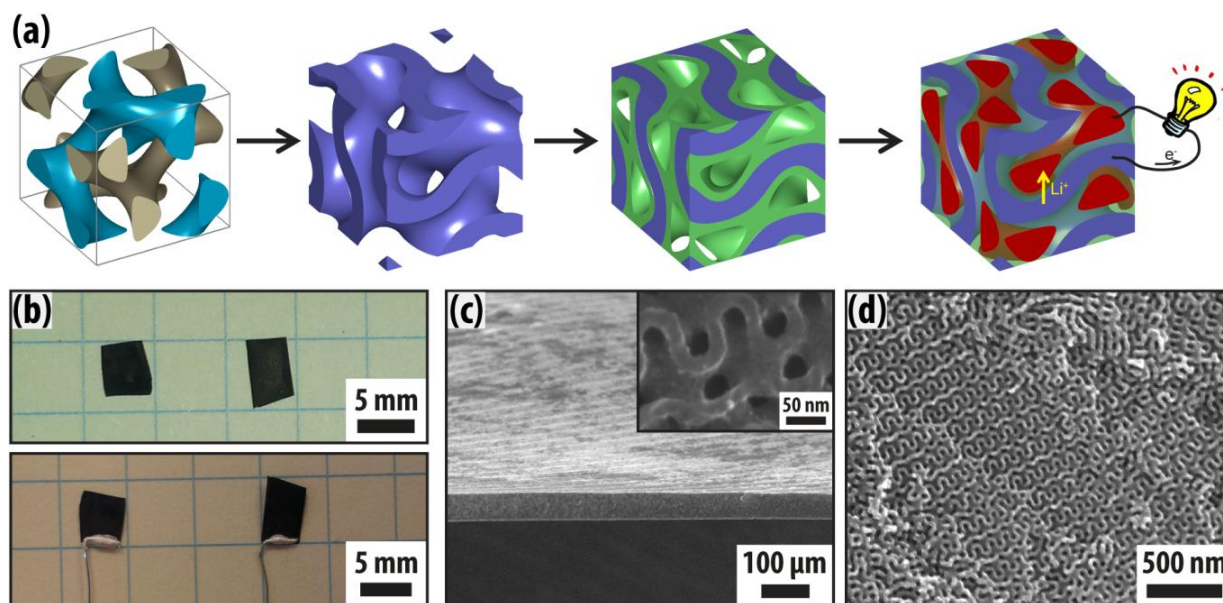


Figure 5.1. Nano-integrated 3D-battery assembly from gyroidal mesoporous carbon monoliths. (a) Carbon monoliths (blue, second from left) are obtained from BCP self-assembly directed gyroidal hybrid formation (left, showing minority BCP domains) with resols precursors and subsequent carbonization. Nanoscopic gyroidal majority domains of the carbon anode (blue) are conformally coated with a nanoscopic polymer electrolyte layer (green), which in turn is back-filled with a nanoscopic cathode composite (red). (b) Photographs of gyroidal mesoporous carbon monoliths as-made (top) and attached to a wire in edge-on geometry (bottom). (c,d) SEM images of a gyroidal mesoporous carbon monolith exhibiting uniform thickness of approximately $60 \mu\text{m}$ (c), surfaces with open and accessible gyroidal mesoporosity (c, inset), and uniformly structured cross-section (d).

The solid electrolyte on the continuous mesoporous anode has to meet a number of requirements: (1) Conformal deposition without pinholes on the mesopore walls; (2) Uniform deposition throughout the entire anode framework; (3) Sufficiently high electrical resistance; (4) Ionic conductivity; (5) Thickness of $\sim 10 \text{ nm}$ providing enough residual porosity for successful infiltration with the cathode composite. The first three requirements assure that no short-circuit between the two electrodes can occur and that leakage currents are kept to a minimum. Ionic conductivity is essential for the lithium exchange between anode and cathode during charge and discharge. Some methods have been proposed and reported for the

deposition of ultra-thin solid electrolyte films, including atomic layer deposition, chemical vapor deposition, and electro-deposition/polymerization.^{29,32-34} Gas phase deposition methods such as the first two mentioned above are either line-of-site methods or rely on sufficient and homogeneous precursor diffusion towards the surface in the allotted reaction time, which can cause incomplete or non-uniform deposition in bulk-sized nanoporous materials.³⁵ Despite recent advances in the field, these methods are not applicable yet for deposition of ultra-thin solid electrolytes for mesoporous materials with macroscopic dimensions. Rolison *et al.* have demonstrated the use of electrodeposition of polymers (electropolymerization) such as poly(*ortho*-phenylene diamine) (POPD) and poly(phenylene oxide) (PPO) as a viable method to synthesize thin film electrolytes of less than 10 nm, with reported electrolyte behavior on flat substrates.^{34,36} The advantage of electropolymerization is multifold. The surface reaction time can be precisely controlled through application of the oxidation potential. This allows to decouple the polymerization event from monomer or reactant diffusion through the nanopores, which is particularly important for macro-scaled monolithic materials. Monomers such as OPD and phenol form insulating polymeric films when oxidatively deposited under basic conditions. Electrical insulation results in self-limiting polymerization and at the same time causes a beneficial self-regulating synthesis to afford conformal and complete deposition. Self-regulation characteristics stem from the attraction of monomers diffusing towards the surface to areas with the highest electric field density, leading to the propensity of deposition on previously uncoated areas until the entire surface is homogeneously covered. Due to the higher electrical resistance and deposition in organic solvent, which aids solution infiltration and wetting of the hydrophobic carbon mesopores, we used poly(phenylene oxide) (PPO) as the solid polymer electrolyte. The deposition thickness and molecular rejection capability of PPO is deposition-potential dependent, forming a thinner and denser film at higher potentials.³⁷ Cyclic voltammetry of the PPO polymerization solution at 20 mV s⁻¹ showed a broad irreversible oxidation peak around 0.08 V vs. Ag/Ag⁺ that decayed rapidly over cycling (Figure 5.2a). Very little indication of an oxidation peak or double layer current was present after 10 cycles, indicating the complete insulation of the carbon surface and potential overgrowth of the polymer layer, blocking the pores.

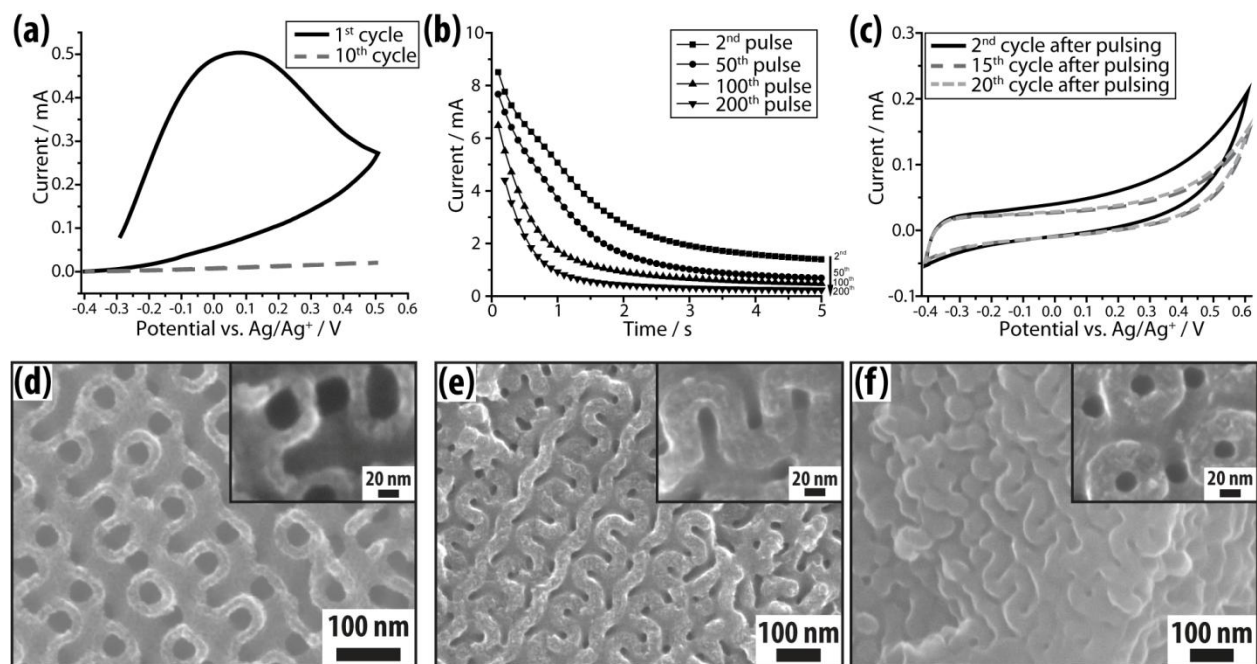


Figure 5.2. Electropolymerization of ultrathin solid polymer electrolyte on mG^D MC anode. (a) Cyclic voltammogram (CV) of mG^D MC anode in the phenol electropolymerization solution. The broad oxidation peak of the first cycle disappears completely after 10 cycles. (b) Current-time traces of selected potentiostatic deposition pulses at 0.6 V vs. Ag/Ag^+ showing the decrease in double layer and oxidation current. (c) CVs after pulsed potentiostatic PPO deposition in the same solution showing only double layer current without a phenol oxidation peak. (d-f) SEM images of mG^D MC anode before (d) and after (e,f) pulsed potentiostatic electropolymerization of PPO. Freshly cleaved cross-sections are shown in (d,e) and the surface in (f). Insets show cross-sections at higher magnification.

In order to afford a thinner PPO film, we used potentiostatic electropolymerization at 0.6 V vs. Ag/Ag^+ , well above the oxidation potential of the phenolate ion and in the mass transport limit. This assures that every incoming monomer experiences the same oxidizing potential on the bare carbon surface. Pulses of 5 sec at the oxidation potential were used with 10 sec of equilibration time to allow for sufficient monomer diffusion throughout the mesoporous carbon monoliths during electropolymerization. The resulting current-time response is a superposition of double layer current (decaying exponentially) at the early pulse times and oxidation current. The initial current due to the double layer formation decays slightly over 200 pulses, while the current due to monomer oxidation decays by an order of magnitude, indicating the insulation of the carbon surface (Figure 5.2b). This is in strong contrast to the background response of the electrolyte, where only double layer current with little tailing and no change over 200 pulses is observed (Figure S5.2a). Cyclic voltammograms (CVs) after the pulsed potentiostatic PPO

deposition in the polymerization solution show mostly double layer characteristics with no oxidation peak occurring at the oxidation potential of the phenolate ion (Figure 5.2c). Some oxidation current that is present at higher potentials stabilizes over cycling, indicating no further insulation of the carbon surface. The area of the CVs after electropolymerization is smaller than in the pure electrolyte, but orders of magnitude larger than the double layer current of a flat PPO-coated carbon substrate with similar geometrical surface area (Figure S5.2). This indicates the retained accessibility of the mesoporosity after pulsed PPO electropolymerization. Scanning electron microscopy (SEM) confirms the deposition of a thin film on the gyroidal carbon mesopores (Figure 5.2d-f). The thickness of the PPO films was estimated from the wall-to-wall distance before and after electropolymerization to be around 8-10 nm. The outer surface of the gyroidal carbon monoliths demonstrated open porosity after PPO deposition, confirming the electrochemical results that no pore clogging occurred using the pulsed potentiostatic method (Figure 5.2f).

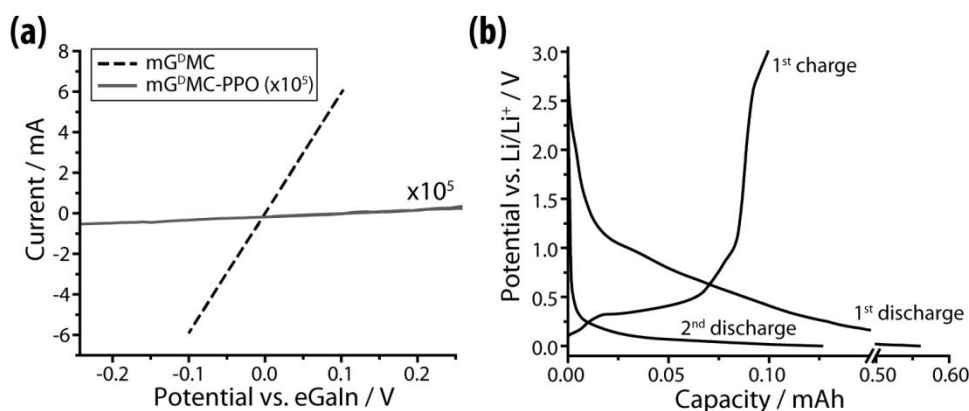


Figure 5.3. Performance test of ultra-thin PPO polymer electrolyte layer. (a) Resistance measurements using a two-electrode configuration of the wire-connected mG^DMC anode before (black) and after (red) PPO electropolymerization showing an increase in resistance by more than 5 orders of magnitude. Note, the current of the PPO coated monoliths was multiplied by a factor of 10⁵ for easier comparison. (b) Discharge and charge curves of a PPO-coated mG^DMC anode demonstrating reversible lithiation-delithiation through the PPO-layer.

The performance of the ultra-thin polymer electrolyte layer was evaluated using two-probe resistance and lithiation measurements. The change in electrical resistance was measured by contacting one surface of the carbon-PPO hybrid with a liquid gallium-indium eutectic (eGaIn). The slope of the potential-

current curves between the carbon-connected wire and the eutectic contact corresponds to the absolute resistance through the contact area. An increase in resistance by more than 5 orders of magnitude from 17Ω to $5 \text{ M}\Omega$ due to PPO deposition was obtained (Figure 5.3a). A very similar electrical resistance was measured for a flat PPO-coated carbon substrate measured in the same geometry (Figure S5.3). In order to elucidate if the PPO-layer is permeable for lithium ions and therefore acts as an electrolyte, a PPO-coated $\text{mG}^{\text{D}}\text{MC}$ was galvanostatically lithiated and delithiated in a two-electrode liquid cell against lithium metal. After soaking in the liquid electrolyte (1 M lithium perchlorate in a 1:1 mixture of ethylene carbonate to dimethyl carbonate) for two days, the free-standing nanoporous anode-electrolyte assembly showed reversible lithiation-delithiation (Figure 5.3b). The first discharge (lithiation of carbon) curve exhibits a plateau around 1 V vs. Li/Li^+ and very large capacity as is commonly observed for the first discharge of carbon anode materials due to built-up of a solid-electrolyte interface (SEI).³⁸ The following charge (delithiation) and discharge (lithiation), however, show a capacity of 0.1 and 0.13 mAh, respectively, demonstrating reversible lithium intercalation. These capacities correspond to approximately 1 mAh cm^2 and 250 mAh g^{-1} , which is in good agreement with the reversible capacity observed from coin cell tests with powdered gyroidal carbon anode material without PPO-coating (Figure S5.3). Again, the behavior of the flat PPO coated carbon substrate is very similar, with the exception of much less capacity associated to SEI layer formation due to the significantly smaller surface area (Figure S5.3).

After successful coating of the 3D carbon anode with a polymer electrolyte, the remaining mesopores were infiltrated with the cathode composite. Elemental sulfur was used as the active cathode material. Sulfur exhibits an intermediate discharge voltage versus lithium metal or carbon of 2-2.5 V. Sulfur can be infiltrated into nanopores using liquid infiltration at low temperature of (155 °C).¹³ Since sulfur is electronically insulating, it has to be combined with another material that acts as a three-dimensionally nano-integrated current collector. We used poly(ethylene dioxothiophene) (PEDOT) as a well-known conducting polymer. The monomer EDOT can be polymerized through chemical or electrochemical oxidation. The doped forms of conducting polymers are commonly insoluble and, therefore, infiltration

into nanopores is problematic. We infiltrated with the monomer (EDOT) and a chemical oxidizing agent (iron(III) *para*-toluenesulfonate), which led to in-situ polymerization of PEDOT inside the mesopores of our gyroidal mesoporous PPO-coated carbon monoliths.³⁹

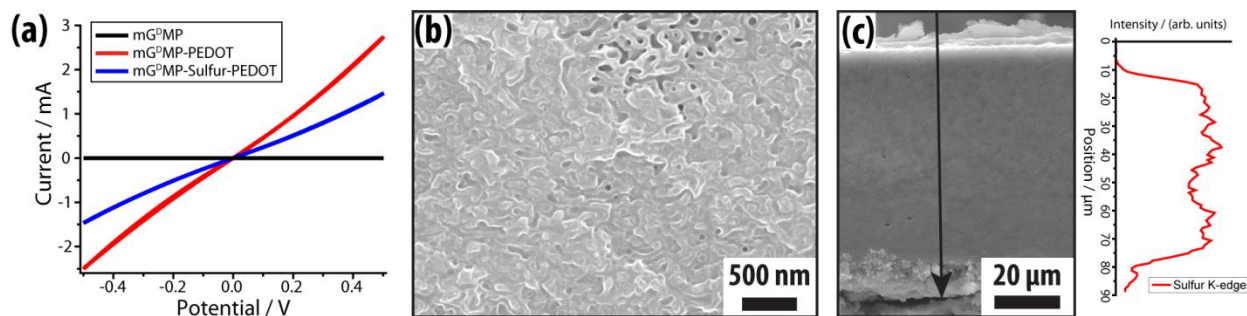


Figure 5.4. Cathode composite infiltration. (a) Resistance measurements of insulating double gyroidal mesoporous polymer monoliths (mG^DMP, black) back-filled with PEDOT (red), and sulfur and PEDOT (blue) using a two-probe configuration with contacts on either monolith surface. (b) Cross-sectional SEM image of a sulfur-PEDOT backfilled mG^DMP indicating good infiltration efficiency. (c) Cross-sectional SEM image of a sulfur-PEDOT backfilled PPO-coated mG^DMC (3D-battery) and EDX line scan of the sulfur signal across the film (line scan position indicated by black arrow in SEM and shown in Figure S5.4a).

In order to separately test the functionality of the PEDOT current collector prepared by this method in a nanoporous template, we measured the resistance across an insulating monolithic double gyroidal mesoporous polymer (mG^DMP) after infiltration (Figure 5.4a). The mG^DMPs were obtained from the same synthesis as its carbon analogue, but with heat treatment to only 450 °C. At this temperature, the structure directing block copolymer ISO decomposes and forms porosity, while the phenol-formaldehyde resols convert into an electronically insulating phenolic resin (black line in Figure 5.4a). The resistance decreases to 180 and 330 Ω after infiltration with PEDOT, or sulfur and PEDOT, respectively. This result independently demonstrated conductivity of the PEDOT polymer and its percolation throughout the nanoporous framework. SEM analysis confirms good infiltration of PEDOT into the nanopores (Figure 5.3b). The complete cross-section of a PPO-coated and sulfur-PEDOT backfilled 3D-battery is shown in Figure 5.3c. Thin polymer overlays of a few microns on either surface of the monoliths can clearly be distinguished. This feature from the PEDOT infiltration-synthesis is beneficial for subsequent contacting of the cathode composite phase, since any mechanical stress directly on the ultra-thin PPO coating could

cause disruption of the separating layer and lead to short-circuiting between anode and cathode phases. The infiltration of sulfur and the sulfur containing PEDOT appears to be fairly homogeneous throughout the entirety of the 3D-battery cell, as revealed by the constant energy dispersive X-ray spectroscopy (EDX) signal of sulfur across the film (Figure 5.3c and S5.4a,b). Quantitative analysis of the EDX spectra of the three points shown in Figure S5.4b estimate a carbon to sulfur ratio of 3.8, 3.0, and 3.4 at the top, middle and bottom of the film, respectively.

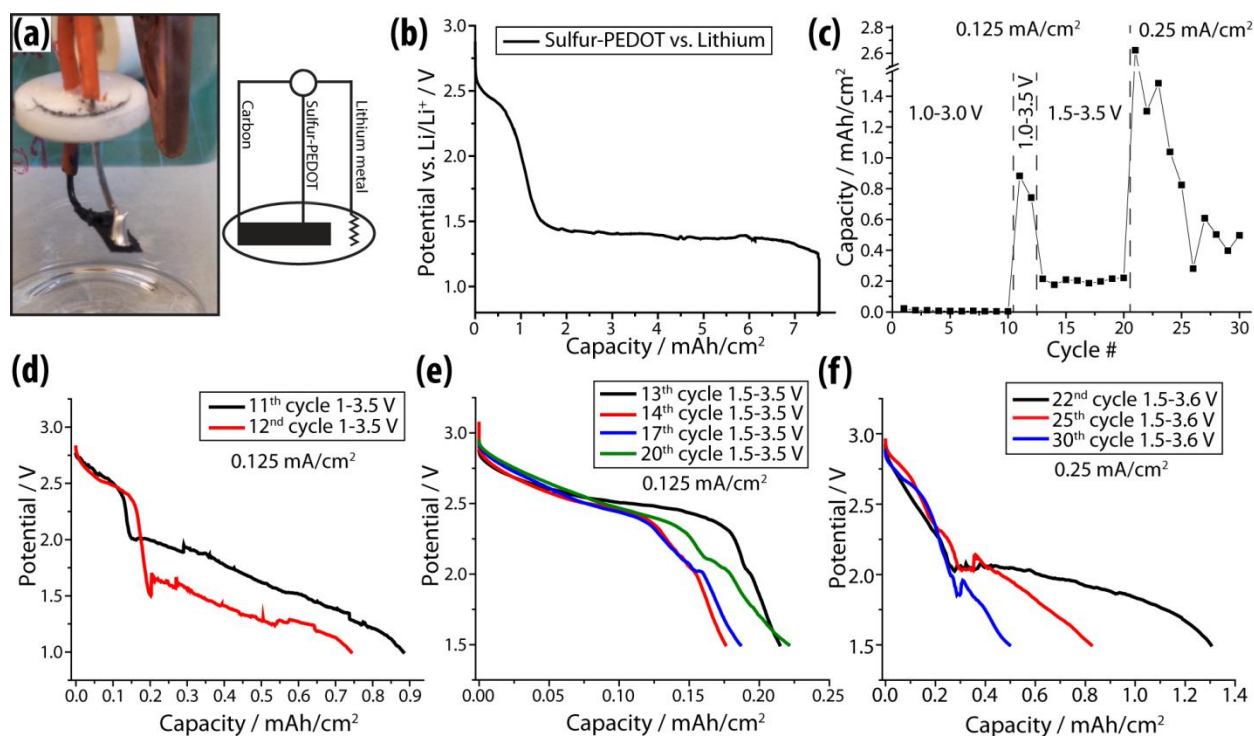


Figure 5.5. Performance test of an all-nano-integrated 3D-battery. (a) Photograph and schematic of a fully assembled 3D-battery after contacting the cathode phase on the top surface and before lithiation (alligator clip for the lithium metal can be seen on the right). (b) Discharge curve of the sulfur-PEDOT phase vs. lithium metal in liquid electrolyte at 0.125 mA cm^{-2} . (c) Discharge capacities of the tested cycles. The cycle conditions (voltage window and current rate) are indicated in the graph. (d) Discharge curves of the first two cycles that were run in the potential window of 1-3.5 V at a current of 0.125 mA cm^{-2} (11th and 12th cycle total). (e) Discharge curves of selected cycles that were run in the potential window of 1.5-3.5 V at a current of 0.125 mA cm^{-2} (13th-20th cycle total). (f) Discharge curves of selected cycles that were run in the potential window of 1.5-3.6 V at a current of 0.25 mA cm^{-2} (22nd-30th cycle total).

In order to introduce lithium into the nano-integrated 3D-battery, the sulfur-PEDOT phase was electrochemically reduced in a two-electrode configuration versus lithium metal (Figure 5.5a,b). A 3D-battery with an area of 0.08 cm^2 was soaked for 2 days in a liquid electrolyte (1 M LiClO_4 in 1:1 vol

DOL:DME) and then discharged at a constant current of 0.125 mA cm^{-2} . The electrolyte was chosen to avoid unwanted side reactions with polysulfides that carbonate-based electrolytes undergo.⁴⁰ The discharge curve exhibited two plateaus around 2.4 V and 1.5 V vs. Li/Li^+ , respectively (Figure 5.5b). The plateau at 2.4 V matches well with the sulfur reduction potential to form long-chain polysulfides.^{13,41} The second discharge plateau is well below the commonly observed one (which is around 2 V vs. Li/Li^+). The large overpotential, however, is expected as PEDOT becomes insulating at these low potentials.⁴² This "external" reduction-lithiation of the sulfur-PEDOT phase was followed by cycling of the 3D-battery at a constant current of 0.125 mA cm^{-2} (carbon vs. lithiated sulfur-PEDOT, Figure 5.5c-e, S5.4, and S5.5). After the first charge to 3 V (Figure S5.4c), the cell was cycled 10 times between 1 and 3 V with very little discharge capacity obtained (Figure 5.5c, S5.4d). After these initial cycles, the 3D-battery was removed from the liquid electrolyte and cycled between 1 and 3.5 V for two cycles (Figure 5.5d, S5.5a). The discharge curves exhibited a reversible plateau around 2.5 Volts with a capacity of $0.12\text{-}0.18 \text{ mAh cm}^{-2}$ and further irreversible capacity at lower potentials. In order to investigate the reversibility of the plateau at 2.5 V, the voltage window was decreased to 1.5-3.5 V in subsequent cycles. The next 8 cycles showed reversible discharge capacities of $0.18\text{-}0.23 \text{ mAh cm}^{-2}$ at a constant current of 0.125 mA cm^{-2} from the discharge plateau at 2.5 V. This data clearly demonstrates reversible charge and discharge of this all-nano-integrated 3D-battery. The subsequent 10 cycles were run at a current of 0.25 mA cm^{-2} between 1.5 and 3.6 V (Figure 5.5f, S5.5d). Again, reversible capacity for the first discharge plateau of approximately $0.25\text{-}0.31 \text{ mAh cm}^{-2}$ was observed, together with a high total capacity of 2.6 mAh cm^{-2} for the first cycle at this current rate. The second discharge plateau, however, showed decreasing capacity retention over the subsequent cycles. The reoccurrence of the second discharge plateau above 1.5 V is most likely due to the increased cut-off voltage for charging the 3D-battery at the higher current rate, which lead to a much higher charge capacity (Figure S5.5d). The current rate also influenced the coulombic efficiency of the 3D-battery cell, which is expressed as the ratio of discharge over charge capacity (Figure S5.5e,f). The capacity discrepancy between charge and discharge is possibly

due to some leakage current through the polymer separator. This should be mitigated at higher charging and discharging rates, as we observed for our 3D-battery.

Conclusion

In this work we demonstrated for the first time the successful synthesis and assembly of a working all-nano-integrated solid-state 3D-battery. Our battery architecture is composed of block copolymer self-assembly derived gyroidal carbon as anode material, an ultrathin poly(phenylene oxide) as solid electrolyte, and prelithiated sulfur-PEDOT composite as the cathode material. Each of these battery components is less than 20 nm in layer thickness, but percolated throughout a macroscopic free-standing architecture in the form of a 3D continuous gyroidal nanonetwork. The successive synthesis steps of each component are compatible with each other, a prerequisite for such an assembly on the nanoscale. The materials employed here are either polymer based or low to moderate temperature processable, which makes it accessible and very attractive for large-scale production. Our nano-integrated 3D-battery demonstrates discharge capacities up to 2.6 mAh cm^{-2} , and a reversible discharge plateau at 2.5 V with capacities of up to 0.25 mAh cm^{-2} . We hope that this work sparks new interest in the development of nano-3D-batteries, and further optimization of the chemistry and components for higher energy and power densities to fully utilize the potential of this intriguing device nanoarchitecture.

Experimental Section

Gyroidal mesoporous carbon anode. The mesoporous carbon monoliths were synthesized using block copolymer (BCP) self-assembly. Structure directing amphiphilic triblock terpolymer poly(isoprene)-*block*-poly(styrene)-*block*-poly(ethylene oxide) (PI-*b*-PS-*b*-PEO, ISO) was synthesized in a step-wise anionic polymerization as described previously.³⁰ The ISO employed here exhibited a total molar mass of 130 kg mol^{-1} , a PDI of 1.09, and respective weight fractions of 15.4%, 31.4% and 53.2% for PI, PS, and PEO. Phenol-formaldehyde resols were used as carbon precursor and synthesized using oligomerization of phenol and formaldehyde in a molar ratio of 1:2 under basic conditions.³¹ Monolithic ISO:resols hybrids with double gyroidal (G^D) morphology were obtained by dissolution of both components (1:0.54

by weight) in tetrahydrofuran (THF) and chloroform (1:1 by weight) and solvent evaporation at 50 °C in a Teflon dish. The dry films were annealed at 125 °C for 24 hours prior to carbonization at 1100 °C for 24 hours. In order to obtain porous film surfaces after carbonization, annealed hybrid films were exposed to argon-oxygen plasma for 40 mins. The free-standing carbon monoliths were cut into the desired shape, attached to a wire in edge-on geometry with silver epoxy (EPO-TEK H20E from EMS), and cured at 80 °C for at least 10 hours. The exposed silver contact was then sealed to the outside using silicone rubber adhesive sealant (Momentive RTV 108) and cured at room temperature for at least 24 hours.

Electrodeposition of polymer electrolyte. The walls and surfaces of the nanoporous carbon anode were conformally coated with poly(phenylene oxide) (PPO) using self-limiting electropolymerization. The polymerization solution in acetonitrile was 0.05 M in phenol and tetramethylammonium hydroxide pentahydrate and 0.1 M in tetrabutylammonium perchlorate (TBAP). The solution was kept under inert gas atmosphere (nitrogen) to prevent oxidation of the deprotonated phenol. A wire-connected gyroidal mesoporous carbon monolith was immersed completely into the solution and left soaking for 15 mins in a septum capped vial. Electropolymerization was conducted in a three-electrode set up with a platinum counter electrode and a Ag/Ag^+ reference electrode (silver wire in acetonitrile with 50 mM silver perchlorate and 0.1 M TBAP). Phenol was oxidatively deposited with 200 pulses at 0.6 V vs. Ag/Ag^+ for a duration of 5 sec with 10 sec rest in between each pulse, followed by 20 cyclic voltammogram sweeps between -0.4 V and 0.6 V vs. Ag/Ag^+ at 20 mV s^{-1} using a Metrohm Autolab PGSTAT204. The nanoporous PPO coated carbon monoliths were subsequently soaked in ethanol to remove excess electrolyte and dried at room temperature.

Lithiation-delithiation of anode-electrolyte assembly. The gyroidal nanoporous PPO coated carbon monolith and lithium foil were immersed in 1 M lithium perchlorate in dimethyl carbonate and ethylcarbonate (1:1 by volume) in a septum capped vial under argon atmosphere. After soaking for 2 days, the carbon was galvanostatically lithiated and delithiated at 10 μA to 0 V and 2 V vs. Li/Li^+ , respectively, in a two electrode setup using a MTI BT8 battery tester.

Cathode material infiltration. Sulfur as the cathode material was introduced to the mesopores of the PPO-coated carbon electrode through liquid/vapor infiltration at 155 °C for 24. Sulfur powder was put on the carbon-PPO electrode and heated to 155 °C in a sealed flask in air.

Cathode current collector infiltration. Poly(ethylene dioxothiophene) (PEDOT) was infiltrated and in-situ synthesized and doped inside the nanopores using oxidative polymerization. A 0.7 M iron (III) *para*-toluene sulfonate solution in ethanol was cooled to 4 °C. EDOT was added to make a 1 M solution. The carbon-PPO-sulfur monolith was immersed in the solution with the wire connection above the liquid-air interface and kept for 20 mins at 4 °C. The 3D battery was subsequently removed from the solution, dried at room temperature for at least 4 hours, and further dried at 80 °C for at least 6 hours. The cathode was then contacted with silver epoxy (EPO-TEK H20E from EMS) on one of the 3D-battery surfaces. The cured electrical contact was again sealed to the outside with silicone rubber adhesive sealant (Momentive RTV 108).

3D battery lithiation and testing. The 3D battery assembly was immersed horizontally (i.e. parallel to the air-liquid interface) in 1 M lithium perchlorate in dioxolane (DOL) and dimethoxyethane (DME) (1:1 by volume) together with a lithium foil in a septum capped vial under argon atmosphere. After soaking for 2 days, the sulfur-PEDOT phase was discharged to 1 V vs. Li/Li⁺ at a current of 10 μA. After lithiation of the cathode, the 3D-battery was charged and discharged with varying rates and cut-off voltages as described in the text.

Characterization. Scanning electron microscopy (SEM) of carbonized samples was carried out on a Zeiss LEO 1550 FE-SEM or a Tescan Mira SEM operating at an accelerating voltage of 10-20 kV. The SEM was equipped with a Bruker energy dispersive spectrometer (EDS) for elemental analysis. SAXS measurements were performed on the monolithic carbon material at the Cornell High Energy Synchrotron Source (CHESS). The sample to detector distance was 2.6 m and the X-ray wavelength, λ , was 1.20 Å. The scattering vector, q , in the experiments is defined as $q = (4\pi/\lambda)\sin \theta$, where θ is half of the scattering angle. Nitrogen sorption isotherms were obtained on a Micromeritics ASAP 2020 surface area and

porosity analyzer at -196 °C. Lithiation and battery tests of monolithic carbon materials and composites were executed using a BST8-WA 8-channel battery analyzer from MTI Corporation. Resistances through the PPO thin film of the PPO-coated carbon monoliths and of the PEDOT and sulfur-PEDOT infiltrated insulating gyroidal mesoporous polymer frameworks were measured using cyclic voltammetry at a scan rate of 50 mV s⁻¹ with an AUTOLAB Metrohm Autolab PGSTAT204. The second contact for the uncoated and PPO-coated carbon monoliths was made using a liquid gallium-indium eutectic contact on one of the surfaces. Contacts for the PEDOT and sulfur-PEDOT infiltrated insulating gyroidal mesoporous polymer framework was made with silver epoxy (EPO-TEK H20E from EMS) on both surfaces.

APPENDIX D

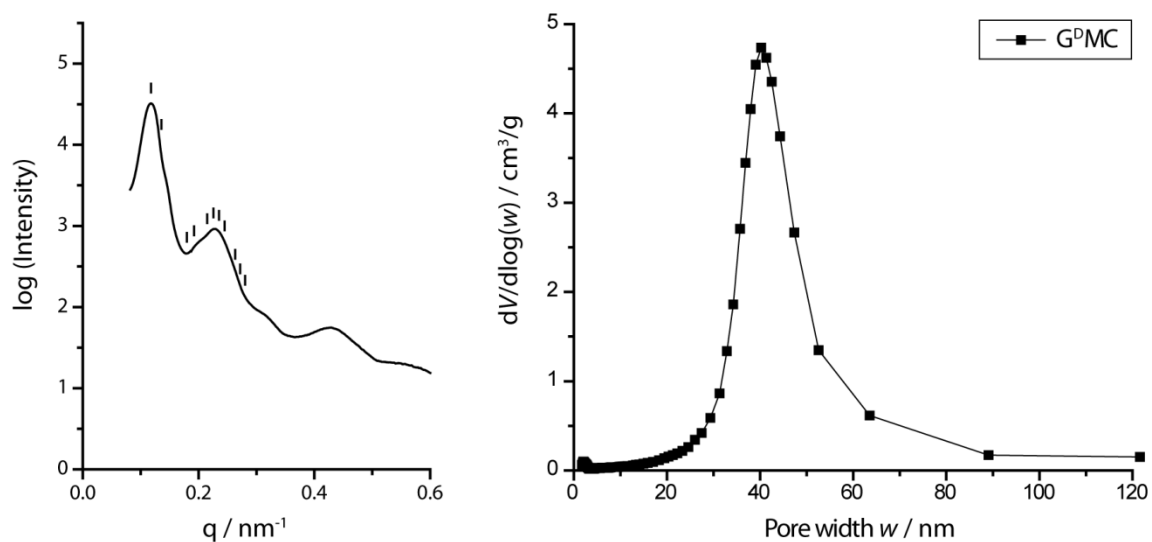


Figure S5.1. (a) Small-angle X-ray scattering pattern of $mG^D \text{MC}$ material after pyrolysis at $1100 \text{ }^\circ\text{C}$. The markings indicate expected positions for the $Ia-3d$ space group of the double gyroid morphology with (100) spacing of 131 nm . (b) BJH pore size distribution derived from the nitrogen adsorption isotherm of gyroidal mesoporous carbon material after pyrolysis at $1600 \text{ }^\circ\text{C}$.

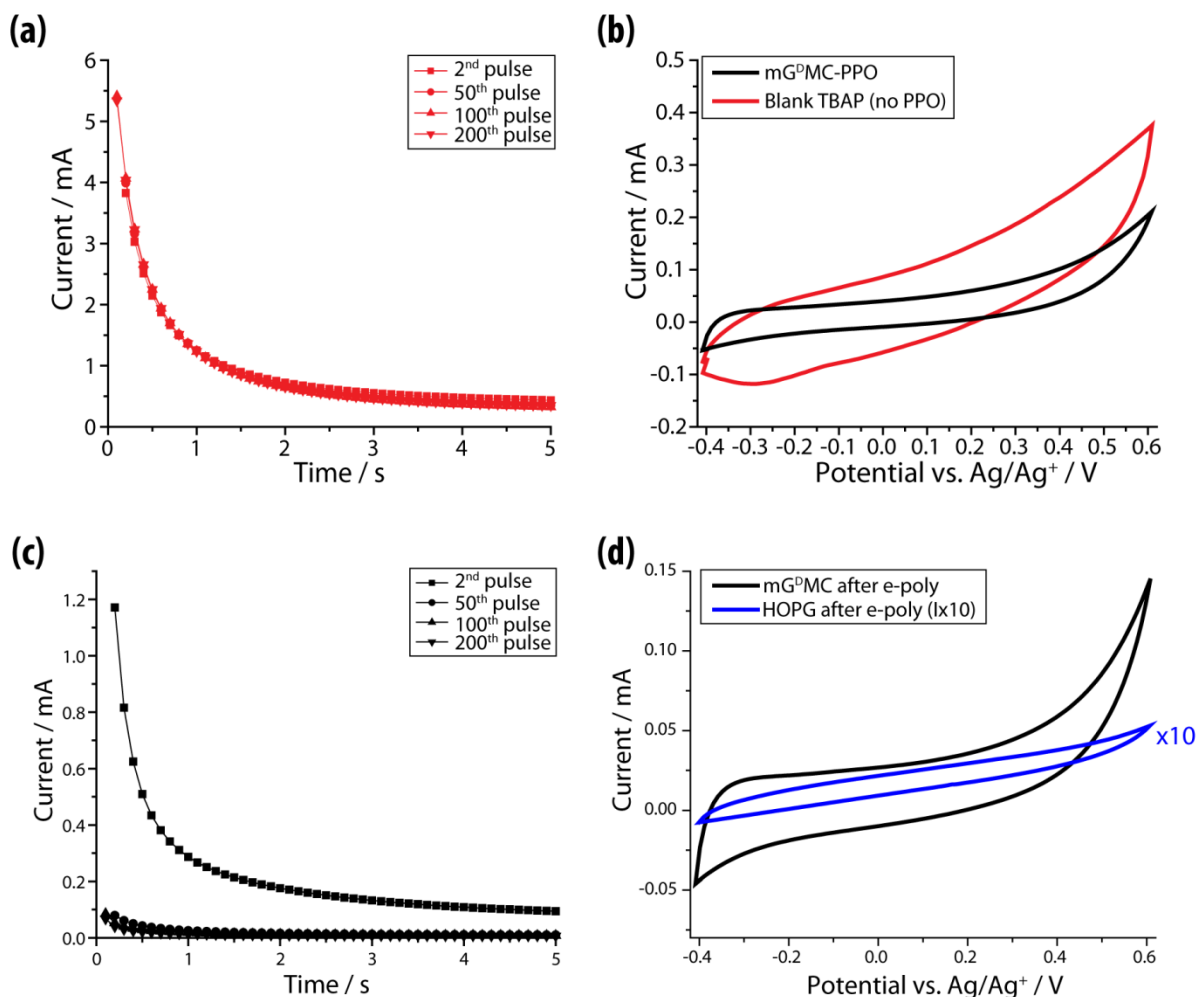


Figure S5.2. (a) Current-time traces of selected potentiostatic pulses at 0.6 V vs. Ag/Ag⁺ of gyroidal mesoporous carbon in the supporting electrolyte demonstrating no change over 200 pulses. (b) CVs after the potentiostatic pulses in the same solution for the supporting electrolyte (red) and after PPO deposition (black). (c) Current-time traces of selected potentiostatic deposition pulses of PPO on a flat carbon substrate (highly oriented pyrolytic graphite, HOPG) at 0.6 V vs. Ag/Ag⁺ showing the very fast decrease in double layer and oxidation current over pulses. (d) CVs after pulsed potentiostatic PPO deposition in the same solution of mG^DMC and HOPG showing only double layer current without a phenol oxidation peak (current of the HOPG is increased by a factor of 10 for clarity).

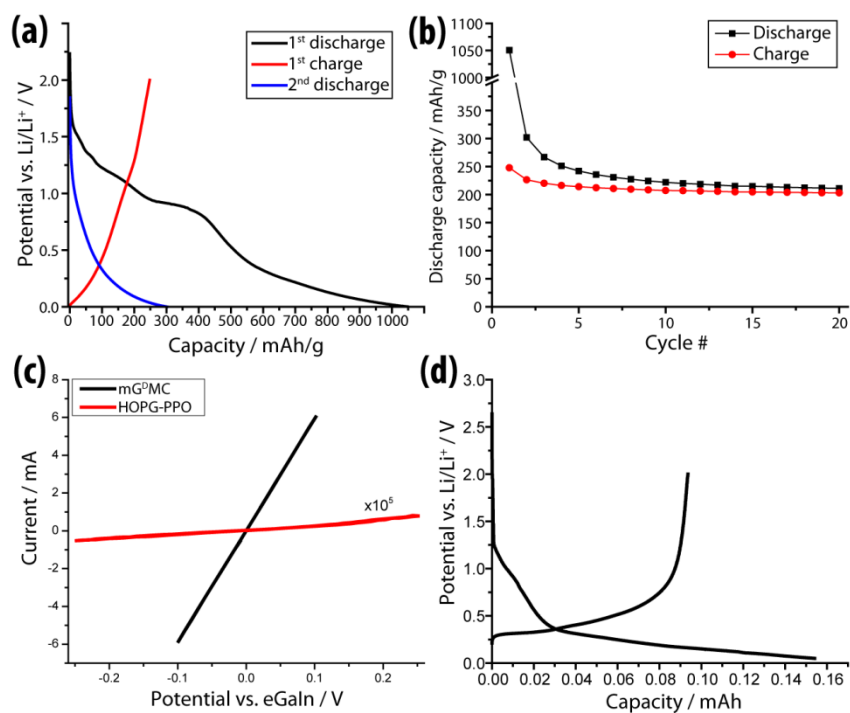


Figure S5.3. Charge and discharge curves of the first two cycles (a) and capacities of the first 22 cycles (b) of powdered gyroidal mesoporous carbon in a standard coin cell versus lithium metal. (c) Resistance measurements using a two-probe configuration of the wire-connected gyroidal mesoporous carbon anode without PPO coating (black) and HOPG after PPO electropolymerization (red) showing the increase in resistance by more than 5 orders of magnitude. Note, the current of the PPO coated HOPG was multiplied by a factor of 10^5 to facilitate comparison. (d) Discharge and charge curves of PPO-coated HOPG demonstrating reversible lithiation-delithiation through the PPO-layer.

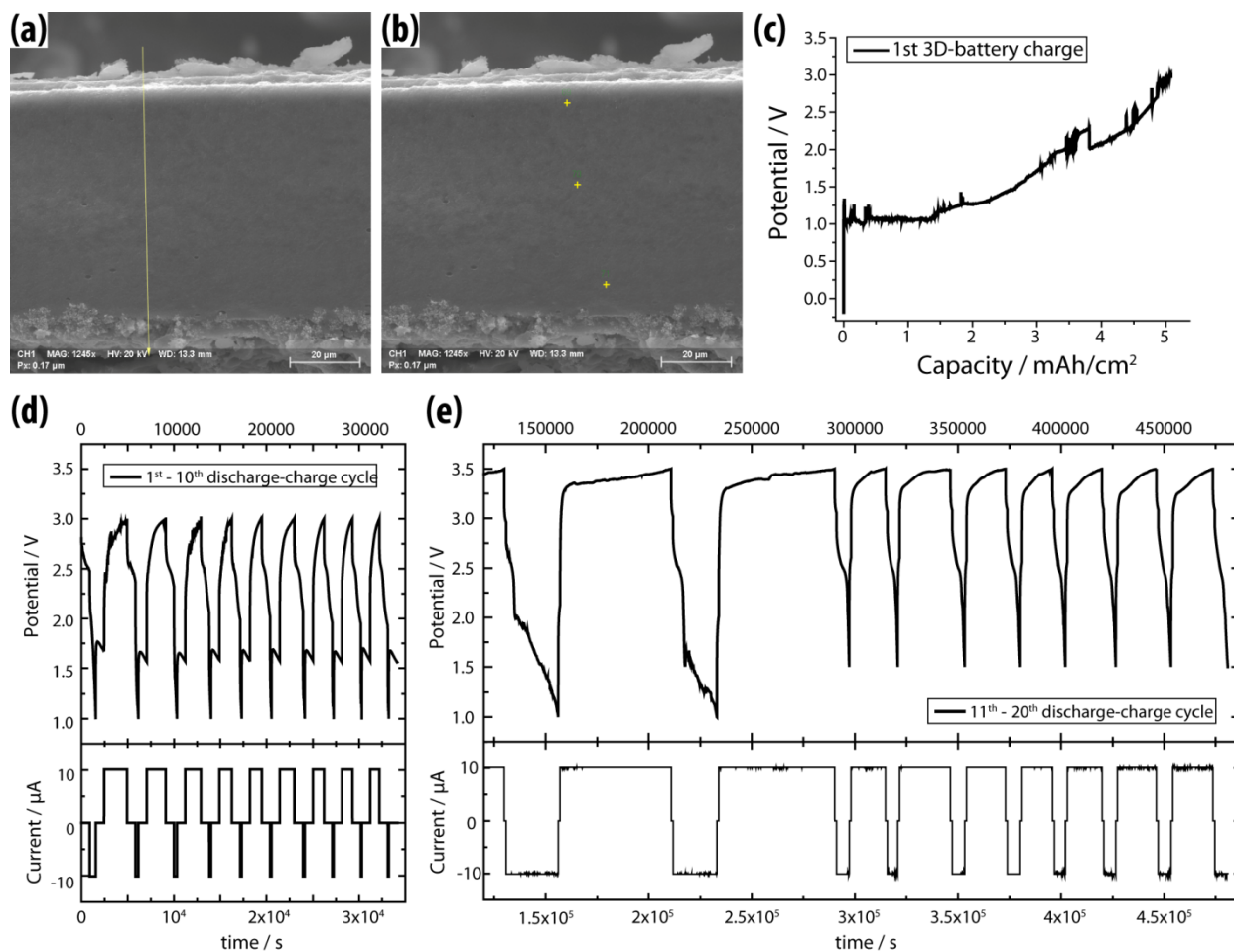


Figure S5.4. (a) Cross-sectional SEM image of the 3D-battery described in the main text with the arrow showing the position of the line scan plotted in Figure 5.4. (b) Cross-sectional SEM image of the 3D-battery described in the main text with the points showing the position of the quantified spectra described in the text. (c) First charge curve described in the text of the 3D-battery to 3 V at 0.125 mA cm^{-2} . (d) Current/potential-time traces of the first 10 cycles run between 1 and 3 V at 0.125 mA cm^{-2} with 15 mins rest between each applied charge or discharge current. (e) Current/potential-time traces of the 10th-20th cycle run between 1 V (11th+12th) or 1.5 V (13th-20th) and 3.5 V at 0.125 mA cm^{-2} with 15 mins rest between each applied charge or discharge current.

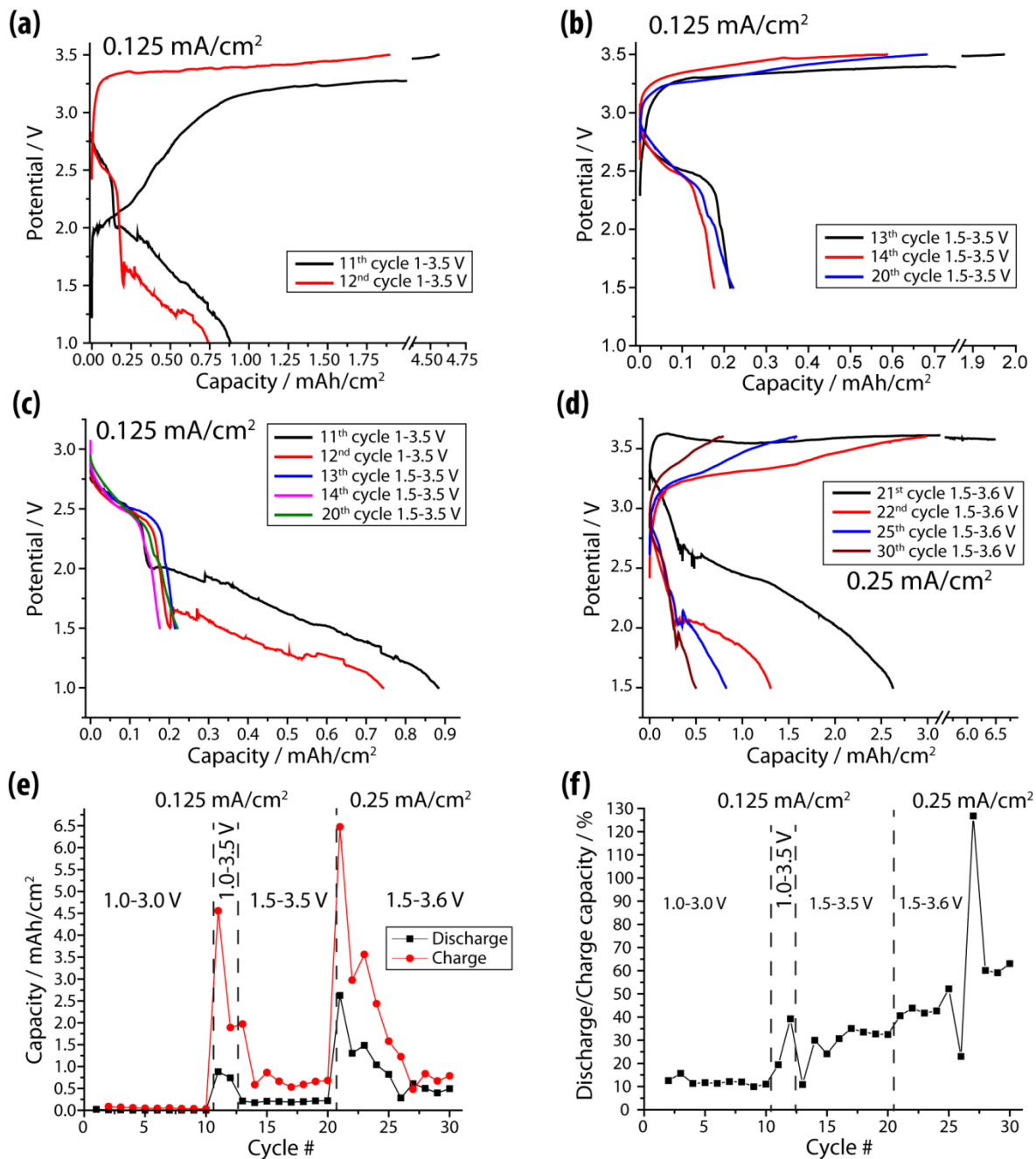


Figure S5.5. (a) Charge-discharge curves of the first two cycles that were run in the potential window of 1-3.5 V at a current of 0.125 mA cm^{-2} (11th and 12th cycle total). (b) Charge and discharge curves of selected cycles that were run in the potential window of 1.5-3.5 V at a current of 0.125 mA cm^{-2} (13th-20th cycle total). (c) Discharge curves of selected cycles that were run at a current of 0.125 mA cm^{-2} (11th-20th cycle total). (d) Charge and discharge curves of selected cycles that were run in the potential window of 1.5-3.6 V at a current of 0.25 mA cm^{-2} (21st-30th cycle total). (e) Charge and discharge capacities of the tested cycles. The cycle conditions (voltage window and current rate) are indicated in the graph. (f) Cycle efficiencies (coulombic efficiencies) of the tested cycles. The cycle conditions (voltage window and current rate) are indicated in the graph.

REFERENCES

- (1) Joachim, C.; Gimzewski, J. K.; Aviram, A. Electronics Using Hybrid-Molecular and Mono-Molecular Devices. *Nature* **2000**, *408*, 541–548.
- (2) Lemmerhirt, D. F.; Wise, K. D. Chip-Scale Integration of Data-Gathering Microsystems. *Proc. IEEE* **2006**, *94*, 1138–1158.
- (3) Armand, M.; Tarascon, J.-M. Building Better Batteries. *Nature* **2008**, *451*, 652–657.
- (4) Tarascon, J. M.; Armand, M. Issues and Challenges Facing Rechargeable Lithium Batteries. *Nature* **2001**, *414*, 359–367.
- (5) Oudenhoven, J. F. M.; Vullers, R. J. M.; van Schaijk, R. A Review of the Present Situation and Future Developments of Micro-Batteries for Wireless Autonomous Sensor Systems. *Int. J. Energy Res.* **2012**, *36*, 1139–1150.
- (6) Wang, Y.; Liu, B.; Li, Q.; Cartmell, S.; Ferrara, S.; Deng, Z. D.; Xiao, J. Lithium and Lithium Ion Batteries for Applications in Microelectronic Devices: A Review. *J. Power Sources* **2015**, *286*, 330–345.
- (7) Arthur, T. S.; Bates, D. J.; Cirigliano, N.; Johnson, D. C.; Malati, P.; Mosby, J. M.; Perre, E.; Rawls, M. T.; Prieto, A. L.; Dunn, B. Three-Dimensional Electrodes and Battery Architectures. *MRS Bull.* **2011**, *36*, 523–531.
- (8) Goodenough, J.; Abruña, H.; Buchanan, M. Basic Research Needs for Electrical Energy Storage. *US Dep. Energy Report of the Basic Energy Sciences Workshop on Electrical Energy Storage* **2007**.
- (9) Bruce, P. G.; Scrosati, B.; Tarascon, J.-M. Nanomaterials for Rechargeable Lithium Batteries. *Angew. Chemie Int. Ed.* **2008**, *47*, 2930–2946.
- (10) Poizot, P.; Laruelle, S.; Grugeon, S.; Dupont, L.; Tarascon, J. M. Nano-Sized Transition-Metal Oxides as Negative-Electrode Materials for Lithium-Ion Batteries. *Nature* **2000**, *407*, 496–499.
- (11) Chan, C. K.; Peng, H.; Liu, G.; McIlwrath, K.; Zhang, X. F.; Huggins, R. a; Cui, Y. High-Performance Lithium Battery Anodes Using Silicon Nanowires. *Nature nanotechnology*, 2008, *3*, 31–35.

- (12) Huang, S. Y. Rocking Chair Lithium Battery Based on Nanocrystalline TiO₂ (Anatase). *Journal of The Electrochemical Society*, 1995, *142*, L142.
- (13) Ji, X.; Lee, K. T.; Nazar, L. F. A Highly Ordered Nanostructured Carbon-Sulphur Cathode for Lithium-Sulphur Batteries. *Nat. Mater.* **2009**, *8*, 500–506.
- (14) Long, J. W.; Dunn, B.; Rolison, D. R.; White, H. S. Three-Dimensional Battery Architectures. *Chem. Rev.* **2004**, *104*, 4463–4492.
- (15) Majid Beidaghi, Y. G. Capacitive Energy Storage in Micro-Scale Devices: Recent Advances in Design and Fabrication of Micro- Supercapacitors. *Energy Environ. Sci.* **2014**, *7*, 867–884.
- (16) Roberts, M.; Johns, P.; Owen, J.; Brandell, D.; Edstrom, K.; El Enany, G.; Guery, C.; Golodnitsky, D.; Lacey, M.; Lecoeur, C.; *et al.* 3D Lithium Ion Batteries—from Fundamentals to Fabrication. *Journal of Materials Chemistry*, 2011, *21*, 9876.
- (17) Bates, J. B.; Dudney, N. J.; Neudecker, B.; Ueda, A.; Evans, C. D. Thin-Film Lithium and Lithium-Ion Batteries. *Solid State Ionics* **2000**, *135*, 33–45.
- (18) Dudney, N. J. Solid-State Thin-Film Rechargeable Batteries. *Mater. Sci. Eng. B Solid-State Mater. Adv. Technol.* **2005**, *116*, 245–249.
- (19) Rolison, D. R.; Long, J. W.; Lytle, J. C.; Fischer, A. E.; Rhodes, C. P.; McEvoy, T. M.; Bourg, M. E.; Lubers, A. M. Multifunctional 3D Nanoarchitectures for Energy Storage and Conversion. *Chem. Soc. Rev.* **2009**, *38*, 226–252.
- (20) Min, H.-S.; Park, B. Y.; Taherabadi, L.; Wang, C.; Yeh, Y.; Zaouk, R.; Madou, M. J.; Dunn, B. Fabrication and Properties of a Carbon/polypyrrole Three-Dimensional Microbattery. *J. Power Sources* **2008**, *178*, 795–800.
- (21) Pikul, J. H.; Gang Zhang, H.; Cho, J.; Braun, P. V.; King, W. P. High-Power Lithium Ion Microbatteries from Interdigitated Three-Dimensional Bicontinuous Nanoporous Electrodes. *Nat. Commun.* **2013**, *4*, 1732.
- (22) Ning, H.; Pikul, J. H.; Zhang, R.; Li, X.; Xu, S.; Wang, J.; Rogers, J. a.; King, W. P.; Braun, P. V. Holographic Patterning of High-Performance on-Chip 3D Lithium-Ion Microbatteries. *Proc. Natl. Acad. Sci.* **2015**, *112*, 201423889.
- (23) Liu, C.; Gillette, E. I.; Chen, X.; Pearse, A. J.; Kozen, A. C.; Schroeder, M. a.; Gregorczyk, K. E.; Lee, S. B.; Rubloff, G. W. An All-in-One Nanopore Battery Array. *Nat. Nanotechnol.* **2014**, 1–9.

- (24) Sun, K.; Wei, T.-S.; Ahn, B. Y.; Seo, J. Y.; Dillon, S. J.; Lewis, J. a. 3D Printing of Interdigitated Li-Ion Microbattery Architectures. *Adv. Mater.* **2013**, *25*, 4539–4543.
- (25) Nathan, M.; Golodnitsky, D.; Yufit, V.; Strauss, E.; Ripenbein, T.; Shechtman, I.; Menkin, S.; Peled, E. Three-Dimensional Thin-Film Li-Ion Microbatteries for Autonomous MEMS. *J. Microelectromechanical Syst.* **2005**, *14*, 879–885.
- (26) Kotobuki, M.; Suzuki, Y.; Munakata, H.; Kanamura, K.; Sato, Y.; Yamamoto, K.; Yoshida, T. Fabrication of Three-Dimensional Battery Using Ceramic Electrolyte with Honeycomb Structure by Sol–Gel Process. *Journal of The Electrochemical Society*, 2010, *157*, A493.
- (27) Nyström, G.; Marais, A.; Karabulut, E.; Wågberg, L.; Cui, Y.; Hamed, M. M. Self-Assembled Three-Dimensional and Compressible Interdigitated Thin-Film Supercapacitors and Batteries. *Nat. Commun.* **2015**, *6*, 7259.
- (28) Ergang, N. S.; Fierke, M. a.; Wang, Z.; Smyrl, W. H.; Stein, A. Fabrication of a Fully Infiltrated Three-Dimensional Solid-State Interpenetrating Electrochemical Cell. *Journal of The Electrochemical Society*, 2007, *154*, A1135.
- (29) Rhodes, C. P.; Long, J. W.; Pettigrew, K. a.; Stroud, R. M.; Rolison, D. R. Architectural Integration of the Components Necessary for Electrical Energy Storage on the Nanoscale and in 3D. *Nanoscale* **2011**, *3*, 1731–1740.
- (30) Bailey, T. S.; Hardy, C. M.; Epps, T. H.; Bates, F. S. A Noncubic Triply Periodic Network Morphology in Poly(isoprene-B-Styrene-B-Ethylene Oxide) Triblock Copolymers. *Macromolecules* **2002**, *35*, 7007–7017.
- (31) Werner, J. G.; Hoheisel, T. N.; Wiesner, U. Synthesis and Characterization of Gyroidal Mesoporous Carbons and Carbon Monoliths with Tunable Ultralarge Pore Size. *ACS Nano* **2014**, *8*, 731–743.
- (32) Reeja-Jayan, B.; Chen, N.; Lau, J.; Kattirtzi, J. a.; Moni, P.; Liu, A.; Miller, I. G.; Kayser, R.; Willard, A. P.; Dunn, B.; *et al.* A Group of Cyclic Siloxane and Silazane Polymer Films as Nanoscale Electrolytes for Microbattery Architectures. *Macromolecules* **2015**, DOI:10.1021/acs.macromol.5b00940.
- (33) Kozen, A. C.; Pearse, A. J.; Lin, C.-F.; Noked, M.; Rubloff, G. W. Atomic Layer Deposition of the Solid Electrolyte LiPON. *Chem. Mater.* **2015**, DOI:10.1021/acs.chemmater.5b01654.
- (34) Rhodes, C. P.; Long, J. W.; Doescher, M. S.; Fontanella, J. J.; Rolison, D. R. Nanoscale Polymer Electrolytes: Ultrathin Electrodeposited Poly(phenylene Oxide) with Solid-State Ionic Conductivity. *J. Phys. Chem. B* **2004**, *108*, 13079–13087.

- (35) Werner, J. G.; Scherer, M. R. J.; Steiner, U.; Wiesner, U. Gyroidal Mesoporous Multifunctional Nanocomposites via Atomic Layer Deposition. *Nanoscale* **2014**, *6*, 8736–8742.
- (36) Long, J. W.; Rhodes, C. P.; Young, A. L.; Rolison, D. R. Ultrathin, Protective Coatings of Poly(o-Phenylenediamine) as Electrochemical Proton Gates: Making Mesoporous MnO₂ Nanoarchitectures Stable in Acid Electrolytes. *Nano Lett.* **2003**, *3*, 1155–1161.
- (37) McCarley, R. L.; Irene, E. a.; Murray, R. W. Permeant Molecular Sieving with Electrochemically Prepared 6-Nm Films of Poly(phenylene Oxide). *J. Phys. Chem.* **1991**, *95*, 2492–2498.
- (38) Xing, W.; Bai, P.; Li, Z. F.; Yu, R. J.; Yan, Z. F.; Lu, G. Q.; Lu, L. M. Synthesis of Ordered Nanoporous Carbon and Its Application in Li-Ion Battery. *Electrochim. Acta* **2006**, *51*, 4626–4633.
- (39) Hong, K. H.; Oh, K. W.; Kang, T. J. Preparation and Properties of Electrically Conducting Textiles by in Situ Polymerization of poly(3,4-Ethylenedioxythiophene). *J. Appl. Polym. Sci.* **2005**, *97*, 1326–1332.
- (40) Gao, J.; Lowe, M. A.; Kiya, Y.; Abruña, H. D. Effects of Liquid Electrolytes on the Charge-Discharge Performance of Rechargeable Lithium/sulfur Batteries: Electrochemical and in-Situ X-Ray Absorption Spectroscopic Studies. *J. Phys. Chem. C* **2011**, *115*, 25132–25137.
- (41) Cuisinier, M.; Cabelguen, P.-E.; Evers, S.; He, G.; Kolbeck, M.; Garsuch, A.; Bolin, T.; Balasubramanian, M.; Nazar, L. F. Sulfur Speciation in Li–S Batteries Determined by Operando X-Ray Absorption Spectroscopy. *J. Phys. Chem. Lett.* **2013**, *4*, 3227–3232.
- (42) Burkhardt, S. E.; Rodríguez-Calero, G. G.; Lowe, M. a.; Kiya, Y.; Hennig, R. G.; Abruña, H. D. Theoretical and Electrochemical Analysis of poly(3,4- Alkylenedioxythiophenes): Electron-Donating Effects and Onset of P-Doped Conductivity. *J. Phys. Chem. C* **2010**, *114*, 16776–16784.

CHAPTER 6

CONCLUSIONS

Nanohybrids and nanocomposites with three-dimensional (3D) nanostructures offer tremendous potential in the field of energy storage and conversion due to the combination of multiple functionalities of the individual components and phases on the nanometer scale. Large surface and interface areas lead to remarkable interactions and synergistic effects that often by far surpass the properties and performance of the individual components. Self-assembly offers a scalable route for the synthesis and fabrication of nanostructures with a large range of tunability. In this dissertation, I have demonstrated the tunable synthesis of periodically ordered three-dimensional carbon materials and carbon based multifunctional and rationally designed nanohybrids using block copolymer self-assembly and spatially controlled synthesis methods.

In chapter 1, I described the tunability of the structural parameters of ordered mesoporous carbon (OMC) materials, and in particular bicontinuous gyroidal mesoporous materials, from the self-assembly and structure direction of the triblock terpolymer poly(isoprene)-*block*-poly(styrene)-*block*-poly(ethylene oxide) (ISO) and phenolic resols. The ISO-resols system can be tailored to obtain OMCs with desired structure, porosity, chemical composition and macroscopic shape. I demonstrated that morphology, porosity, as well as pore and unit cell size are independently controllable by rationally designing BCP composition, molar mass, and polymer-to-precursor ratio. The reported morphologies include one-dimensional (1D) hexagonally packed cylinders, three-dimensional (3D) double gyroid majority networks, and the first reported chiral single gyroid minority carbon network that were remarkably stable up to 1600 °C. The pore size was controllable over the range of 12-40 nm, which included the largest mesopore size for soft-templated ordered mesoporous carbons to date. The structural stability of the gyroidal mesoporous carbons was further demonstrated using physical activation of the carbon materials. Despite the introduction of a large fraction of micro- and small nanopores during the harsh activation

treatment, and the increase of the surface area to over $2000 \text{ m}^2 \text{ g}^{-1}$ after a weight loss of 78 wt%, the gyroidal mesostructure stayed intact.

Due to the incredible tunability over the structural properties of nanomaterials from block copolymer self-assembly, they are ideal candidates for structure-property relationship studies. To this end in chapter 2 I presented the methodological study of my carbons as host materials in carbon-sulfur nanocomposites for lithium-sulfur batteries. For my sulfur backfilled OMCs I found that the 3D double gyroidal matrix morphology led to higher capacity retention over cycling relative to the more open single gyroid structure, with little effect of varying pore size above 10 nm. Carbonization temperature had a substantial effect on cycling, with good performance for low-temperature carbonized host materials, most likely due to higher heteroatom content, surface functionality, and microporosity. The beneficial impact of micro (<2 nm) and small nanopores (<4 nm) on the capacity retention over cycling was further confirmed using the activated gyroidal carbon materials that lead to state-of-the-art performance. These highly porous materials, however, reduce the volumetric capacity and energy density significantly. Therefore, I believe that research towards sulfur-host materials that are strongly interacting with the hydrophilic polysulfide species, like surface functionalized nanoporous carbonaceous and polymeric materials, is the most promising future direction for reaching performance characteristics that justify commercialization of this highly promising energy storage material.

The concept of rationally designed two-component multifunctional nanohybrids is further expanded in chapter 3. Here, I studied the applicability of atomic layer deposition (ALD) in nanoporous monolithic bulk materials (square centimeters in area and tens of micrometers in thickness) with conformal 13 nm thin titania deposition in 40 nm large gyroidal mesopores and more than 7 μm deep into the films. This went far beyond what had been described previously, where only substrate-supported block copolymer derived nanoporous thin films had been investigated. However, it also demonstrated the limitations of ALD for conformally coating nanoporous bulk materials. The resulting gyroidal mesoporous core-shell hybrids exhibited triple-functionality with a graphitized carbon core, crystallized anatase-titania shell, and

3D continuous mesopores. The proximity of these functional materials on the nanoscale results in large interfaces with potential synergistic effects important for various electrochemical devices. The control over structural parameters of the carbon substrate (e.g. pore size, dimensionality) and the thickness of the titania layer make this system very interesting for future systematic studies on the influence of these parameters on, for example, photocatalytic performance or pseudocapacitive energy storage.

The ultimate goal for 3D multifunctional nanohybrids is the assembly of a functional device with all its individual components combined on the nanoscale. For example, combining anode, electrolyte, and cathode materials may enable the formation of a three-dimensionally integrated nanobattery (3D-battery). Such integrated 3D nano-architectures promise significant battery performance improvements, especially the increase of energy density per area and volume, as well as power capabilities due to a significantly reduced ion-diffusion length. In the last chapter of my thesis I described the fabrication of such a multifunctional nanohybrid by employing conformal, self-limiting and self-healing electropolymerization of a thin (<10 nm) electronically insulating but lithium conducting poly(phenylene oxide) layer to coat the 40 nm large pores of my monolithic gyroidal OMC constituting battery electrolyte and anode, respectively. I demonstrated reversible lithiation-delithiation of such polymer-electrolyte coated carbon anodes, thereby proving the functionality of these nano-assemblies. I further successfully backfilled the anode-electrolyte hybrids with sulfur and poly(ethylene dioxothiophene) (PEDOT) as active cathode material and current collector, respectively, which completed the assembly of a lithium-ion 3D battery consisting of two electrode materials with different electrochemical potentials separated by an ion-conducting electronic insulator, all with nanoscopic dimensions. I show the first proof of reversible battery cycling behavior of this all-nano-integrated 3D-battery. Future work on this system should include a thorough study of available cathode materials, as well as conducting polymers as integrated cathode materials. PEDOT has a limited applicability at the lower potentials of sulfur reduction, which potentially leads to irreversible capacity loss at low voltages. Through chemical modification of the monomers, the operating potentials of conducting polymers can be tuned. Other intermediate-voltage cathode materials

that are of interest for this 3D-battery architectures include redox-active organic molecules such as quinone derivatives that can be solution infiltrated into the pore structure before or together with the conducting polymer.

For future research directions, the 3D-battery concept has many parameters and components that can be changed for optimization, or specific applications of this energy storage device can be targeted. These include requirements such as high volumetric energy density, power capabilities, or architectural limitations. The size of the anode and cathode phases, for example, can be extended from the nanoscale (good for high power applications) to the mesoscale (100s of nanometers or micrometers, good for higher volumetric energy density). To this end, graded hierarchically meso- and macroporous materials that were recently developed in the Wiesner group are interesting candidates as alternative architectures for 3D-batteries.¹ For example, such an architecture made from carbon could be used as the framework for one of the electrodes, where the active material is backfilled into the carbon mesoporosity. After conformal deposition of a solid electrolyte onto the remaining porosity, the macropores could in turn be infiltrated with the counter electrode composite. This concept integrates the carbon framework solely as the current collector and advanced anode materials can be applied, such as lithium titanate, that show high-rate capabilities due to fast lithium-ion diffusion but are electronically insulating. For on-chip 3D-battery applications, a laser-patterning process of porous carbonaceous structures recently developed by the Wiesner group could be used to directly write the carbon framework onto a silicon wafer with spatial control.² All subsequent steps for the full synthesis and assembly of an on-chip 3D thin film battery could be applied directly to the substrate supported carbon nanostructure.

REFERENCES

- (1) Gu, Y.; Werner, J. G.; Dorin, R. M.; Robbins, S. W.; Wiesner, U. Graded Porous Inorganic Materials Derived from Self-Assembled Block Copolymer Templates. *Nanoscale* **2015**, *7*, 5826–5834.
- (2) Tan, K. W.; Jung, B.; Werner, J. G.; Rhoades, E. R.; Thompson, M. O.; Wiesner, U. Transient Laser Heating Induced Hierarchical Porous Structures from Block Copolymer-Directed Self-Assembly. *Science* **2015**, *349*, 54–58.